

# Attoseconds and the exascale: on laser plasma surface interactions



Robin Timmis  
University College  
University of Oxford

A thesis submitted for the degree of  
*Doctor of Philosophy*

Michaelmas 2014



# Acknowledgements

## **Personal Institutional**

The author thanks the Norreys Research Group, Prof. Philip Burrows and Dr. Qingsong Feng for useful discussions, the SMILEI consortium and the ARCHER2 support team. The authors also acknowledge the support of AWE plc, UKRI-EPSRC and the Oxford-Berman Graduate Scholarship program. This work used the ARCHER2 UK National Supercomputing Service (<https://www.archer2.ac.uk>) under project e674 of URKI-EPSRC grant no. EP/R029148/1 and UKRI-STFC grant no. ST/V001655/1.



## Abstract

The commissioning of multi-petawatt class laser facilities around the world is gathering pace. One of the primary motivations for these investments is the acceleration of high-quality, low-emittance electron bunches. Here we explore the interaction of a high-intensity femtosecond laser pulse with a mass-limited dense target to produce MeV attosecond electron bunches in transmission and confirm with three-dimensional simulation that such bunches have low emittance and nano-Coulomb charge. We then perform a large parameter scan from non-relativistic laser intensities to the laser-QED regime and from the critical plasma density to beyond solid density to demonstrate that the electron bunch energies and the laser pulse energy absorption into the plasma can be quantitatively described via the Zero Vector Potential mechanism. These results have wide-ranging implications for future particle accelerator science and associated technologies.



# Contents

<b>List of Figures</b>	<b>xi</b>
<b>A List of Symbols and Abbreviations</b>	<b>xv</b>
<b>1 Introduction</b>	<b>1</b>
1.1 High-energy-density physics . . . . .	2
1.2 Electromagnetism fundamentals . . . . .	4
1.3 The definition of a classical plasma . . . . .	5
1.3.1 The Debye length . . . . .	6
1.3.2 The plasma parameter . . . . .	7
1.3.3 Collisionality and the plasma frequency . . . . .	7
1.4 The Lawson-Woodward theorem . . . . .	9
1.5 Laser-solid density plasma linear interaction . . . . .	10
1.6 Relativity . . . . .	11
1.6.1 Ultra-relativistic similarity theory . . . . .	12
1.6.2 Relativistic lasers and plasmas . . . . .	14
1.6.3 Conservation of generalised transverse momentum . . . . .	15
1.7 QED effects . . . . .	16
1.7.1 High-energy photon emission and radiation reaction . . . . .	17
1.7.2 Multi-photon Breit-Wheeler pair production . . . . .	18
1.8 Simulating the interaction . . . . .	18
1.8.1 Supercomputing resources . . . . .	18
1.8.2 Particle-In-Cell codes . . . . .	19
1.8.3 Hydrodynamic codes . . . . .	26
1.9 Powering the interaction . . . . .	27
1.9.1 Laser contrast . . . . .	29
<b>2 The Zero Vector Potential Absorption Mechanism</b>	<b>31</b>
2.1 Motivations and an overview . . . . .	31
2.2 Introduction . . . . .	33
2.2.1 ZVP electron bunch energies . . . . .	40
2.2.2 ZVP bunches oblique incidence scaling . . . . .	43

2.2.3	Defining characteristics of the ZVP mechanism . . . . .	46
2.3	Numerical simulations of the ZVP mechanism . . . . .	46
2.3.1	The ZVP mechanism in 3D3V . . . . .	47
2.4	The ZVP electron bunch . . . . .	53
2.4.1	Energy absorption in the ZVP regime . . . . .	63
2.4.2	Unpacking the QED effects of Figure 2.12 . . . . .	66
2.4.3	Errors . . . . .	68
2.5	Conclusions . . . . .	69
<b>3</b>	<b>Attosecond X-ray harmonics on the ORION laser facility</b>	<b>71</b>
3.1	Introduction . . . . .	72
3.2	Theory . . . . .	73
3.2.1	The ROM model . . . . .	73
3.2.2	The normalisation factor . . . . .	78
3.2.3	Hole boring . . . . .	79
3.2.4	Harmonic source size . . . . .	83
3.2.5	The SHHG optimal parameter space . . . . .	83
3.3	Simulations . . . . .	85
3.3.1	1D PIC simulations of HHG . . . . .	85
3.3.2	Hydrodynamic simulations of preplasma formation . . . . .	91
3.4	The experiment . . . . .	96
3.4.1	Targets . . . . .	100
3.4.2	Contrast and plasma mirrors . . . . .	101
3.4.3	KBRXM . . . . .	101
3.5	Experimental data processing . . . . .	102
3.5.1	Image plate calibration . . . . .	102
3.5.2	OHREX calibration . . . . .	104
3.5.3	Extracting the data . . . . .	105
3.6	Experimental results . . . . .	108
3.7	Summary . . . . .	112
<b>4</b>	<b>Attosecond electron bunches and X-ray pulses on GEMINI PW</b>	<b>115</b>
4.1	Overview . . . . .	115
4.2	X-ray harmonics on GEMINI PW . . . . .	117
4.3	Observation of ZVP electron bunches . . . . .	119
4.4	Application of HHG to white light Laue diffraction . . . . .	123
4.5	Contrast . . . . .	124
4.5.1	Contrast on GEMINI PW . . . . .	124
4.5.2	Kahaly mirror . . . . .	128
4.6	Beyond GEMINI PW . . . . .	129

**Appendices**

<b>A General plasma physics</b>	<b>133</b>
A.1 Lorentz transformations of electromagnetic fields . . . . .	133
A.2 The headlight effect . . . . .	134
A.3 Geometric transverse emittance . . . . .	134
A.4 The Bourdier method . . . . .	137
<b>B PIC simulations</b>	<b>141</b>
B.1 Convergence of 3D PIC simulations . . . . .	141
<b>References</b>	<b>143</b>

*x*

# List of Figures

1.1	Laser systems across the globe, both commissioned and theorised.	3
1.2	Diagram to illustrate the derivation of the plasma frequency.	8
1.3	A schematic of the PIC code loop and the algorithms performed.	20
1.4	A representation of the staggered Yee grid.	21
1.5	Smilei simulation box decomposition into cells, patches and MPI patch collections.	23
1.6	Representation of the interaction of the ARCHER2 hardware and software components when running Smilei.	24
1.7	Image of the ORION SP1 double beamlet structure in the near-field.	28
2.1	Diagram of a p-polarised laser pulse incident at angle $\theta$ specularly reflected from a solid density plasma.	35
2.2	Diagram of a <i>p</i> -polarised laser pulse incident on an ablating overdense plasma.	38
2.3	The numerical simulation using a 3D Particle-In-Cell (PIC) code of the Zero Vector Potential (ZVP) mechanism.	48
2.4	Propagation of a vector potential zero through the ablating ZVP electron bunch.	51
2.5	Electron dynamics in 3D PIC simulation for both linear and circularly polarised relativistic laser pulses.	52
2.6	The Fourier transform of the reflected laser pulse in 3D PIC simulations.	53
2.7	2D PIC simulation results qualitatively describing typical mass-limited ZVP electron bunch structure.	55
2.8	Energy spectra for mass-limited electron bunches formed via linearly and circularly polarised laser pulses.	57
2.9	Mean mass-limited ZVP electron bunch normalised kinetic energies extracted from 2D PIC simulations.	59
2.10	Mass-limited electron bunch train length as a function of laser intensity and plasma density.	60
2.11	The relative errors for each mean energy data point compared to Figure 2.9.	64

2.12	Peak instantaneous bulk electron bunch total energy escaping to the plasma bulk rear. . . . .	65
2.13	An exploration of ZVP 2D PIC simulation stability. . . . .	69
3.1	2D PIC simulation of HHG beaming effect via hole boring. . . . .	80
3.2	Typical 1D HHG Smilei simulation results . . . . .	88
3.3	Comparison between simulation and analytical predictions of hole boring and HHG normalisation factor. . . . .	89
3.4	The effect of the PIC code particle shape function on numerical heating. . . . .	89
3.5	Reflected beam harmonic content up to the keV range in a high-resolution 1D PIC simulation. . . . .	90
3.6	Attosecond pulse train from the filtered reflected laser pulse. . . . .	91
3.7	Silicon dioxide plasma mirror switch on from irradiation by the SP2 main pulse. . . . .	93
3.8	The attenuation of the SP2 laser pulse as it propagates through a switched-on PM. . . . .	93
3.9	Typical preplasma formation from the incidence of the ORION SP2 laser prepulse on a plastic target. . . . .	94
3.10	Preplasma scale length parameter scan. . . . .	95
3.11	Typical electron temperature of a plastic target after irradiation by a petawatt class laser prepulse. . . . .	96
3.12	ORION HHG experiment target chamber set up. . . . .	98
3.13	ORION target chamber geometry . . . . .	99
3.14	ORION HHG experiment targets . . . . .	100
3.15	Unprocessed IP from ORION experiment . . . . .	106
3.16	Typical ORION experiment uncalibrated IP response quartz ( $10\bar{1}0$ ) crystal and Fourier transform . . . . .	107
3.17	Typical ORION experiment calibrated IP response for the quartz ( $10\bar{1}1$ ) crystal. . . . .	109
3.18	Dependence of the harmonic beam spectral intensity on laser spot size at 2.405 keV. . . . .	110
3.19	X-ray harmonic intensities measured on the ORION experiment compared to theory and simulation. . . . .	111
4.1	Planned GEMINI-PW experimental setup for the measurement of ZVP electron bunches. . . . .	120
4.2	Attosecond ZVP electron bunch targets . . . . .	120
4.3	Native contrast of the GEMINI PW laser system. . . . .	125
A.1	Emittance calculation for an ideal Gaussian distribution in phase space. . . . .	136

A.2	137
B.1 Comparison between the initial 3D simulation and a lower resolution version.	142



# A List of Symbols and Abbreviations

**Note** . . . . . All quantities are defined in SI units unless otherwise specified throughout the thesis.

$\alpha$	. . . . .	Twiss parameter = $-\frac{\langle x_i x'_i \rangle}{\epsilon_{\text{rms}}^i}$
$a_0$	. . . . .	Normalised vector potential = $\frac{e \mathbf{E}_L }{m_e c \omega_L}$
$A$	. . . . .	Atomic mass number
$\mathbf{A}$	. . . . .	Three-vector potential
$\mathbf{A}^\mu$	. . . . .	Four-vector potential = $(\phi/c, \mathbf{A})$
$\beta$	. . . . .	Normalised speed = $v/c$ or Twiss parameter = $\frac{\langle x_i \rangle}{\epsilon_{\text{rms}}^i}$
$\beta$	. . . . .	Normalised velocity = $\mathbf{v}/c$
$\mathbf{B}$	. . . . .	Magnetic field
$\mathbf{B}_L$	. . . . .	Magnetic field of a laser pulse
$c$	. . . . .	Speed of light = $3.00 \times 10^8 \text{ m s}^{-1}$
$\delta$	. . . . .	Skin depth
$\delta(\mathbf{x})$	. . . . .	Dirac-delta function
$d\mathbf{s}$	. . . . .	Vector line element
$\Delta$	. . . . .	Change in a variable
$D$	. . . . .	Number of dimensions
$\nabla$	. . . . .	Partial derivative = $\hat{\mathbf{x}}_\mu \frac{\partial}{\partial x_\mu}$ , $\mu = x, y, z$
$\epsilon_0$	. . . . .	Permittivity of free space = $8.854 \times 10^{-12} \text{ F m}^{-1}$
$\epsilon_{\text{rms}}$	. . . . .	Transverse geometric emittance
$\epsilon_{n,\text{rms}}$	. . . . .	Transverse normalised emittance
$e$	. . . . .	Absolute charge of an electron = $1.602 \times 10^{-19} \text{ C}$
$e^\pm$	. . . . .	Electron (−) or positron (+)
$\mathbf{E}$	. . . . .	Electric field
$E_S$	. . . . .	Schwinger electric field = $1.3 \times 10^{18} \text{ V m}^{-1}$

$\mathbf{E}_L$	Electric field of a laser pulse
$f$	Distribution function
$\mathbf{F}_L$	Lorentz force = $q(\mathbf{E} + \mathbf{v} \times \mathbf{B})$
$\gamma$	Lorentz/gamma factor = $\frac{1}{\sqrt{1-\beta^2}}$ or Twiss parameter = $\frac{\langle x_i'^2 \rangle}{\epsilon_{rms}^i}$ or high-energy photon
$\eta$	Efficiency
$I$	Electromagnetic field intensity
$\mathcal{H}$	Hamiltonian
$\theta$	Angle of incidence of a laser pulse
$\mathbf{J}$	Current density
$\mathbf{k}$	Electromagnetic three-wave vector
$\mathbf{K}^\mu$	Electromagnetic four-wave vector = $(\omega/c\mathbf{k})$
$K$	Boltzmann constant = $1.38 \times 10^{-23} \text{ J K}^{-1}$
$\lambda_D$	Debye length $\equiv \sqrt{\frac{\epsilon_0 K T_e}{n_e e^2}}$
$\lambda_L$	Laser pulse wavelength
$\Lambda_\nu^\mu$	Lorentz transformation matrix
$L$	Length
$\mathcal{L}$	Lagrangian
$\mu_0$	Vacuum permeability = $1.257 \times 10^{-6} \text{ N A}^{-2}$
$m_e$	Mass of an electron = $9.11 \times 10^{-31} \text{ kg}$
$n$	Harmonic order
$n, N$	Number
$n_c$	Plasma critical density = $\frac{\omega_L^2 m_e \epsilon_0}{e^2}$
$n_e$	Plasma electron number density
$\bar{n}_e$	Normalised plasma electron number density = $\frac{n_e}{n_c}$
$n_i$	Plasma ion number density
$\mathbf{n}$	Vector normal to a surface
$N_A$	Avogadro's number
$N_D$	Number of particles within the Debye sphere = $\frac{4}{3}\pi\lambda_D^3 n$
$\omega$	Angular frequency of an oscillation or low energy photon
$\omega_L$	Laser pulse angular frequency

$\omega_p$	Plasma frequency = $\sqrt{\frac{e^2 n_e}{m_e \epsilon_0}}$
$\phi$	Angle of laser polarisation out of the plane of interaction or scalar electromagnetic potential
$\mathbf{p}$	Three-momentum
$P$	Pressure
$\mathbf{P}^\mu$	Four-momentum = $(U/c, \mathbf{p})$
$Q$	Charge
$\rho$	Density
$r_L$	Relativistic Larmor radius = $\frac{\gamma m_e v}{e \mathbf{B} }$
$\mathbf{r}$	Radial vector
$\hat{\mathbf{r}}$	Radial unit vector
$R$	Rate
$\sigma$	Surface area
$S$	Relativistic similarity parameter = $\bar{n}_e/a_0$
$S(\mathbf{x})$	Shape function
$\tau$	Average time or standard deviation of time
$t$	Time
$T$	Kinetic energy
$T_e$	Plasma electron temperature
$u, v$	Speed
$\mathbf{u}, \mathbf{v}$	Velocity
$U$	Energy
$v_\phi$	Phase velocity
$V$	Potential or volume
$w_L$	Beam waist
$w_p$	Quasi-particle weight
$\chi_\gamma$	Photon quantum parameter
$x, y, z$	Standard Cartesian coordinates in 3D
$\mathbf{x}, \mathbf{y}, \mathbf{z}$	Vectors along each axis of the Cartesian coordinate system
$\hat{\mathbf{x}}, \hat{\mathbf{y}}, \hat{\mathbf{z}}$	Unit vectors along each axis of the Cartesian coordinate system
$Z$	Ion charge state in units of $e$

<b>Subscripts . . .</b>	The following are defined the subscripts
C . . . . .	Pseudocapacitor
e . . . . .	Electron
$\gamma$ . . . . .	Photon
L . . . . .	Laser pulse or Longitudinal
T . . . . .	Transvere to a laser pulse
pol . . . . .	Along the polarisation vector of a laser pulse
$\perp$ . . . . .	Perpendicular
$\parallel$ . . . . .	Parallel
$i, j$ . . . . .	Indices
s . . . . .	Species
$x, y, z$ . . . . .	Along the specific Cartesian axes
$\infty$ . . . . .	
<b>The hat symbol</b>	To represent a normalised vecotr
<b>primed coordinates</b>	<del>and reference frames</del>
<b>1D, 2D, 3D</b> . .	One-, two- or three-dimension(al)
<b>BW</b> . . . . .	Breit-Wheeler
<b>CLF</b> . . . . .	Central Laser Facility
<b>CPA</b> . . . . .	Chirped Pulse Amplification
<b>CSE</b> . . . . .	Coherent Synchrotron Emission
<b>FDTD</b> . . . . .	Finite Difference Time Domain
<b>HB</b> . . . . .	Hole Boring
<b>HED</b> . . . . .	High-Energy-Density
<b>HHG</b> . . . . .	High Harmonic Generation
<b>HPC</b> . . . . .	High Performance Computing
<b>OHREX</b> . . . .	ORION High Resolution X-ray
<b>PIC</b> . . . . .	Particle-In-Cell
<b>QED</b> . . . . .	Quantum Electro-Dynamics
<b>ROM</b> . . . . .	Relativistic Oscillating Mirror
<b>RPM</b> . . . . .	Relativistic Plasma Mirror
<b>RR</b> . . . . .	Radiation Reaction
<b>SF-QED</b> . . . .	Strong-Field Quantum Electro-Dynamics
<b>ZVP</b> . . . . .	Zero Vector Potential

# 1

## Introduction

### Contents

---

<b>1.1</b>	<b>High-energy-density physics</b>	<b>2</b>
<b>1.2</b>	<b>Electromagnetism fundamentals</b>	<b>4</b>
<b>1.3</b>	<b>The definition of a classical plasma</b>	<b>5</b>
1.3.1	The Debye length . . . . .	6
1.3.2	The plasma parameter . . . . .	7
1.3.3	Collisionality and the plasma frequency . . . . .	7
<b>1.4</b>	<b>The Lawson-Woodward theorem</b>	<b>9</b>
<b>1.5</b>	<b>Laser-solid density plasma linear interaction</b>	<b>10</b>
<b>1.6</b>	<b>Relativity</b>	<b>11</b>
1.6.1	Ultra-relativistic similarity theory . . . . .	12
1.6.2	Relativistic lasers and plasmas . . . . .	14
1.6.3	Conservation of generalised transverse momentum . . . . .	15
<b>1.7</b>	<b>QED effects</b>	<b>16</b>
1.7.1	High-energy photon emission and radiation reaction . .	17
1.7.2	Multi-photon Breit-Wheeler pair production . . . . .	18
<b>1.8</b>	<b>Simulating the interaction</b>	<b>18</b>
1.8.1	Supercomputing resources . . . . .	18
1.8.2	Particle-In-Cell codes . . . . .	19
1.8.3	Hydrodynamic codes . . . . .	26
<b>1.9</b>	<b>Powering the interaction</b>	<b>27</b>
1.9.1	Laser contrast . . . . .	29

---

## 1.1 High-energy-density physics

We sit on the verge of the exascale revolution both in terms of computing [1] and laser power. With rapid adoption of the pioneering advancements of Chirped Pulse Amplification (CPA) by Strickland and Mourou [2] and of Optical Parametric Chirped Pulse Amplification [3], multi-petawatt facilities have been commissioned and built across the globe and plans for sub-exawatt facilities are now underway. Figure 1.1 details the parameter space accessible by current and proposed facilities [2, 4–68], clearly, there is no indication of wavering interest or support for the field of High-Energy-Density (HED) physics.

HED physics is the laboratory study of the behaviour of matter with a pressure above 10 GPa, approximately one million atmospheres and containing free electrons not confined to a solid state [72], typically in the plasma state of matter. HED conditions are found for a vast range of densities and temperatures (from zero to a million million Kelvin) operating in both the quantum and relativistic realms. The applications are equally diverse, including but not limited to inertial confinement fusion, particle acceleration for scientific or medical purposes and light sources for diagnostic tools. Ubiquitous in the natural universe, beyond our solar system, all that can be observed in the sky is radiation emitted from HED plasmas [**chen**].

This thesis concerns itself with a specific interaction, that of a high-power short-pulse laser incident on a flat solid target. Through the process discussed in this thesis, using state-of-the-art 10 PW laser facilities such as [19], electron bunches and light pulse of unprecedented charge and brightness can be produced, both with attosecond duration, thus uncovering new avenues for attosecond resolution diagnostics and to access the Schwinger limit. Seemingly counter-intuitively, as the laser power increases, via relativistic effects and for certain conditions, greater coherency in the electron dynamics can be observed and the signals amplified. The red dashed line of figure 1.1 could be accessed using next-generation sub-ewatt facilities. Before delving into this fascinating phenomenon, the remainder of this chapter will provide some of the relevant background information. Chapter 2 introduces the Zero Vector Potential of attosecond absorption in this laser-solid interaction. The following

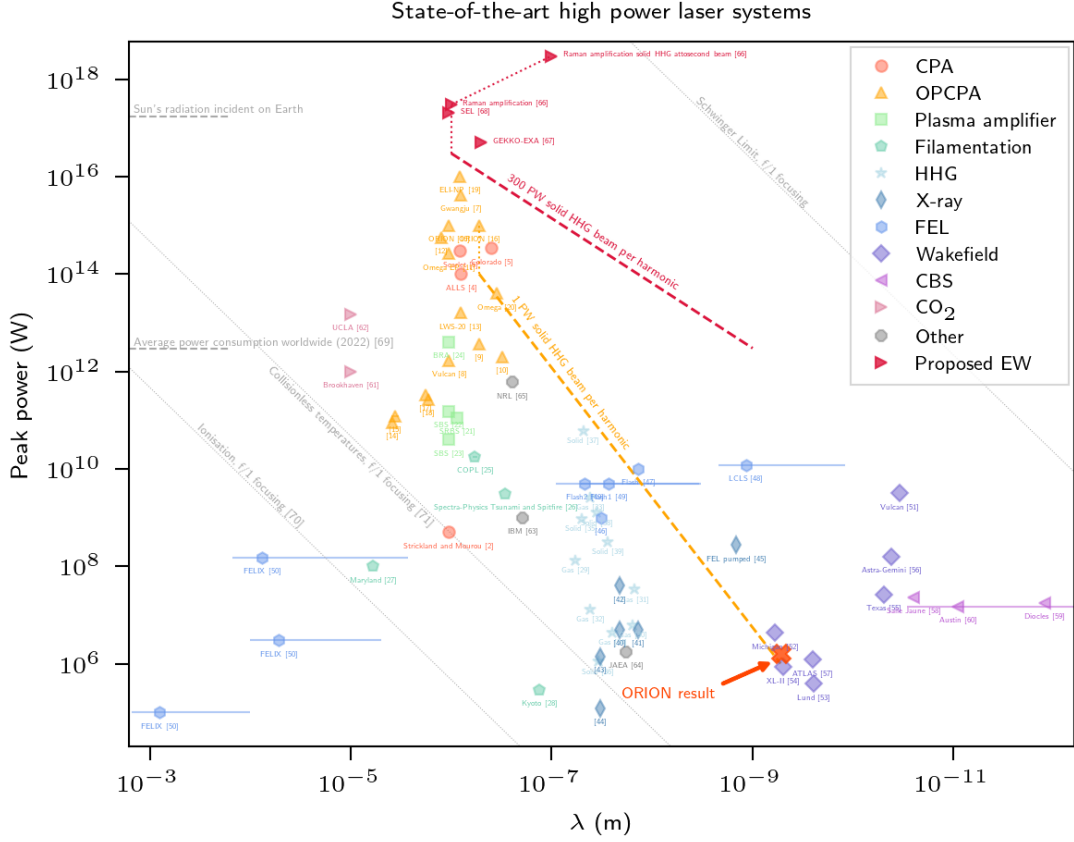


**Figure 1.1:** A by no means exhaustive plot of laser systems across the globe, both commissioned and theorised [2, 4–71] to provide an overview of the parameter space currently and soon to be accessible. The experimental result obtained at the ORION laser facility [16] is presented, and will be discussed in detail in chapter ???. The dashed orange line is the accompanying theoretical prediction. The red dashed line indicates the parameter space accessible via the methods discussed in this thesis when coupled with a sub-ettawatt Raman amplified laser beam. Such a beam would provide intensities in the water window many orders of magnitude beyond that currently accessible in state-of-the-art facilities.

chapter discusses the associated process of Surface High Harmonic Generation and the results of a recent experiment at the ORION laser facility where the absolute intensity of individual X-ray harmonics was measured and compared to the theory.

## 1.2 Electromagnetism fundamentals

The spatio-temporal propagation of electric  $\mathbf{E}(t, \mathbf{x})$  and magnetic  $\mathbf{B}(t, \mathbf{x})$  fields must satisfy Maxwell's equations [73]

$$\nabla \cdot \mathbf{B} = 0, \quad (1.1a)$$

$$\nabla \cdot \mathbf{E} = \frac{\rho}{\epsilon_0}, \quad (1.1b)$$

$$\nabla \times \mathbf{B} = \mu_0 \mathbf{J} + \mu_0 \epsilon_0 \partial_t \mathbf{E}, \quad (1.1c)$$

$$\nabla \times \mathbf{E} = -\partial_t \mathbf{B}. \quad (1.1d)$$

Here,  $\epsilon_0 = 8.85 \times 10^{-12} \text{ F m}^{-1}$  and  $\mu_0 = 1.26 \times 10^{-6} \text{ N A}^{-2}$  are the vacuum permittivity and permeability respectively and  $\rho(t, \mathbf{x})$  and  $\mathbf{J}(t, \mathbf{x})$  the total charge and current densities of charged particles present.

A particle with charge  $q$  and velocity  $\mathbf{v}$  in the presence of electromagnetic fields experiences the Lorentz force,

$$\mathbf{F}_L = q(\mathbf{E} + \mathbf{v} \times \mathbf{B}). \quad (1.2)$$

The electromagnetic fields can be obtained from the scalar,  $\phi$ , and vector,  $\mathbf{A}$ , potentials as [74]

$$\mathbf{E} = -\nabla \phi - \partial_t \mathbf{A}, \quad (1.3)$$

$$\mathbf{B} = \nabla \times \mathbf{A}. \quad (1.4)$$

### The Vlasov-Maxwell system of equations

A collisionless and fully ionised plasma is fully described in the kinetic description by the Vlasov-Maxwell system of equations [75]. Each plasma species,  $s$ , of particles with mass  $m_s$  and charge  $q_s$  is described by its distribution function  $f_s(t, \mathbf{x}, \mathbf{p})$  at time  $t$ , position  $\mathbf{x}$  and momentum  $\mathbf{p} = m_s \gamma \mathbf{v}$ . The distribution satisfies the Vlasov equation, that is,

$$(\partial_t + \frac{\mathbf{p}}{m_s \gamma} \cdot \nabla + \mathbf{F}_L \cdot \nabla_{\mathbf{p}}) f_s = 0, \quad (1.5)$$

where  $\mathbf{F}_L$  is the Lorentz force given in equation 1.2. The electric  $\mathbf{E}(t, \mathbf{x})$  and magnetic  $\mathbf{B}(t, \mathbf{x})$  fields that generate the force must satisfy Maxwell's equations (equations 1.1).

This self-consistent system of equations describes the dynamics of plasma particles within electromagnetic fields. The particles modify the fields via their charge and current densities,

$$\rho(t, \mathbf{x}) = \sum_s q_s \int d^3 p f_s(t, \mathbf{x}, \mathbf{p}), \quad (1.6)$$

and

$$\mathbf{J}(t, \mathbf{x}) = \sum_s q_s \int d^3 p \mathbf{v} f_s(t, \mathbf{x}, \mathbf{p}), \quad (1.7)$$

respectively.

### 1.3 The definition of a classical plasma

As outlined in F. Chen's definitive textbook 'Introduction to Plasma Physics and Controlled Fusion' [73], a plasma must fulfil three criteria, namely,

1. Ionisation: a plasma must consist of both charged and neutral particles, of course, this alone cannot define a plasma, any gas will contain some degree of ionisation, however, with reference to figure 1.1, clearly, modern high power laser systems will instantaneously fully ionise a target upon incidence;
2. Quasineutrality: while locally there can be (often extreme) electromagnetic forces and charge concentrations at work, over the length scales of the plasma, such forces are screened out and the plasma bulk remains net neutral in charge;
3. Collective behaviour: unlike in a gas, where collisions will dominate the dynamics, the particles in a plasma generate electromagnetic fields that interact at a distance and thus a particle's motion depends not only on its immediate vicinity but on the surrounding plasma conditions, indeed often it is the so-called *collisionless* plasmas where collisions can be safely neglected that are of most interest, as is the focus of this thesis.

These conditions can be quantitatively described by the Debye length, the plasma parameter and the plasma frequency as laid out in the following sections.

### 1.3.1 The Debye length

The Debye length describes the extent to which a plasma can shield electromagnetic fields within and so remain quasineutral. Consider an infinitely extending plasma with a test charge placed at some point, then what would be the scalar potential  $\phi(\mathbf{x})$  around it? If the plasma had no kinetic energy, the charged particles would arrange themselves immediately adjacent to the test charge and once this equilibrium state was reached there would be no electromagnetic fields present. More realistically, the plasma will have some temperature, likely a very large temperature and so some particles will be able to escape the potential of the test charge and thus leak electromagnetic fields into the plasma bulk. Poisson's equation (equation 1.1b in the static case) reads

$$\epsilon_0 \nabla^2 \phi = -e(Zn_i - n_e), \quad (1.8)$$

where  $\epsilon_0 = 8.854 \times 10^{-12} \text{ F m}^{-1}$  is the permittivity of free space,  $e = 1.602 \times 10^{-19} \text{ C}$  is the charge of an electron,  $Z$  is the plasma ion charge in units of  $e$  and  $n_i$  and  $n_e$  are the number densities of plasma ions and electrons.

Since the electrons are significantly more mobile than the ions due to their lower mass, it is in general the electrons and not the ions that respond to the test charge and the ions can be assumed to provide a constant background of positive charge density. If the number density of electrons follows a Boltzmann temperature distribution in the presence of a potential energy  $-e\phi$ , then

$$n_e = n_{e,0} e^{e\phi/KT_e}, \quad (1.9)$$

where  $n_{e,0}$  is the electron number density far from the test charge,  $n_i = n_{e,0}/Z$ ,  $K = 1.38 \times 10^{-23} \text{ J K}^{-1}$  is the Boltzmann constant and  $T_e$  is the electron temperature in Kelvin. Note that in plasmas it is very common for different species to have differing temperatures depending on the mechanism for energy absorption and the timescales for collisions compared to the timescale of the study.

Substituting equation 1.9 into equation 1.8 and Taylor expanding the exponential term in the limit that the plasma is weakly coupled ( $e\phi \ll KT_e$ ),

$$\nabla^2\phi = \frac{\phi}{\lambda_D^2}, \quad (1.10)$$

where

$$\lambda_D \equiv \sqrt{\frac{\epsilon_0 K T_e}{n_e e^2}}, \quad (1.11)$$

is the *Debye length* and describes the thickness of the charge sheath surrounding the test charge. For quasineutrality to hold for the plasma bulk, its spatial dimensions,  $L$ , must extend beyond a few Debye lengths, *i.e.*

$$L \gg \lambda_D. \quad (1.12)$$

### 1.3.2 The plasma parameter

In order for the derivation of section 1.3.1 to be statistically valid, there must be a large number of charged particles within the shielding sheath. The number of particles within the *Debye sphere* is

$$N_D = \frac{4}{3}\pi\lambda_D^3 n, \quad (1.13)$$

where,  $N_D$  is the *plasma parameter*. Note that, as discussed above, in most cases it is most suitable to choose the number density  $n$  to be the number density of electrons,  $n_e$ . To ensure the plasma is suitably ionised (criterion 1) and that the plasma engages in collective behaviour (criterion 3),

$$N_D \ggg 1. \quad (1.14)$$

### 1.3.3 Collisionality and the plasma frequency

Collective behaviour not only depends on the ability for large numbers of particles to interact via electromagnetic forces but also that these forces dominate over collisions in describing particle trajectories. Taking  $\omega$  as the typical frequency of plasma oscillations and  $\tau$  as the average time between collisions, for a plasma (as opposed to a gas)

$$\omega\tau > 1 \quad (1.15)$$

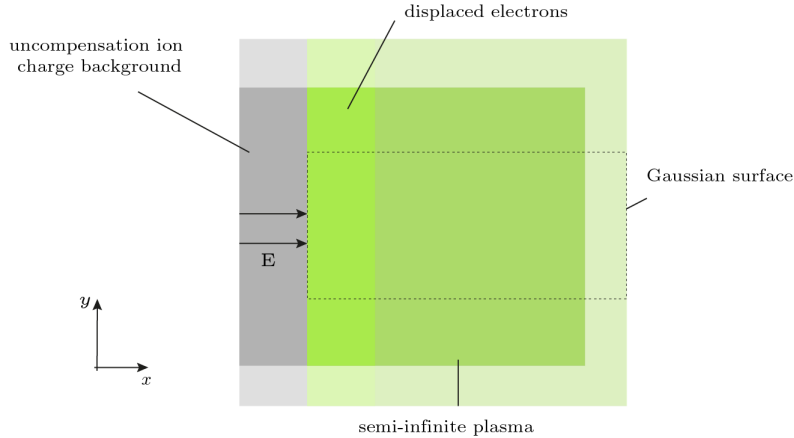


**Figure 1.2:** The electrons of a semi-infinite plasma are displaced inwards by some external force leaving in their wake an uncompensated space charge of ‘immobile’ positive ions. By constructing a Gaussian surface along the dashed line, using Gauss’ Law, the electric field associated with the positive space charge can be calculated.

is required. It now remains to determine what is the typical frequency of collisions in a given plasma. While the types of plasma waves and their associated frequencies of oscillation are multitudinous, the characteristic frequency, the *plasma frequency*,  $\omega_p$ , is the most straightforward. It describes the response of electrons to charge imbalances within an infinite uniform plasma at rest in the absence of magnetic fields or temperature fluctuations. As noted in section 1.3.1, the ions provide a constant background of positive charge.

Consider a semi-infinite plasma existing for  $x > 0$ , with electron density  $n_e$  and ion density  $n_e/Z$  of charge state  $Z^1$ . Suppose the electron fluid is displaced by some perfectly isotropic force into the plasma bulk a distance  $(\Delta x)\hat{\mathbf{x}}$  as in figure 1.2. The total charge of displaced electrons within a surface area of  $\sigma$  is

$$Q = -en_e\sigma\Delta x. \quad (1.16)$$

Applying the integral form of Gauss’ law (from equation 1.1b) to the surface detailed in figure 1.2, the uncompensated charge leads to

$$-\sigma E\hat{\mathbf{x}} = \frac{Q}{\epsilon_0}\hat{\mathbf{x}} = -\frac{en_e\sigma\Delta x}{\epsilon_0}\hat{\mathbf{x}} \quad (1.17)$$

---

<sup>1</sup>This description has direct relevance to the Zero Vector Potential mechanism which will be made clear in chapter 2.

at the electron surface. By the Lorentz force, equation 1.2, the displaced electrons will experience a restoring force,  $-eE\hat{x}$ , perpendicular to the surface due to the electron-ion charge imbalance. The equation of motion for electrons on that surface is therefore

$$m_e \frac{d^2\Delta x}{dt^2} = -eE = -\frac{e^2 n_e}{\epsilon_0} \Delta x. \quad (1.18)$$

Equation 1.18 clearly describes a simple harmonic oscillator with a characteristic frequency given by the plasma frequency,

$$\omega_p = \sqrt{\frac{e^2 n_e}{m_e \epsilon_0}}. \quad (1.19)$$

## 1.4 The Lawson-Woodward theorem

The Lawson-Woodward theorem states that there can be no net electron energy gain using laser fields [76], quite at odds with one of the primary aims of this thesis, that is, the acceleration of electrons. There are, however, several conditions that must be met, namely,

1. The interaction region is infinite;
2. The interaction occurs in a vacuum;
3. The electron is ultra-relativistic ( $v \approx c$ ) along the acceleration gradient;
4. No electro- or magnetostatic fields are present;
5. Non-linear effects are neglected.

Several of these will be applicable to the various accelerations of electrons considered. It is this final condition that is most damning to the application of the theorem. Throughout this thesis, the ultra-relativistic laser pulses under consideration ensure non-linear effects cannot be neglected. It is indeed such non-linearities that are of most interest.

## 1.5 Laser-solid density plasma linear interaction

Consider small transverse electromagnetic waves propagating through a plasma. Linearising equation 1.2 for a single plasma electron by assuming only small field variations and thus small velocity variation,

$$m_e \dot{\mathbf{v}}_e = -e\mathbf{E}. \quad (1.20)$$

Combining the time derivative of equation 1.1c and the curl of equation 1.1d,

$$\nabla \times \nabla \times \mathbf{E} = -\mu_0 \dot{\mathbf{J}} - \mu_0 \epsilon_0 \ddot{\mathbf{E}}. \quad (1.21)$$

Considering only fast oscillations such that ions are effectively immobile,

$$\mathbf{J} = -n_e e \mathbf{v}_e \quad (1.22)$$

and using the identity  $\nabla \times \nabla \times \mathbf{E} = \nabla(\nabla \cdot \mathbf{E}) - \nabla^2 \mathbf{E}$ ,

$$\nabla(\nabla \cdot \mathbf{E}) - \nabla^2 \mathbf{E} = -\frac{\mu_0 n_e e^2}{m_e} \mathbf{E} - \mu_0 \epsilon_0 \ddot{\mathbf{E}}. \quad (1.23)$$

Assuming plane wave solutions of the form

$$\mathbf{E} = \mathbf{E}_0 e^{i(\mathbf{k} \cdot \mathbf{x} - \omega t)}, \quad (1.24)$$

where  $\mathbf{k}$  is the wave-vector and  $\omega$  the frequency of oscillations and noting the waves are transverse  $\mathbf{k} \cdot \mathbf{E} = 0$ ,

$$|\mathbf{k}|^2 \mathbf{E} = -\frac{\mu_0 n_e e^2}{m_e} \mathbf{E} + \mu_0 \epsilon_0 \omega^2 \mathbf{E} \quad (1.25)$$

and hence the dispersion relation for electromagnetic waves propagating in a plasma is

$$\omega^2 = c^2 |\mathbf{k}|^2 + \omega_p^2. \quad (1.26)$$

Equation 1.26 exhibits a *cutoff* dependent on the plasma density via  $\omega_p$ . The *critical density*,  $n_c$ , is defined as the density above which a laser pulse of frequency  $\omega_L$  cannot propagate through a plasma. This occurs for  $\omega_L = \omega_p$ , thus,

$$n_c = \frac{m_e \epsilon_0 \omega_L^2}{e^2}. \quad (1.27)$$

As the plane wave has a spatial dependence  $\sim \exp(\mathbf{k} \cdot \mathbf{x})$ , if  $n_e > n_c$ ,  $\mathbf{k}$  is imaginary and the wave no longer propagates through the plasma and instead exponentially attenuates over a skin depth,

$$\delta = \frac{1}{|\mathbf{k}|} = \frac{c}{\sqrt{\omega_p^2 - \omega_L^2}} \quad (1.28)$$

and is reflected. For typical high-power lasers with wavelengths in the visible or near-infrared, fully ionised solids tend to have densities well above the critical density and thus

## 1.6 Relativity

Modern high-power lasers operate in the domain of relativistic mechanics and in general interactions are highly non-linear. It is useful to introduce some of the basic principles of relativity. Note that while there has been growing interest in the curvature of spacetime by relativistic lasers [77], this effect remains undetectable at present. Thus, throughout this thesis, the inner product of 4-tensors is defined using the Minkowski Metric [74].

Many useful quantities can be arranged into contravariant four-vectors that undergo a Lorentz transformation for a change of frame of reference [74], specifically,

$$\mathbf{A}'^\mu = \Lambda_\nu^\mu \mathbf{A}^\mu, \quad (1.29)$$

where  $\Lambda_\nu^\mu$  is the appropriate Lorentz transformation, and primed symbols typically denote boosted frames of reference. Without loss of generality, the coordinate system can be defined such that the boosted frame travels along the  $\mathbf{x}$ -axis with respect to the initial frame. Thus, the Lorentz transformation is defined

$$\Lambda_\mu^\nu = \begin{pmatrix} \gamma & -\beta\gamma & 0 & 0 \\ -\beta\gamma & \gamma & 0 & 0 \\ 0 & 0 & 1 & 0 \\ 0 & 0 & 0 & 1 \end{pmatrix}. \quad (1.30)$$

Generally, a *beta factor* is a normalised speed or velocity of an object,

$$\beta = \frac{v}{c}, \quad (1.31)$$

Symbol	Name	Components	Invariant
$\mathbf{X}^\mu$	4-displacement	$(ct, \mathbf{x})$	$-c^2\tau^2$
$\mathbf{A}^\mu$	4-potential	$(\phi/c, \mathbf{A})$	
$\mathbf{J}^\mu$	4-current density	$(c\rho, \mathbf{J})$	$-c^2\rho_0^2$
$\mathbf{K}^\mu$	4-wave vector	$(\omega/c, \mathbf{K})$	
$\mathbf{P}^\mu$	4-momentum	$(U/c, \mathbf{p})$	$-m^2c^2$

**Table 1.1:** Four-vectors of relevance to this thesis. New parameters are the proper time,  $\tau$ , the proper charge density,  $\rho_0$ , energy,  $U = \gamma mc^2$ , three-momentum,  $\mathbf{p} = \gamma m\mathbf{v}$ .

here it refers to the frame velocity and its associated Lorentz or *gamma factor* is

$$\gamma = \frac{1}{\sqrt{1 - \beta^2}}. \quad (1.32)$$

Four-vectors relevant to this thesis are listed in table 1.1. Transformations of electromagnetic fields under reference frame boosts are given in appendix A.1 and Maxwell's equations are Lorentz covariant.

Focusing now on the 4-potential  $\mathbf{A}^\mu$ , choosing the Lorenz gauge,

$$\partial_\mu \mathbf{A}^\mu = \nabla \cdot \mathbf{A} + \frac{1}{c^2} \partial_t \phi = 0, \quad (1.33)$$

then Maxwell's equations can be written

$$\partial_\nu \partial^\nu \mathbf{A}^\mu = -\frac{1}{c^2 \epsilon_0} \mathbf{J}^\mu. \quad (1.34)$$

Equation 1.34 can then be solved to yield

$$\mathbf{A}(\mathbf{x}, t) = \frac{\mu_0}{4\pi} \int \frac{\mathbf{J}(\mathbf{x}', t_a)}{|\mathbf{x} - \mathbf{x}'|} d^3 \mathbf{x}', \quad (1.35)$$

where  $t_a = t - |\mathbf{x} - \mathbf{x}'|/c$  is the advanced time.

### 1.6.1 Ultra-relativistic similarity theory

Consider a relativistically intense laser pulse normally incident on a collisionless plasma as in figure 1.2 and neglect ion motion. The electron distribution is fully described by the Vlasov equation (equation 1.5) with the self-consistent electric

and magnetic fields satisfying Maxwell's equations (equations 1.1). Suppose the incident laser pulse has an initial vector potential

$$\mathbf{A}(t = 0) = \mathbf{a}((y^2 + z^2)/R^2, x/c\tau) \cos k_L x. \quad (1.36)$$

This envelope form for the potential,  $\mathbf{a}((y^2 + z^2)/R^2, x/c\tau)$ , is sensible provided  $k_L R \gg 1$  and  $\omega_L \tau \gg 1$ , where  $R$  is the focal spot radius and  $\tau$  the pulse duration. For fixed laser envelope, the laser-plasma dynamics depend on just four dimensionless variables: the normalised focal spot size,  $k_L R$ , the normalised pulse duration,  $\omega_L \tau$ , the normalised laser vector potential amplitude

$$a_0 = \max \left| \frac{e\mathbf{a}}{m_e c^2} \right|, \quad (1.37)$$

in terms of the peak laser electric field amplitude  $\mathbf{E}_L$ ,

$$a_0 = \frac{e|\mathbf{E}_L|}{m_e c \omega_L}, \quad (1.38)$$

and the normalised plasma density

$$\bar{n}_e = \frac{n_e}{n_c}. \quad (1.39)$$

By normalising the system of equations, details given in the appendix, and combining these last two expressions into the *relativistic similarity parameter*,

$$S = \frac{\bar{n}_e}{a_0}, \quad (1.40)$$

it is possible to show that in the ultra-relativistic limit ( $a_0 \gg 1$ ), the dynamics of the system are similar for constant  $S$  [78] with plasma electrons following similar trajectories where

$$\mathbf{p} \sim a_0. \quad (1.41)$$

There is also a more physical meaning to the  $S$  parameter. Consider again section 1.5 on the propagation of linear electromagnetic waves through a plasma but now for the case of an ultra-relativistic laser pulse. For an electron rotating in an electromagnetic field,

$$\mathbf{F}_\perp = \gamma m_e \mathbf{a}_\perp, \quad (1.42)$$

where  $\mathbf{a}_\perp$  is the acceleration perpendicular to the motion and thus the response of the electrons is reduced by a factor of  $\gamma$ . While some find the *relativistic mass* correction to be somewhat unhelpful nomenclature for the phenomenon [74], it has nevertheless become commonplace within the literature of relativistic plasma physics [70]. Turning the handle, one finds that the relativistic plasma frequency is

$$\omega_p^{\text{rel}} = \sqrt{\frac{e^2 n_e}{\gamma m_e \epsilon_0}}. \quad (1.43)$$

Using equation 1.41, and taking  $v \approx c$ , then  $\gamma \approx a_0$  and the normalised relativistic cutoff density is simply  $S$ . Thus, the ultra-relativistic similarity parameter is just a measure of the overdensity of a plasma once relativistic corrections have been applied, *i.e.* for  $S > 1$ , a laser pulse will be reflection, however for  $\bar{n}_e > 1$  and  $S < 1$ , one enters the regime of relativistically self-induced transparency [79]. It is now possible to define the parameter space of interest in this thesis: relativistic laser-plasma surface interactions occur for  $a_0 \gg 1$  and  $S > 1$ .

### 1.6.2 Relativistic lasers and plasmas

The descriptor *relativistic* is applied liberally in this thesis. When applied to electromagnetic fields or laser pulses it refers to

$$a_0 \geq 1. \quad (1.44)$$

When applied to particles, their Lorentz factors are

$$\gamma = \frac{1}{\sqrt{1 - \beta^2}} \geq 2, \quad (1.45)$$

corresponding to a speed,  $u \geq 0.87c$ . *Ultra-relativistic* implies these quantities are much larger than the conditions provided. A relativistic laser pulse will accelerate electrons to relativistic velocities in a fraction of a laser pulse cycle. Consider an electron in the presence of a uniform electric field of magnitude  $a_0 = 100$ , an intensity accessible by current state-of-the-art laser facilities. The work done on that particle by the field is

$$T = (\gamma - 1)m_e c^2 = \int \mathbf{E} \cdot d\mathbf{x}, \quad (1.46)$$

The field will accelerate an electron to relativistic velocities in a distance less than 1 % of a corresponding laser pulse wavelength.

Upon entrance to the relativistic regime, the motion of an electron fundamentally changes. Consider Equation 1.2. For non-relativistic laser pulses, the magnetic field component can be neglected and the electron will simply oscillate along the electric field vector direction. Once electron velocities approach  $c$ , this approximation is no longer valid, electron velocities are rotated in the magnetic field and are accelerated along the laser propagation direction. In a plasma, this enables compression of a surface since ions are accelerated inwards in longitudinal electric fields from the induced electron-ion separation.

### 1.6.3 Conservation of generalised transverse momentum

Consider a holonomic system of  $N$  relativistic particles under the influence of electromagnetic forces. A particle  $j$  with charge  $e_j$  and mass  $m_j$  experiences a scalar potential,

$$V_j = e_j(\phi - \mathbf{A} \cdot \mathbf{v}_j) \quad (1.47)$$

and hence the system is described by the Lagrangian [80]

$$\mathcal{L} = \sum_{j=1}^N \left( -m_j c^2 \sqrt{1 - \beta_j^2} - e_j(\phi - \mathbf{A} \cdot \mathbf{v}_j) \right), \quad (1.48)$$

The generalised momentum corresponding to coordinate  $x_j$  is

$$p_{j,x} = \frac{\partial L}{\partial \dot{x}_j} = \frac{m_j \dot{x}_j}{\gamma_j} + e_j A_x, \quad (1.49)$$

thus, the generalised momentum describes both the linear mechanical momentum and the momentum of the electromagnetic field. Via Noether's theorem, if  $L$  is independent of  $x_j$ , *i.e.* spatially homogeneous along  $x$  for particle  $j$ , then

$$\dot{p}_{j,x} = 0 \quad (1.50)$$

since

$$\frac{d}{dt} \left( \frac{\partial L}{\partial \dot{x}_j} \right) = \frac{\partial L}{\partial x_j}. \quad (1.51)$$

Taking the Lorenz gauge, consider a linearly polarised Gaussian laser pulse, with an axis of polarisation along  $x$  incident on a solid target at rest. Then  $A_x$  is approximately constant along  $x$  near the beam centre<sup>2</sup>. Integrating equation 1.50, fully constraining the gauge by setting the potential to zero initially, and noting that there is no linear momentum at the target, the generalised transverse momentum conservation equation for an electron in the laser field is

$$p_T = eA, \quad (1.52)$$

where  $p_T$  is the electron momentum along the polarisation axis of the laser pulse and  $A$  is the laser pulse 3-vector potential amplitude. As a sanity check, this expression complies with the ultra-relativistic similarity result of equation 1.41.

Note that this is only valid provided the electron does not radiate along the direction of polarisation as discussed by Sokolov *et al* [81]. The implications of *Radiation Reaction* are discussed in the following section.

## 1.7 QED effects

Next-generation laser facilities will enable the testing of decades-old theoretical predictions of Strong-Field Quantum Electro-Dynamics (SF-QED). Already Fedeli *et al* have shown in simulations that current PW-class laser facilities can access the regime using an all-optical set-up based on laser-solid surface interactions [82]. The Schwinger Limit  $E_S = 1.32 \times 10^{18} \text{ V m}^{-1}$  is the field intensity at which the vacuum becomes non-linear. If by some means an electron can be directed towards a plane electromagnetic wave, by consideration of the Lorentz transformations of electromagnetic fields (equations A.1), it is possible that provided the electron is sufficiently relativistic, in its own frame of rest it will ‘see’ electromagnetic fields intense enough to access vacuum non-linearities. The first two frontiers of SF-QED that will be accessible are Radiation Reaction and multi-photon Breit-Wheeler electron pair production. Brief introductions to these phenomena are now presented.

---

<sup>2</sup>Constant relative to the scale of typical electron trajectories in such an interaction.

### 1.7.1 High-energy photon emission and radiation reaction

When a charged particle undergoes an acceleration, it emits electromagnetic radiation. If the electromagnetic field is sufficiently strong, *i.e.* approaching the Schwinger Limit in the rest frame of the particle, then a non-negligible fraction of the particle momentum can be transferred to the emitted high energy photon, substantially impacting the dynamics of the accelerated particle. This back reaction is known as Radiation Reaction (RR).

Smilei (detailed in the following section) implements the process of high-energy photon emission as Inverse Compton Scattering on the basis of several assumptions [83], namely,

1. radiating particles are ultra-relativistic and therefore radiation is emitted in the direction of travel of the particle;
2. the field varies slowly over the timescale of photon emission, this is the *locally-constant field approximation* and requires ultra-relativistic field strengths;
3. but they are small with respect to the Schwinger Limit, specifically requiring the invariants  $\sqrt{c^2\mathbf{B}^2 + \mathbf{E}^2}$  and  $\sqrt{c\mathbf{B} \cdot \mathbf{E}} < E_S$ ;
4. real particles radiated independently of their neighbours, this requires the emitted wavelength to be shorter than the typical inter-particle spacing.

Provided such conditions hold, the rate of photon emission depends on two invariants [84], the electron quantum parameter

$$\chi = \frac{\gamma}{E_S} \sqrt{(\mathbf{E} + \mathbf{v} \times \mathbf{B})^2 - (\mathbf{v} \cdot \mathbf{E})^2/c^2}, \quad (1.53)$$

where  $\mathbf{v}$  is the electron velocity and the emitted photon quantum parameter

$$\chi_\gamma = \frac{\gamma_\gamma}{E_S} \sqrt{(\mathbf{E}_\perp + \mathbf{c} \times \mathbf{B})^2 - (\mathbf{c} \cdot \mathbf{E})^2/c^2}, \quad (1.54)$$

where  $\gamma_\gamma$  is the normalised photon energy =  $\hbar\omega_\gamma/m_e c^2$ . The exact relationship is complex and in the the fully quantum domain ( $\chi > 1$ ), is it not practical to solve the integrations required for all particles. Instead, values are extracted from precalculated tables and into a Monte Carlo algorithm.

### 1.7.2 Multi-photon Breit-Wheeler pair production

Multi-photon Breit-Wheeler pair production, also known as non-linear Breit-Wheeler is the decay of a high energy photon, typically produced via RR, into an electron-positron pair in the presence of a strong electromagnetic field, explicitly,

$$\gamma + n\omega \rightarrow e^- + e^+. \quad (1.55)$$

The strength of the effect is dependent on the Lorentz invariant photon quantum parameter, equation 1.54 Cite Smilei and say, in a constant E-field, the rate of pair production increases rapidly up to  $\chi_\gamma \approx 10$  at which point it saturates and slowly reduces.

## 1.8 Simulating the interaction

Modelling laser-plasma interactions is a notoriously challenging endeavour; due to the complexity of the many-bodied systems involved (a fully ionised centimetre cubed block of plastic contains on the order of  $10^{23}$  particles) and the stochasticity of particle motion, it is frequently impossible to construct models *ab initio*. Instead, hydrodynamic simulation codes such as HYADES [85] and FLASH [86] and Particle-In-Cell simulation codes such as Smilei [75], Osiris [87] and EPOCH [88] are used to construct phenomenological models and to direct experimentation.

### 1.8.1 Supercomputing resources

Modern High Performance Computing (HPC) systems are poised to enter the exascale regime ( $> 10^{18}$  Floating Point Operations Per Second). With limited improvements in microprocessor technologies, such power is achieved through massive parallelisation across processing units. To enable the study of the dynamics of up to billions of macroparticles, PIC codes test the limits of current supercomputing architectures. ARCHER2, the UK's national supercomputer came online in November 2021, with it delivering over ten times the resources of its predecessor (ARCHER) [89]. An HPE Cray EX supercomputing system with a peak performance estimated at  $28 \text{ Pflops s}^{-1}$  across 5860 nodes each with dual AMD

EPYCTM 7742 64-core processor for a total of 750,080 cores, ARCHER2 was able to supply the resources required to run the costly PIC simulations for this research. The substantially cheaper HYADES simulations were performed using the Rutherford Appleton Laboratory's SCARF HPC cluster [90].

### 1.8.2 Particle-In-Cell codes

#### Discretisation of the Vlasov-Maxwell equations

Finding numerical solutions to the Vlasov-Maxwell equations is no straightforward task, while codes exist that are capable, such as Valis [91], the requirement of high resolution in both position and momentum is exceedingly costly and the use of such codes is limited with respect to their size, duration and spatial dimensions. A more tractable approach is to discretise the distribution function into  $N_s$  *quasi-particles*<sup>3</sup>. These are often referred to as *macro-particles* in practice and typically represent a large number of real particles, such that

$$f_s(t, \mathbf{x}, \mathbf{p}) = \sum_{p=1}^{N_s} w_p S(\mathbf{x} - \mathbf{x}_p(t)) \delta(\mathbf{p} - \mathbf{p}_p(t)), \quad (1.56)$$

where  $w_p$  is the quasi-particle's weight,  $\mathbf{x}_p$  and  $\mathbf{p}_p$  are its position and momentum respectively,  $\delta$  is the Dirac-delta distribution and  $S(\mathbf{x})$  the shape-function chosen to represent the quasi-particle. The Vlasov equation is then integrated along the continuous trajectories of the quasi-particles while Maxwell's equations are solved on a discrete spatial grid of *cells*. Such a code is aptly named a *Particle-In-Cell* (PIC) code. A schematic of the standard PIC code algorithm is presented in figure 1.3. After particle and field initialisation, fields are interpolated at particle positions. The well-established momentum-conserving *Boris pusher* algorithm computes the new macro-particle velocities and positions [93]. Particles are advanced in time using a *leap-frog* scheme, where positions are defined at integer,  $n$ , time steps and momenta at half-integer,  $n + 1/2$ . The charge conserving Esirkepov algorithm [94] projects the new charge and current densities onto the grid to then solve Maxwell's equations on the grid using the Finite-Difference-Time-Domain approach [95]. To

---

<sup>3</sup>Originally introduced by Langdon and Birdsall as *clouds* [92].

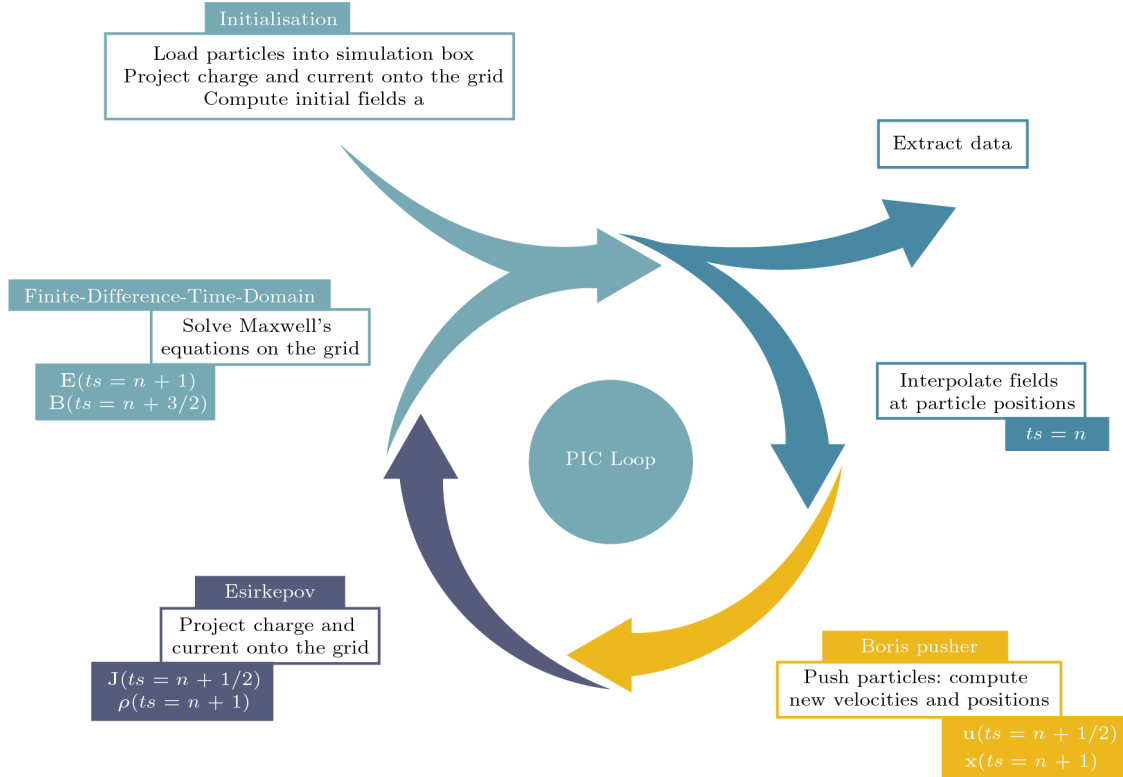


**Figure 1.3:** A schematic of the PIC code loop and the algorithms performed from time step,  $ts$ , from  $n$  to  $n + 1$ .

ensure space and time centring of the electromagnetic field derivatives in Maxwell's equations, electric and magnetic fields are discretised on the staggered *Yee grid* as represented in figure 1.4. with electric fields defined at integer time steps and magnetic fields at half-integer time steps.

## Smilei

Smilei (for Simulating Matter Irradiated by Light at Extreme Intensities) is a modern collaborative, massively parallel, fully relativistic and open source plasma physics PIC code and the major workhorse for this thesis<sup>4</sup>. Produced by M. Grech's team(CHECK THIS) at École Polytechnique [75], its recent development was motivated by the rapid advancements of multi-petawatt facilities both globally and locally with the recent completion of the 10 PW Apollon laser facility and by the availability of supercomputing power which has ‘skyrocketed’ in recent years [75].

<sup>4</sup>At points benchmarks against the EPOCH and Osiris PIC codes were performed.

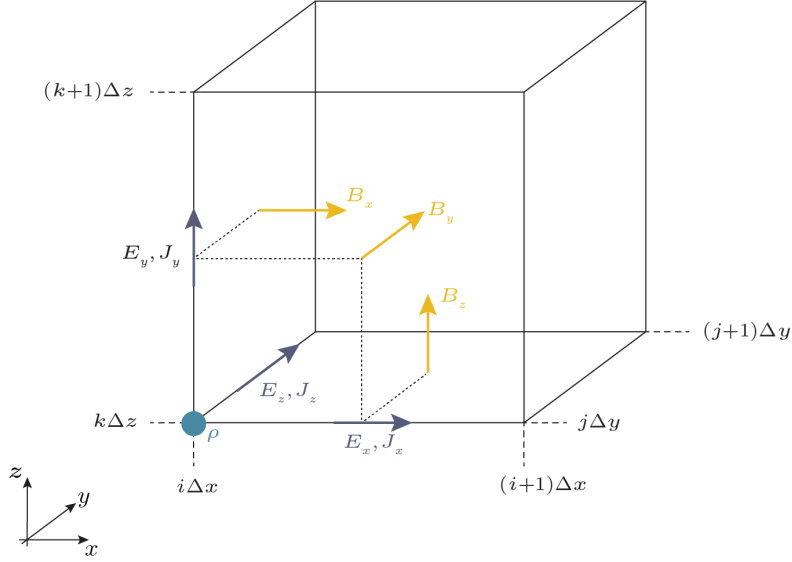


**Figure 1.4:** A representation of the staggered 3D Yee grid for the cell at  $(i\Delta x, j\Delta y, k\Delta z)$  for spatial centring of the curl operations, including the locations where all system properties are defined.

Indeed, the 3D PIC simulations discussed in this thesis required the parallelisation of almost 20 % of the computing resources available on ARCHER2.

## Reference units

Given the broad range of magnitudes linked to multi-petawatt and femtosecond laser pulses, solid density plasmas, micrometre wavelengths, and attosecond electron bunches, it becomes significantly more convenient to transform them into dimensionless normalised values. Smilei operates in such units. This normalisation is not chosen *a priori*, instead results can be scaled by an arbitrary reference angular frequency. This is extremely useful when working with boosted frames of reference. As this thesis focuses on the interaction of a laser pulse with plasma, the laser pulse angular frequency,  $\omega_L$  is set as the frequency of reference. A list of the most common normalisations is given in table 1.2.

## Simulation parameters

*Silver-Müller* boundary conditions for the simulation box edges [96] are able to absorb and inject electromagnetic waves and particles. Note that there can be non-physical reflection of electromagnetic waves at such boundaries leading to some error.

Units of	SI units	Normalisation
velocity	$\text{m s}^{-1}$	$c$
charge	C	$e$
mass	kg	$m_e$
momentum	$\text{kg m s}^{-1}$	$m_e c$
energy/temperature	J	$m_e c^2$
time	s	$\omega_L^{-1}$
length	m	$c/\omega_L$
number density	$\text{m}^{-3}$	$n_c$
electric field	$\text{V m}^{-1}$	$m_e c \omega_L / e$

**Table 1.2:** Smilei normalisations for common quantities with the laser angular frequency  $\omega_L$  set at the reference angular frequency.

The quasi-particle shape function  $S(\mathbf{x})$  determines the projection of particle charge onto the grid. It is symmetric in all dimensions with respect to  $\mathbf{x}$  and extends over  $n$  cells of width  $\Delta x$  in each direction where  $n$  is the interpolation order. It can be written as a product across  $D$  dimensions,

$$S(\mathbf{x}) = \prod_{\mu=1}^D s^{(n)}(x^\mu). \quad (1.57)$$

Smilei implements orders 2, 3 and 4, the explicit shape functions are

$$s^2(n) = \begin{cases} \frac{1}{\Delta x} \left( 1 - \left| \frac{x}{\Delta x} \right| \right) & \text{if } |x| \leq \Delta x, \\ 0 & \text{otherwise,} \end{cases} \quad (1.58a)$$

$$s^3(n) = \begin{cases} \frac{3}{4\Delta x} \left( 1 - \frac{4}{3} \left( \frac{x}{\Delta x} \right)^2 \right) & \text{if } |x| \leq \frac{1}{2}\Delta x, \\ \frac{9}{8\Delta x} \left( 1 - \frac{2}{3} \left| \frac{x}{\Delta x} \right| \right)^2 & \text{if } \frac{1}{2}\Delta x < |x| \leq \frac{3}{2}\Delta x, \\ 0 & \text{otherwise,} \end{cases} \quad (1.58b)$$

$$s^4(n) = \begin{cases} \frac{2}{3\Delta x} \left( 1 - \frac{3}{2} \left( \frac{x}{\Delta x} \right)^2 + \frac{3}{4} \left| \frac{x}{\Delta x} \right|^3 \right) & \text{if } |x| \leq \Delta x, \\ \frac{4}{3\Delta x} \left( 1 - \frac{1}{2} \left| \frac{x}{\Delta x} \right|^3 \right) & \text{if } \Delta x < |x| \leq 2\Delta x, \\ 0 & \text{otherwise.} \end{cases} \quad (1.58c)$$

While the correct implementation of collisions in PIC codes remains an open problem [97], Smilei has implemented relativistic binary collisions between macroparticles using a Monte-Carlo-based scheme [98]. The aforementioned QED processes

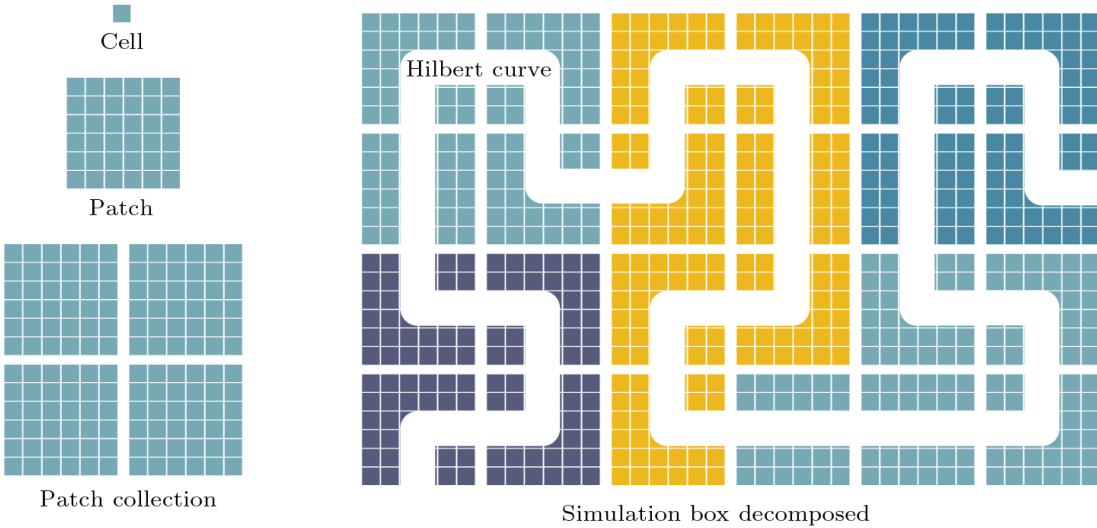


**Figure 1.5:** Smilei simulation box decomposition into cells, patches and MPI patch collections. Cells are grouped into patches, patches are grouped into MPI patch collections. MPI patches are assigned contiguously along the Hilbert curve.

of Inverse Compton scattering and non-linear Breit-Wheeler pair production are included using the built-in Smilei packages [75]. These processes can lead to cascades of many particles being added to the simulations. Macroparticle merging can increase simulation efficiency and reduce the memory footprint. Smilei implements such a scheme, inspired by that designed by Vranic *et al* [99], that is computationally efficient and conserves energy, momentum and charge within a cell. While Smilei contains modules to handle ionisation, with reference to figure 1.1 these are deemed unnecessary for the laser intensities considered in this thesis.

### Parallelisation in practice

In the following discussion, where differences in language occur, objects are given as their ARCHER2 (Smilei) names. The Smilei simulation box consists of a grid of cells as in figure 1.5. The box is decomposed into *patches* consisting of many cells. Patches are arranged into *MPI patch collections* assigned contiguously along a Hilbert curve.

Archer consists of many *CPUs (cores)* that can each perform computational tasks. CPUs are grouped into *nodes*. Memory is shared within a node such that all CPUs (cores) in a node can operate on the same data. When optimised, ARCHER2's memory in each node is split into 8 *sockets*. These 8 sockets each perform a *task*

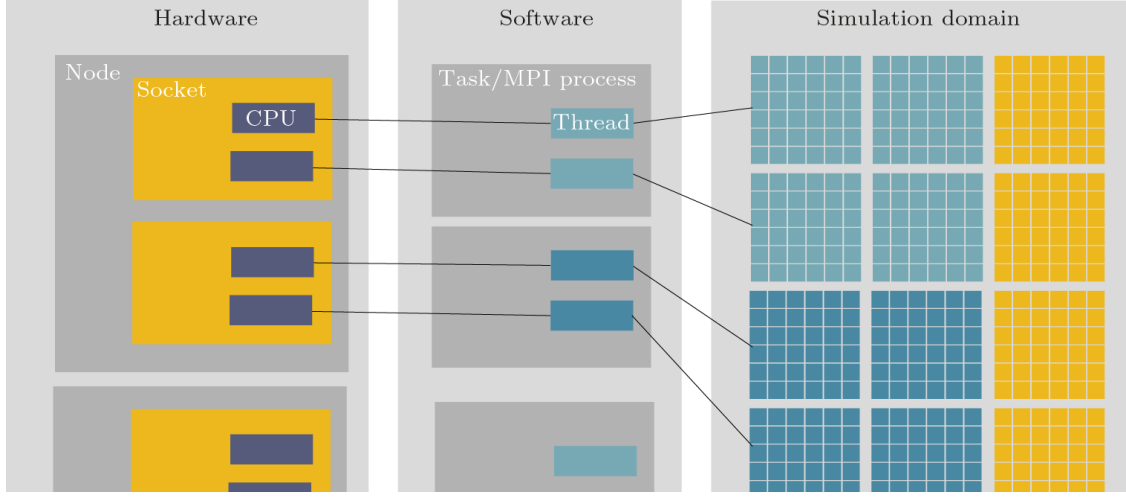


**Figure 1.6:** Representation of the interaction of the ARCHER2 hardware and software components when running Smilei. Each CPU is assigned a thread, each task is carried out by one socket. A task tackles one MPI patch collection with threads working through patches.

(*MPI process*). Each task (*MPI process*) has 16 CPUs (cores) assigned that each perform a *thread*. A thread is a sequence of instructions from the program.

Each task (*MPI process*) handles one *MPI patch collection*. Threads work through patches. Figure 1.6 represents this division of labour. Threads do not need to wait for other threads in their process to tackle new patches in their MPI patch collection. This is a form of local *dynamic load balancing*. If an MPI patch collection is overloaded, a patch is offloaded to a contiguous MPI patch collection.

There are several considerations for simulation optimisation. Tasks (*MPI processes*) should always be assigned more patches than threads. To apply the Hilbert curve, the number of patches in each dimension must be a power of 2. The fewer cells in a patch, the more efficient the load balancing, however, the cost of synchronisation between patches increases, although generally the gain in efficiency from load balancing by increasing patch number will win out at later times with increasing efficiency for increased frequency of load balancing [75]. Note that smaller patches are preferable when there are small regions with large numbers of particles, as in laser-solid surface interactions, however, the minimum patch size is dependent on the shape function of the macro-particles.

### Sources of error inherent to PIC codes

Despite their relatively intuitive interpretation, PIC codes are famously finickety and prone to errors, most notably that of numerical self heating<sup>5</sup>. There are three conditions required for stability.

To ensure stability, or at least to minimise instability, there are several conditions which must be met. Naturally, the time step,  $\Delta t$ , and cell size ( $\Delta x \Delta y \Delta z$ ) must adequately capture all interesting features of a given simulation. Typically such features are plasma wave oscillations,

$$\Delta t \omega_p \ll 1, \quad (1.59)$$

and laser pulse electromagnetic field oscillations or higher order harmonics of the laser pulse if that is of interest, for the  $n$ th harmonic

$$\Delta t \omega_L n \ll 1. \quad (1.60)$$

Note this also ensures that macroparticles are smaller than the wavelengths of the system, a requirement to ensure they mimic real particles [100]. Relativistic PIC codes must satisfy the much-acclaimed [101] Courant-Friedrichs-Lowy condition,

$$\frac{1}{c\Delta t} > \sqrt{\frac{1}{(\Delta x)^2} + \frac{1}{(\Delta y)^2} + \frac{1}{(\Delta z)^2}}, \quad (1.61)$$

thus preventing light and relativistic particles from crossing a cell in one timestep and generating numerical Cerenkov radiation [102]. As with real plasmas and real particles, to avoid numerical charge fluctuation and ensure collective behaviour of macroparticles,

$$\frac{4}{3}\pi\lambda_D^3 n_{\text{macro}} = N_{D,\text{macro}} \gg 1, \quad (1.62)$$

where  $n_{\text{macro}}$  is the macroparticle density [102]. To avoid numerical heating, the cell size must resolve the Debye length,

$$\frac{\lambda_D}{\Delta x} \geq 1, \quad (1.63)$$

---

<sup>5</sup>Standard PIC code algorithms are charge and momentum conserving but not energy conserving [75].

failure to do so may cause plasma self-heating until the Debye length matches the cell size [102]. Interestingly, Brackbill *et al* [103] observed in their simulations that setting  $\lambda_D/\Delta x = 1$  was most effective at reducing spurious heating. Arber *et al* [104] performed extensive simulations exploring this instability. If the Debye length is not resolved, after an initial period of rapid self-heating, the temperature increases linearly and can be modelled as

$$\frac{dT_{\text{eV}}}{dt_{\text{ps}}} = \alpha_H \frac{n_{23}^{3/2} \Delta x_{\text{nm}}^2}{N_{\text{ppc}}}, \quad (1.64)$$

where  $T_{\text{eV}}$  is the temperature in electron volts,  $t_{\text{ps}}$  is the time in picoseconds,  $n$  is the plasma electron number density in units of  $10^{23} \text{ cm}^{-3}$ ,  $\Delta x_{\text{nm}}$  is the cell size in nanometres and  $N_{\text{ppc}}$  is the number of macroparticles per cell with  $\alpha_H$ , the heating coefficient, determined from their simulations. For a top-hat macroparticle shape function, they found  $\alpha_H = 3000$  with an order of magnitude reduction for every increase in order of the shape function and further improvements from using current smoothing techniques. Note that the heating curves are roughly self-similar at all points and thus while equation 1.64 was established in the linear regime only, its scalings remain useful to compare simulations at all times.

The final instability that shall be discussed is the *finite grid instability*. This is the aliasing error associated with particle properties being deposited at grid points. Is most catastrophic for cold drifting plasmas and depends on the *beam Debye length*,

$$B = \frac{u}{\omega_p \Delta x}, \quad (1.65)$$

where  $u$  is the beam speed. While their theory predicts stability for  $B > 0.25$ , Brackbill *et al* [103] observed instability growth for all beam temperatures in their simulations, although they found the percentage error is a small fraction for  $B > 10$ .

### 1.8.3 Hydrodynamic codes

A hydrodynamic code approximates the plasma distribution as a fluid. This is achieved by taking the moments of velocity of the distribution function,  $f_s$  for fluid species  $s$ . The first three return the number density of particles

$$n_s = \int f_s d\mathbf{v}, \quad (1.66)$$

the fluid velocity,  $\mathbf{u}_s$  and momentum,

$$\mathbf{p}_s = m_s n_s \mathbf{u}_s = \int f_s \mathbf{v} d\mathbf{v}, \quad (1.67)$$

and the pressure tensor

$$P_s = m_s \int f_s (\mathbf{v} - \mathbf{u}_s)(\mathbf{v} - \mathbf{u}_s) \mathbf{v}. \quad (1.68)$$

The fluid equations that govern the evolution of these quantities can be extracted from the Vlasov equation, Equation 1.5 by taking the appropriate moments <sup>6</sup>. Likewise producing the continuity equation

$$\frac{\partial n_s}{\partial t} + \nabla \cdot (n_s \mathbf{u}_s) = 0, \quad (1.69)$$

for conservation of particle number and the equation of motion

$$m_s n_s \left( \frac{\partial \mathbf{u}_s}{\partial t} + (\mathbf{u}_s \cdot \nabla) \mathbf{u}_s \right) = q_s n_s (\mathbf{E} + \mathbf{u}_s \times \mathbf{B}) - \nabla \cdot P_s \quad (1.70)$$

for conservation of momentum. This equation is analogous to the Navier-Stokes equation except for the addition of the electromagnetic fields. The viscosity term is bundled into the pressure tensor [73].

Here lies a problem. The presence of the pressure tensor in Equation ?? prevents the closure of the system of equations. Taking the second moment of the Vlasov equation to obtain the energy transport equation would then contain the third moment of the distribution function presenting the same issue. Instead, a *closure relation* is introduced, enabling the construction of a self-contained theory using a finite number of moments.

HYADES is a 1D three fluid (electrons, ions and radiation) radiative hydrodynamic code [85] and is the code of choice in this thesis. The equations of mass and energy transport are solved in a Lagrangian coordinate system, *i.e.*, unlike strictly Eulerian PIC codes, the mesh defining regions of the simulation moves with the plasma it describes. To complete the system to the second moment, the

---

<sup>6</sup>Of course, these equations can also be derived by first principles by considering the dynamics of a fluid element [73]

Parameter	ORION	GEMINI	
Beamlines	SP1	SP2	N & S
Power (PW)	0.5	1	0.5
Energy (J)	200	500	12
Wavelength (nm)	527	1053	800
Parabola, $f/\#$	$f/3$	$f/3$	$f/2$
Focal spot FWHM ( $\mu\text{m}$ )	< 20	< 10	2
Duration (fs)	500	500	40
Shot rate	5/day	5/day	3/min
Peak $a_0$ (approx)	10	30	24

**Table 1.3:** The ORION and GEMINI petawatt class short pulse beamlines for comparison. The GEMINI North (N) and South (S) beamlines are equivalent.

*equation of state*, describing pressure in terms of the temperature and density of the system, and the heat transfer equation are added.

The reduction of dimensionality achieved through this approximation dramatically reduces the computational cost of the simulation. However, much of this thesis relies on the precise velocity distribution of particles, naturally such a code cannot model these phenomena and the primary tool is the PIC code.

## 1.9 Powering the interaction

Two experiments are discussed in this thesis, one performed on ORION, and one planned on GEMINI. Their typical beam parameters are presented in Table 1.3. The GEMINI-PW laser facility of the Central Laser Facility (CLF) at Harwell Campus, Oxfordshire is a petawatt class facility consisting of two 30 fs beams, **N!** (**N!**) and **S!** (**S!**), each delivering a maximum focused intensity of  $2 \times 10^{21} \text{ W cm}^{-2}$  at a repetition rate of 0.05 Hz. Such a high frequency of operation has led to a paradigm shift in high-power laser physics experimentation with the arrival of statistically significant results.

The ORION SP1 is produced by passing the SP2 through two frequency doubling crystals creating two equivalent beamlets that are then overlaid at the target. The

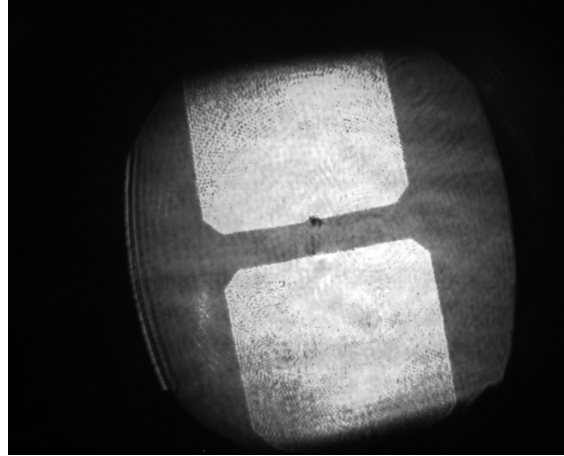


**Figure 1.7:** Image of the ORION SP1 double beamlet structure in the near-field. The two beamlets are then superimposed on the target.

Pedestal, $i$	$I_{0,i}$	$t_i$
Main pulse, p	1	0.2 ps
Picosecond pump residual, pp	$10^{-3}$	3 ps
Picosecond pedestal, ps	$5 \times 10^{-5}$	8 ps
Nanosecond pedestal, ns	$10^{-11}$	3 ns

**Table 1.4:** The native ORION SP2 pulse and prepulse pedestal constants as defined in Equation 1.68.

double beamlet structure at the near-field is imaged in Figure 1.7.

The ORION SP2 beamline intensity temporal profile can be modelled as

$$I_{\text{SP2}} \sim (I_{0,p} \operatorname{sech}(t/t_p)^2 + I_{0,pp} e^{-(t/t_{pp})^2} + I_{0,ps} e^{-\operatorname{abs}(t)/t_{ps}} + I_{0,ns} e^{-(t/t_{ns})^8}), \quad (1.71)$$

where the constants are detailed in Table 1.4 [174]. The picosecond pump residual arises from parametric fluorescence in the ps OPA, the picosecond pedestal from scatter in the stretchers and noise on the OPA pump laser and the nanosecond pedestal from parametric fluorescence from the nanosecond OPAs. The SP1 temporal intensity profile is

$$I_{\text{SP1}} \sim (I_{\text{SP2}}^2 + I_{\text{SP2}} \times 10^{-8}). \quad (1.72)$$

The second term is due to the limitations of the harmonic separation system. The frequency doubling mechanism is not 100 % efficient, *i.e.* some of SP2 beamline

remains and must be filtered out. The main pulse of the GEMINI beamlines is more appropriately modelled as a Gaussian.

### **1.9.1 Laser contrast**

# 2

## The Zero Vector Potential Absorption Mechanism

### Contents

---

<b>2.1</b>	<b>Motivations and an overview</b>	<b>31</b>
<b>2.2</b>	<b>Introduction</b>	<b>33</b>
2.2.1	ZVP electron bunch energies	40
2.2.2	ZVP bunches oblique incidence scaling	43
2.2.3	Defining characteristics of the ZVP mechanism	46
<b>2.3</b>	<b>Numerical simulations of the ZVP mechanism</b>	<b>46</b>
2.3.1	The ZVP mechanism in 3D3V	47
<b>2.4</b>	<b>The ZVP electron bunch</b>	<b>53</b>
2.4.1	Energy absorption in the ZVP regime	63
2.4.2	Unpacking the QED effects of Figure 2.12	66
2.4.3	Errors	68
<b>2.5</b>	<b>Conclusions</b>	<b>69</b>

---

### 2.1 Motivations and an overview

Throughout the history of experimental science, light has always been the primary tool of investigation and discovery. Through the creation of synchrotron radiation sources and more recently XFELs, electron bunches have been employed to create increasingly specialised light sources for the study of matter of all kinds. At SLAC, the United States' forefront electron accelerator, applications hail from many

disciplines: science, medicine, industry and homeland security. At Diamond Light Source, the UK's national synchrotron science facility, studies range from novel drugs to ancient paintings. Unsurprisingly, extensive research efforts have been enlisted to produce electron bunches of ever greater charge, energy and coherency. Multi-petawatt laser facilities are now available across the globe for the study of laser-plasma interactions in the ultra-relativistic regime  $a_0 \gg 1$ . Here, there is a novel method for high-charge electron bunch creation. Via relativistic effects, a laser pulse organises the electrons at the surface of a solid-density plasma into coherent bunches that can be ejected at high speeds. Those discussed in this thesis have properties comparable to those of forefront accelerators but on ultra-short timescales. The quality, charge and duration of the attosecond electron bunches described here would enable the study of the most fundamental interactions of our universe. Electron bunch formation from solid targets has received much interest in recent years [105–112] with some experimental evidence for attosecond electron bunches from intense laser-solid interactions [113–115]. This interest stems partially from their ability to produce higher charge bunches at lower intensities compared to gas targets [113]. Here is proposed a new mass-limited target setup to generate electron bunches of extreme charge density. These electron bunches are fully characterised in 3D PIC simulations to compare their quality to those of existing electron bunch production methods. Their energies are described via an extended version of the ZVP Mechanism and the corresponding implications for laser to plasma energy absorption are also considered including the intersection of ZVP with SF-QED effects of next-generation laser facilities. ZVP theory has direct relevance to High Harmonic Generation (HHG) due to the known intrinsic link between electron bunches and the reflection mechanism [116, 117].

These results have excited the community to perform experiments to realise these electron bunches for the creation of ultra-bright X-ray pulses: after the recent successful campaign at the ORION laser facility, studying HHG from such electron bunches, details are presented here for the upcoming experiment to observe the electron bunches directly at the GEMINI PW laser at the Central Laser Facility, UK.

This Chapter is organised as follows. Section 2.2 outlines the ZVP mechanism including quantitative calculations of system properties. In Section 2.3.1 the first 3D PIC simulations to observe the ZVP mechanism are presented. Further PIC simulations are presented in Section 2.4 focusing now on the hot electron bunches produced via the mechanism their properties, energy scalings and implications for SF-QED. Section ?? details the planned experiment to observe the ZVP mechanism at the GEMINI-PW laser facility including. Finally, concluding remarks are given in Section 2.5.

## 2.2 Introduction

Of primary interest in this thesis is the interaction of a relativistically intense short-pulse laser with a solid-density plasma target with a sharp density gradient. Now is presented one model for the interaction: the ZVP mechanism as proposed by *Baeva et al* [118] and later developed by *Savin et al* [117, 119]. Alongside the theories of the Relativistic Electron Spring [120] and Coherent Synchrotron Emission [121], ZVP is a post-ponderomotive model of attosecond absorption and reflection. The model considers a quasi-static surface equilibrium state analogously to ion acceleration in the hole boring [122] and light sail regimes [123].

An explanation for the absorption of laser energy into dense plasmas was first suggested by Wilks and Kruer [124]. A ponderomotive mechanism where plasma electrons are heated directly by the laser pulse via the  $\mathbf{J} \times \mathbf{B}$  force. This thesis is interested in the so-called ‘post-ponderomotive’ regime where the frequency of relativistic plasma oscillations ( $\omega_p \sim \sqrt{S}$ ) are greater than the  $\mathbf{J} \times \mathbf{B}$  induced plasma electron oscillations at  $2\omega_L$ . The plasma electrons’ response is then fast enough to compensate for the ponderomotive pressure of the laser pulse with the formation of electrostatic fields between electrons and ions and so respond adiabatically to the applied  $\mathbf{J} \times \mathbf{B}$  force. Hence, plasma electrons cannot be heated directly by the laser pulse. Interestingly, this condition suggests a criterion for the ZVP regime,  $S > 4$ , slightly more constraining than  $S > 1$  as is typically stated for the ZVP regime [119]. The bulk plasma must have  $S > 1$  to prevent relativistic transparency and so

ensure a laser-surface interaction. Then the ponderomotive pressure of the laser will typically compress the front surface to densities such that the overdensity condition is satisfied, provided the target is of sufficient thickness. Note that neglecting the pre-adiabatic formation phase requires a sufficiently steep density gradient around the relativistic critical density surface (where  $S = 1$ ) to shift the main interaction to a region where this condition on the overdensity is satisfied. Pre-plasma formation and scale length will be discussed in great detail in the following chapters. For now, assume the technology exists to control this phenomenon.

Provided all conditions are met, the ponderomotive pressure of the laser pulse compresses electrons at the front surface of the plasma and so shifts the laser-plasma surface interaction to plasma densities well beyond the relativistic critical density, leaving in its wake a positive space charge of ions. This electron-ion charge separation leads to the formation of a *pseudo-capacitor* electrostatic field. Having entered a regime of adiabaticity, the plasma skin layer is confined within a potential well consisting of the ponderomotive pressure of the laser pulse and the Coulomb potential of the pseudocapacitor field. Thus is formed a high-density and longitudinally thin electron bunch (sometimes referred to as an electron sheath in the literature [120]) at the plasma surface.

To understand this system, consider now a relativistic linearly polarised laser pulse obliquely incident, at an angle of incidence  $\theta$ , on a semi-infinite plasma, existing for  $x \geq 0$  as in Figure 2.1.

The Hamiltonian of a single electron confined within the potential well [80] is

$$\mathcal{H} = c\sqrt{m_e^2c^2 + |\mathbf{p}|^2} - e\Phi. \quad (2.1)$$

Here, the second term of Equation 2.1 describes the contribution to the electron's energy from the electrostatic potential,  $\Phi$ , of the pseudo-capacitor. The first term is the electron energy,  $U$ , extracted from the invariant of the relativistic 4-momentum of the electron,  $\mathbf{P}^\mu = (U/c, \mathbf{p})$ ,

$$\mathbf{P}_\mu \mathbf{P}^\mu = \frac{U^2}{c^2} - |\mathbf{p}|^2 = m_e^2c^2. \quad (2.2)$$

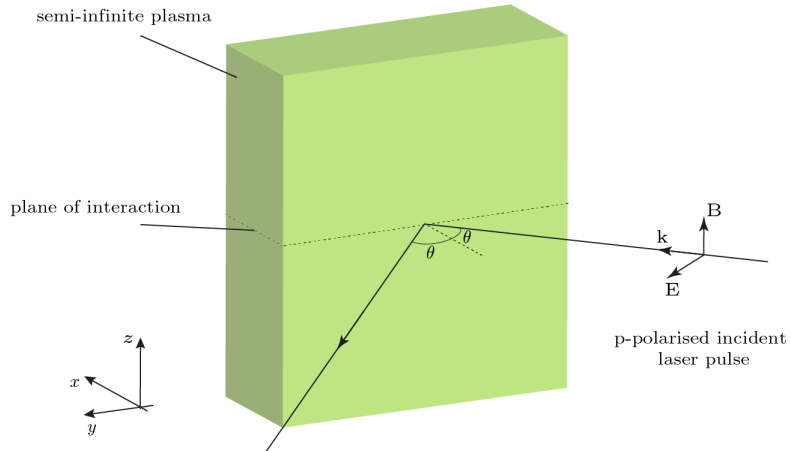


**Figure 2.1:** Diagram of a p-polarised laser pulse incident at angle  $\theta$  specularly reflected from a solid density plasma. By considering the Lorentz force equation, it is clear that all forces and therefore all plasma particle dynamics are confined to a plane.

Decomposing the electron's 3-momentum into orthogonal components:  $p_{\text{prop}}$ , along the laser propagation direction,  $p_{\text{pol}}$ , along the polarisation axis of the laser pulse and  $p_{\perp}$ , perpendicular to both, there are two simplifications to be made. Firstly, by canonical conservation of transverse momentum,  $p_{\text{pol}} = eA$ , where  $A$  is the laser vector potential amplitude. Secondly, in the case of a p-polarised laser pulse (the known optimum for ZVP electron bunch generation [117] and HHG [125]), with reference to Figure 2.1 and the Lorentz force law, the forces at play confine the electron trajectory to the  $p_{\text{prop}}-p_{\text{pol}}$  plane and the essential interaction geometry is two-dimensional. This is provided one considers length scales smaller than the focal spot of the laser pulse on the target, such that variation of the ponderomotive pressure with the third dimension can be neglected.

Explicitly, the Hamiltonian can be written as

$$\mathcal{H} = c\sqrt{m_e^2c^2 + p_{\text{prop}}^2 + e^2A^2} - e\Phi. \quad (2.3)$$

Equation 2.3 describes a potential well that constrains the electrons, on one side longitudinal space charge- $e\Phi$  term prevents further propagation into the target while on the other term associated with the vector potential of the laser pulse,  $e^2A^2$ . It is clear that should the vector potential pass through zero<sup>1</sup>, one of the

---

<sup>1</sup>Note that in writing  $p_{\text{pol}} = eA$  one has determined the gauge in which the zero becomes a defined quantity

potential well walls is totally suppressed, enabling electrons in the skin layer to escape the plasma, breaking adiabaticity. The necessity of vector potential zeros for this violent reconstruction of the plasma surface led Baeva *et al* [118] to coin the term ‘Zero Vector Potential’ mechanism to describe this process. Indeed, while elementary electromagnetism tells us a laser pulse will exponentially decay within a skin layer of a plasma without passing through zero, Baeva *et al* [118] demonstrated in PIC simulations that in this non-linear regime, zeros do exist and do propagate through the skin layer. The explanation relies on a Doppler shift in the laser field due to the relativistic motion of the ablating plasma surface, and a mathematical formalism of this process proceeds as follows.

As the ZVP mechanism is a relativistic phenomenon, it is absolutely essential to perform a relativistic analysis. Since all accelerated electrons travel at approximately speed  $c$ , surface electrons undergo similar trajectories. Acting collectively they oscillate in the laser pulse field. Consider first a transformation to the frame of reference where the laser pulse is normally incident to the plasma surface, this frame travels at velocity  $\mathbf{v} = (c \sin \theta) \hat{\mathbf{y}}$  with electrons streaming at  $-\mathbf{v}$ . Using Equation 2.2,  $U = \gamma m_e c^2$  and integrating Equation 1.50 in the boosted frame noting  $p_T(t = 0) = \gamma_{\mathbf{v}} m_e v = m_e c \sin \theta \cos \theta$ ,

$$\gamma^2 = 1 + (a_0 + \sin \theta \cos \theta)^2 + \left( \frac{p_{\text{prop}}}{m_e c} \right)^2, \quad (2.4)$$

where all parameters are in the boosted frame. Using  $\mathbf{p} = \gamma m_e \mathbf{v}$ , the longitudinal velocity is

$$v_{\text{prop}} = \frac{\tilde{p}_{\text{prop}} c}{\sqrt{1 + (a_0 + \sin \theta \cos \theta)^2 + \tilde{p}_{\text{prop}}^2}}, \quad (2.5)$$

where  $\tilde{p}_{\text{prop}} = p_{\text{prop}}/m_e c$ . Thus, should the transverse vector potential pass through  $-\sin \theta \cos \theta$ , zero for normal incidence, the surface can propagate towards the laser pulse at very close to speed  $c$ . Transforming back to the laboratory frame, at the peak of ablation ( $\mathbf{u} \approx -c \hat{\mathbf{x}}$ ) and using the equations for relativistic velocity addition,

$$\mathbf{u}'_{\parallel} = \frac{\mathbf{u} - \mathbf{v}}{1 - \mathbf{u} \cdot \mathbf{v}/c^2}, \quad (2.6)$$

$$\mathbf{u}'_{\perp} = \frac{\mathbf{u}_{\perp}}{\gamma_v(1 - \mathbf{u} \cdot \mathbf{v}/c^2)}, \quad (2.7)$$

where  $\gamma_v = 1/\sqrt{1 - |\mathbf{v}|^2/c^2}$  [74], one finds that this peak ablation at speed  $\approx c$  occurs now in the specular reflection direction. Simultaneity is broken and ripples co-move along the surface with the incident laser pulse wavefronts.

Transform now to the rest frame of the ablating front. Beyond the relativistic critical density surface, the vector potential of the laser pulse decays evanescently. At the spatial centre of the laser pulse, it can be described simply by

$$\mathbf{A}'_{\text{L}}(t', r') = A'_0 \cos(\omega'_{\text{L}} t') \exp(-r'/\delta') \hat{\mathbf{r}}'_{\text{pol}} = A'_0 \hat{\mathbf{r}}'_{\text{pol}}, \quad (2.8)$$

where the primed symbols indicate that these quantities are measured in the rest frame of the expanding front.  $A'_0$  is the vector potential amplitude and  $\omega'_{\text{L}}$  is the frequency of the laser pulse,  $r'$  is the propagation distance of the laser into the plasma,  $\delta'$  is the skin depth and  $\hat{\mathbf{r}}'_{\text{pol}}$  a unit vector defining the polarisation direction of the laser pulse. Un-primed coordinates will indicate the lab frame measurements.

While previous demonstrations of the existence of vector potential zeros assumed that the ablation occurs normally to the plasma surface, it is necessary to confirm that zeros are still predicted for specular ablation. Consider a p-polarised laser pulse confined to the  $x$ - $y$  plane incident with an angle of incidence  $\theta$  on an ablating overdense plasma expanding with velocity  $-v_f \hat{\mathbf{x}}$  in the lab frame, as in Figure 2.2.

The direction of polarisation is

$$\hat{\mathbf{r}}_{\text{pol}} = \hat{\mathbf{x}} \sin 2\theta - \hat{\mathbf{y}} \cos 2\theta \quad (2.9)$$

and the velocity of the rest frame of the ablating front relative to the lab frame is  $-v_f \hat{\mathbf{x}}$ .

Applying the Lorentz transformation to the electromagnetic 4-potential,  $\mathbf{A}^{\mu}$ , where  $\Lambda_{\mu}^{\nu}$  is given by Equation 1.30, immediately from the  $y$ -coordinate transformation,

$$A'_{\text{L}} \cos 2\theta' = A_{\text{L}} \cos 2\theta. \quad (2.10)$$

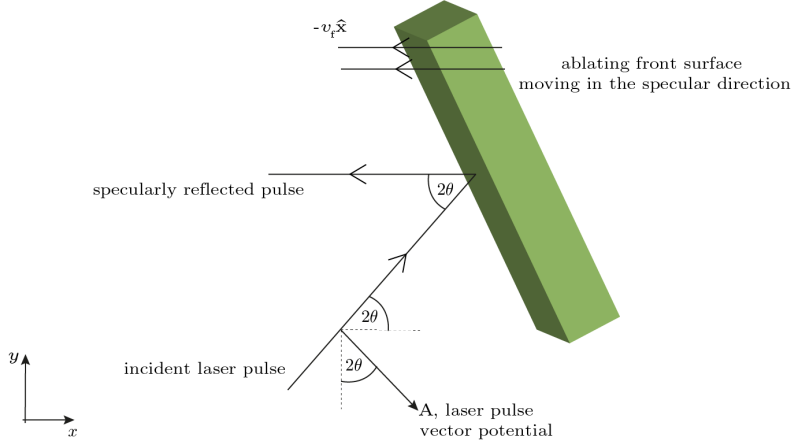


**Figure 2.2:** Diagram of a  $p$ -polarised laser pulse incident on an ablating overdense plasma. The laser is incident obliquely at an angle of  $\theta$  and is reflected specularly. The plasma ablates specularly also. Note that this process occurs on sub-laser pulse cycle timescales and it is therefore only the electrons that are ablating in this process. The interaction geometry is confined to a 2D plane.

Applying the headlight effect for a source moving at an angle  $2\theta$  to the boosted frame (a full derivation is given in Appendix A.2),

$$\cos(2\theta') = \frac{\cos(2\theta) - \beta}{1 - \beta \cos(2\theta)} \quad (2.11)$$

and rearranging Equation 2.10, the vector potential in the lab frame is

$$A_L = \frac{1 - \beta \sec(2\theta)}{1 - \beta \cos(2\theta)} A'_0 \cos(\omega'_L t') \exp(-r'/\delta'). \quad (2.12)$$

Writing the boosted frame space-time coordinates in terms of the lab frame coordinates,

$$ct' = \gamma(ct - \beta x), \quad (2.13)$$

$$x' = \gamma(x - \beta ct), \quad (2.14)$$

yields

$$A_L = A_0 \cos(\omega_L t - kx) \exp\left(-\frac{\sqrt{(x - \beta ct)^2 + (y/\gamma)^2}}{\delta}\right), \quad (2.15)$$

where

$$A_0 = \frac{1 - \beta \sec(2\theta)}{1 - \beta \cos(2\theta)} A'_0, \quad (2.16)$$

$$\omega_L = \gamma \omega'_L, \quad (2.17)$$

$$k = \frac{\beta \gamma \omega'_L}{c}, \quad (2.18)$$

$$\delta = \frac{\delta'}{\gamma}. \quad (2.19)$$

The oscillatory term in Equation 2.15 demonstrates the propagation of vector potential zeros within the plasma target. From the structure of this term, it would appear that these zeros are expelled from the plasma along the specular direction at a speed

$$v_\phi = \frac{\omega_L}{k} = \frac{c}{\beta} = -\frac{c^2}{v_f}. \quad (2.20)$$

While in their original ZVP paper, Baeva laid some doubt on their version of this calculation, instead suggesting similarity theory predicts zeroes propagate at speed  $c$  [118], the theory of High Harmonic Generation rejects this alternative. It is well known that the emission of reflected radiation occurs primarily at the point where the transverse vector potential passes through zero [116] but equally that the width of the radiated pulse depends on the advance time emission point [126]. If the zeroes moved at speed  $c$ , then the observed emitted pulse would be infinitely thin, producing radiation with perfect coherence in all cases. This is unphysical and simulations have suggested finite advanced time bunch widths decreasing rapidly with increasing laser intensity [126]. This is precisely what is predicted by Equation 2.20. As the laser intensity increases,  $v_f$  naturally increases. Thus, the zeroes propagate closer to the speed of light and reduce the advanced time bunch width.

To summarise, for a sufficiently intense laser pulse, electrons at the surface of an irradiated solid target are accelerated by the laser to relativistic velocities at a fraction of a laser pulse cycle and therefore electrons both follow similar trajectories and respond adiabatically to the  $\mathbf{J} \times \mathbf{B}$  force of the laser pulse. They form into a high charge density spatially thin coherent electron bunch on the front surface of the plasma but are displaced inwards from the approximately immobile ions via the ponderomotive pressure of the laser. This charge separation generates a longitudinal electrostatic pseudocapacitor field that confines electrons to a potential well on the front surface of the plasma, preventing further propagation of the electron bunch into the plasma bulk. When the zero of the vector potential passes through the electron bunch, the ponderomotive pressure instantaneously

vanishes and electrons are ejected specularly from the target, co-propagating with the zeroes of the vector potential.

In the work by Cousens *et al* on electron trajectories in this regime, it is noted that a Coherent Synchrotron Emission (CSE) radiation burst occurs when the transverse momentum goes to zero [cousens2020], corresponding to the passage of the zero of the transverse vector potential. CSE and ZVP are therefore intrinsically linked, however, while CSE focuses on reflection and the HHG spectrum, ZVP is concerned with laser pulse energy absorption.

After expulsion from the plasma, the pseudocapacitor is discharged as the electron bunch accelerates across it. Upon encountering the subsequent laser pulse peak amplitude, the bunch is then rotated back towards the plasma and launched into the bulk at high energy along the laser propagation axis (by conservation of transverse momentum in the plasma bulk), as it does so emitting coherent synchrotron radiation in transmission.

### 2.2.1 ZVP electron bunch energies

In [118], Baeva *et al* propose energy scalings in one-dimension (1D) for an electron bunch produced in the ZVP regime as a function of the incident laser pulse intensity and plasma density. This was extended to three-dimensions (3D) by Savin *et al* [117]. What follows is that discussion with closer consideration of both the constants of proportionality and their consequences. Note that throughout the electron bunch is treated as infinitesimally thin, as proved to be a reasonable assumption in previous work on ZVP [117, 125, 127]. Sub-bunch dynamics have been explored in more detail by Gonoskov *et al* [128].

The expressions for energies in equations 2.26 and 2.29 require the electron bunch to fully discharge the pseudo-capacitor before interaction with the subsequent laser pulse peak. Since the electron bunch travels at speed  $\approx c$ , the peak displacement (and thus the pseudo-capacitor width) must satisfy

$$\Delta x \leq \frac{\lambda}{8}. \quad (2.21)$$

Using Equation 2.24, it is clear Equation 2.21 is satisfied for  $S \geq 1.3$  at normal incidence.

Consider again the semi-infinite block of plasma presented in Figure 1.2, normally irradiated by a laser pulse with wavelength  $\lambda_L$  and peak electric field,  $E_L$ . It is now the ponderomotive pressure of the laser that displaces the electron fluid in this picture. The electron surface moves inwards until the pressure exerted by the peak instantaneous ponderomotive pressure of the laser pulse cycle,

$$\mathbf{P}_L = \epsilon_0 E_L^2 \hat{\mathbf{x}} = \epsilon_0 \left( \frac{a_0 \omega_L m_e c}{e} \right)^2 \hat{\mathbf{x}} \quad (2.22)$$

is equal and opposite to the pressure exerted by the pseudo-capacitor field,

$$\mathbf{P}_C = \frac{QE_C}{\sigma} \hat{\mathbf{x}} = -\frac{(en_e \Delta x)^2}{\epsilon_0} \hat{\mathbf{x}} \quad (2.23)$$

from equations 1.16 and 1.17. Equating the magnitudes of  $\mathbf{P}_L$  and  $\mathbf{P}_C$ , the maximum displacement inwards of electrons is

$$\Delta x \hat{\mathbf{x}} = \frac{c}{\omega_L} \frac{a_0}{\bar{n}_e} \hat{\mathbf{x}} = \frac{1}{kS} \hat{\mathbf{x}}, \quad (2.24)$$

where  $k$  is the wavevector of the laser pulse. Correspondingly,

$$E_C = \frac{en_e}{\epsilon_0} \Delta x = \frac{\omega_L c m_e a_0}{e} = E_L. \quad (2.25)$$

Applying the results of equations 2.24 and 2.25, when the ponderomotive pressure vanishes and the electron bunch is launched across the pseudo-capacitor, the relativistic kinetic energy gained by a single electron is

$$T = \int \mathbf{F} \cdot d\mathbf{s} = \int_{\Delta x}^0 -eE_C dx = \int_{\Delta x}^0 -\frac{en_e x}{\epsilon_0} dx = \frac{1}{2} m_e c^2 \frac{a_0^2}{\bar{n}_e} \quad (2.26)$$

or an electron gamma factor,

$$\gamma = \frac{1}{\sqrt{1 - \beta^2}} = 1 + \frac{a_0^2}{2\bar{n}_e}. \quad (2.27)$$

Assuming all displaced electrons are captured by the potential well and launched as a coherent bunch, the total number of electrons in the bunch is

$$N_e = n_e \sigma \Delta x = \frac{\sigma a_0 n_c}{k} = \sigma \epsilon_0 E_L \quad (2.28)$$

and hence, the total kinetic energy of the electron bunch is

$$U_{\text{ZVP}} = N_e T = \frac{\sigma n_c}{k} \times \frac{1}{2} m_e c^2 \frac{a_0^3}{\bar{n}_e}. \quad (2.29)$$

It is now interesting to compare Equation 2.29 to the laser energy deposited upon the plasma surface and therefore consider what fraction of the laser energy can be absorbed via the ZVP mechanism. Using  $E_C = E_L$ , Equation 2.29 can be rewritten as

$$U_{\text{ZVP}} = \frac{1}{2\omega_L S} \sigma c \epsilon_0 E_L^2. \quad (2.30)$$

For the case of normal incidence, bunches are produced at a frequency of  $2\omega_L$ , naturally following the frequency of the  $\mathbf{J} \times \mathbf{B}$  force. Assuming a sinusoidal plane wave incident with surface area  $\sigma$ , the energy available during the pushing phase (a quarter-cycle) is

$$U_{L,1/4} = \sigma \frac{T}{4} \langle I_L \rangle = \frac{2\pi}{8\omega_L} \sigma c \epsilon_0 E_L^2. \quad (2.31)$$

Hence,

$$\eta_{\text{ZVP}} = \frac{U_{\text{ZVP}}}{U_{L,1/4}} = \frac{2}{\pi S}. \quad (2.32)$$

Interestingly, this analytical result predicts the trend observed by A. Savin [119] in PIC simulations both in magnitude and in scaling. Indeed, A. Savin demonstrated in numerical simulation

$$\eta_{\text{ZVP}} \sim S^{-1.000(3)}, \quad (2.33)$$

however, this result led A. Savin to conclude that increasing  $S$  reduces absorption, increasing the energy in the reflected HHG beam thus increasing high harmonic efficiency, seemingly in tension with the results of other works [120, 126]. The resolution arises from awareness of two distinct conversion efficiencies that describe the reflected harmonic spectrum: the total conversion efficiency into the full reflected beam and the conversion efficiency for individual harmonics. While the overall conversion into the reflected beam decreases for decreasing  $S$ , the slope of the harmonic spectrum becomes shallower and HHG efficiency increases. Indeed, high

harmonic efficiency necessitates high reflection inefficiencies due to the production of ZVP electron bunches as higher energy bunches produce more coherent reflected radiation [126]. Harmonic efficiencies will be discussed in more detail in the following Chapters, however, at currently accessible laser intensities, it would appear that X-ray harmonics are produced with greater efficiency for high  $S$  [129], a regime generally neglected in parameter scans given the computational and experimental challenges of accessing it.

Unfortunately, it is not possible to link the energy scaling derived in this Section to CSE since the harmonic emission occurs before the ZVP acceleration phase. In Dromey *et al*, the CSE regime was demonstrated for the first time in transmission through thin foils, however, laser pulses are now of sufficient intensity to access CSE in reflection from solid targets. This has been identified as a more efficient approach if it can be reached due to the production of higher density and shorter duration electron bunches and therefore brighter and more coherent CSE [130].

### 2.2.2 ZVP bunches oblique incidence scaling

This section is inspired by ideas from the work of Gonoskov *et al* [120] and Vincenti *et al* [122] to extend the theory of the ZVP mechanism for energy absorption to the more practical<sup>2</sup> case of oblique incidence.

Provided the plasma-vacuum boundary is sufficiently steep, the plasma electrons will respond adiabatically to the laser pulse and arrange themselves to form a pseudocapacitor longitudinal electric field  $E_C$  at the plasma surface. At all points in this adiabatic ‘pushing’ phase, the surface electrons will be in a quasi-static equilibrium *i.e.* there will be a balance between the electromagnetic forces on them. Consider again the laser pulse incident on a solid density plasma existing for  $x > 0$  at angle  $\theta$ . Transforming to the frame of reference in which the laser is normally incident (quantities in this frame are indicated by the primed symbol), the electron and ion bulk plasma species stream at velocity  $\mathbf{v}_d = -c \sin \theta \hat{\mathbf{y}}$ . Applying the Lorentz force law along the longitudinal direction ( $\hat{\mathbf{x}}$ ), for a displacement of the electron fluid

---

<sup>2</sup>Not only is this more feasible in experiment but has been shown to optimise HHG [120].

$x'_e$  (one assumes that the expression for a single electron at the surface describes the surface since all electrons follow similar trajectories), travelling at speed  $\mathbf{v}'$ ,

$$-e(\mathbf{v}'(x'_e) \times (\mathbf{B}'_L(x'_e) + \mathbf{B}'_i(x'_e)) \cdot \hat{\mathbf{x}} + E'_C(x'_e)) = 0, \quad (2.34)$$

where the laser magnetic field,

$$B'_L = \frac{m_e \omega'_L a_0 \sin(\omega'_L t' - k' x'_e)}{e} \hat{\mathbf{z}} \quad (2.35)$$

and  $B_i$  is the magnetic field generated by the uncompensated ion current,  $\mathbf{J}_i = Z n'_i(x'_e) \mathbf{v}_d$ , where the electron fluid has been displaced. As before, from Equation 1.17,

$$E'_C = \frac{en'_e x'_e}{\epsilon_0}. \quad (2.36)$$

Applying Maxwell-Ampère's Law, Equation 1.1c, and noting that by symmetry there can be no variation in the magnetic field with  $y'$  or  $z'$ , it becomes clear that

$$-\frac{d(\mathbf{B}'_i)_{z'}}{dx'} = \mu_0 (\mathbf{J}_i)_{y'}. \quad (2.37)$$

Integrating Equation 2.37 from  $-\infty$  to  $x'_e$ , noting that  $\mathbf{B}_i = 0$  at infinity and assuming a constant density profile  $n'_i$  for  $x > 0$  with  $Z n_i = n_e$ ,

$$\mathbf{B}'_i(x'_e) = \mu_0 en'_e x'_e c \sin(\theta) \hat{\mathbf{z}}. \quad (2.38)$$

Using equations 2.35, 2.36 and 2.38 and making the reasonable approximation that the relativistic electrons on the surface move at speed  $v'_y \approx \pm c$  at peak displacement ( $x'_e = x'_p$ ), 2.34 can be written as

$$-e \left( \pm c \left( \pm \frac{m_e \omega'_L a_0}{e} + \mu_0 en'_e x'_p c \sin \theta \right) + \frac{en'_e x'_p}{\epsilon_0} \right) = 0. \quad (2.39)$$

For the laser to be in the pushing phase, the first term must be negative, corresponding to  $\mathbf{v}'$  and  $\mathbf{B}'_L$  having the opposite sign, hence,

$$c \left( -\frac{m_e \omega'_L a_0}{e} \pm \mu_0 en'_e x'_p c \sin \theta \right) + \frac{en'_e x'_p}{\epsilon_0} = 0, \quad (2.40)$$

where here the  $\pm$  tracks the sign of  $\mathbf{v}'$ . After some manipulation, one arrives at

$$x'_p = \frac{1}{k' S' (1 \pm \sin \theta)}. \quad (2.41)$$

Transforming back to the lab frame,

$$x_p = \frac{\cos^2 \theta}{kS(1 \pm \sin \theta)}. \quad (2.42)$$

Convincingly, this reduces to Equation 2.24 for  $\theta = 0$  and predicts the suppression and enhancement of the two surface oscillations per laser pulse cycle. Explicitly, for a laser pulse propagating at  $y = x \tan \theta$ , the peak displacement of the electron surface is enhanced for  $\mathbf{B}_L$  in the  $+\hat{\mathbf{z}}$ -direction and suppressed for  $\mathbf{B}_L$  in the  $-\hat{\mathbf{z}}$ -direction.

Again, integrating to find the work done as the electron bunch accelerates across the pseudocapacitor,

$$T(\theta) = \int \mathbf{F} \cdot d\mathbf{s} = \frac{1}{2} m_e c^2 \frac{a_0^2}{\bar{n}_e} \frac{\cos^4 \theta}{(1 \pm \sin \theta)^2}. \quad (2.43)$$

While it was to be expected that a component of the electric field acting into or out of the plasma would change the magnitude of the displacement, this result suggests that increasing the angle of incidence can increase the electron energy gain in the enhanced cycle more than the decrease in the suppressed cycle. Note that this is to be expected as it is known that HHG efficiency is improved for non-zero angle of incidence [120, 126]. It would be interesting to explore whether the presence of an external magnetic field could be applied to mimic the effect of oblique incidence by replacing the magnetic field due to the uncompensated ion current.

While this model would suggest an optimal angle for electron energy and therefore of HHG of  $\pi/2$ , if  $\theta > \pi/4$ , then, if the relativistic electron bunch is travelling at  $c$  along the specular reflection direction, the subsequent laser peak amplitude will never ‘catch up’ with the electron bunch, and electrons can escape, generating high charge electron bunches in reflection as observed in experiment by Lin *et al* [113], but reducing the efficiency of HHG.

Finally, the total bunch energy as a function of  $\theta$ ,

$$U_{ZVP}(\theta) = \frac{\sigma n_c}{k} \times \frac{1}{2} m_e c^2 \frac{a_0^3}{\bar{n}_e} \frac{\cos^6 \theta}{(1 \pm \sin \theta)^3}. \quad (2.44)$$

As anticipated, oblique incidence can increase laser absorption efficiency for higher  $S$  plasmas which are currently more easily accessed compared to the more optimal low  $S$  plasmas.

### 2.2.3 Defining characteristics of the ZVP mechanism

In her original paper on the ZVP mechanism, T. Baeva *et al* [118] outlined 6 defining characteristics of the ZVP mechanism, namely,

1. The existence of vector potential zeros moving through the skin layer in the laboratory frame;
2. The existence of zeroes in the incident laser pulse vector potential required for the formation of fast electron bunches;
3. The generation of fast electron bunches with ultra-short temporal duration;
4. That such fast electron bunches follow the energy scalings of equations 2.26 and total energy 2.29;
5. Injection of the fast electron bunches is along the propagation axis of the laser pulse;
6. There must be an intrinsic link between the fast electron bunches and coherent HHG;

with the moving zeros within the skin layer being the key delineator between this post-ponderomotive regime of laser pulse energy absorption and all other proposed mechanisms. While such observational requirements are far beyond the reaches of current experimental know-how, numerical simulations in both 1- [118] and 2-dimensions [117] have confirmed the above points. Now is presented the first 3D simulations attempting to demonstrate these criteria.

## 2.3 Numerical simulations of the ZVP mechanism

This thesis relies on the analysis of 1,2 and 3D PIC simulations, primarily using the massively parallel and open-source simulation code Smilei [75]. Simulation parameters are provided throughout.

### 2.3.1 The ZVP mechanism in 3D3V

3D simulation results are presented in Figure 2.3 alongside comparison to an equivalent 2D simulation. Simulation parameters are given in Table 2.1, such parameters are compatible with the 10 PW ELI-NP state-of-the-art short pulse laser facility [131] incident on foam targets. Figure 2.3c) clearly demonstrates the existence of high energy density electron bunches propagating through the plasma bulk in the direction of the laser pulse. Note that this ZVP criterion is a direct consequence of conservation of transverse momentum inside the plasma bulk where the laser fields cannot propagate. Figure 2.3b) shows these bunches escape to the rear of the bulk but lose energy as they do so. Looking now at Figure 2.3e) and the internal structure of the plasma bulk. These bunches drive two-stream and filamentation instabilities [132]. The bulk propagating electron bunches are accompanied by higher density electron bunches to either side of the plasma block with the side of emission alternating every half laser pulse cycle.

#### Considerations and convergence of 3D simulations

The plasma specifications were chosen to minimise computational load while ensuring numerical convergence, requiring over 100 billion macroparticles. The electron temperature is raised significantly higher than that which would be expected in such a laser-plasma system so as to resolve the Debye length. Anticipated plasma temperatures are calculated using 1D HYADES simulations in the following Chapter. While this temperature is unphysical and will lead to some small plasma expansion over the course of the simulation (negligible on these timescales), the temperature remains small compared to that imparted to the electron bunches by the laser pulse. The striking similarity between the 2 and 3D simulation results is a natural consequence of the 2D nature of the interaction geometry. It is, however, still reassuring to show that previous work withstands the test of reality's geometry and the simple elegance of the ZVP mechanism is not lost in the chaos.

For the 3D simulations only, particles were initialised randomly not regularly to avoid numerical error. Regularly initialised plasma blocks in 3D simulations

### 2.3. Numerical simulations of the ZVP mechanism

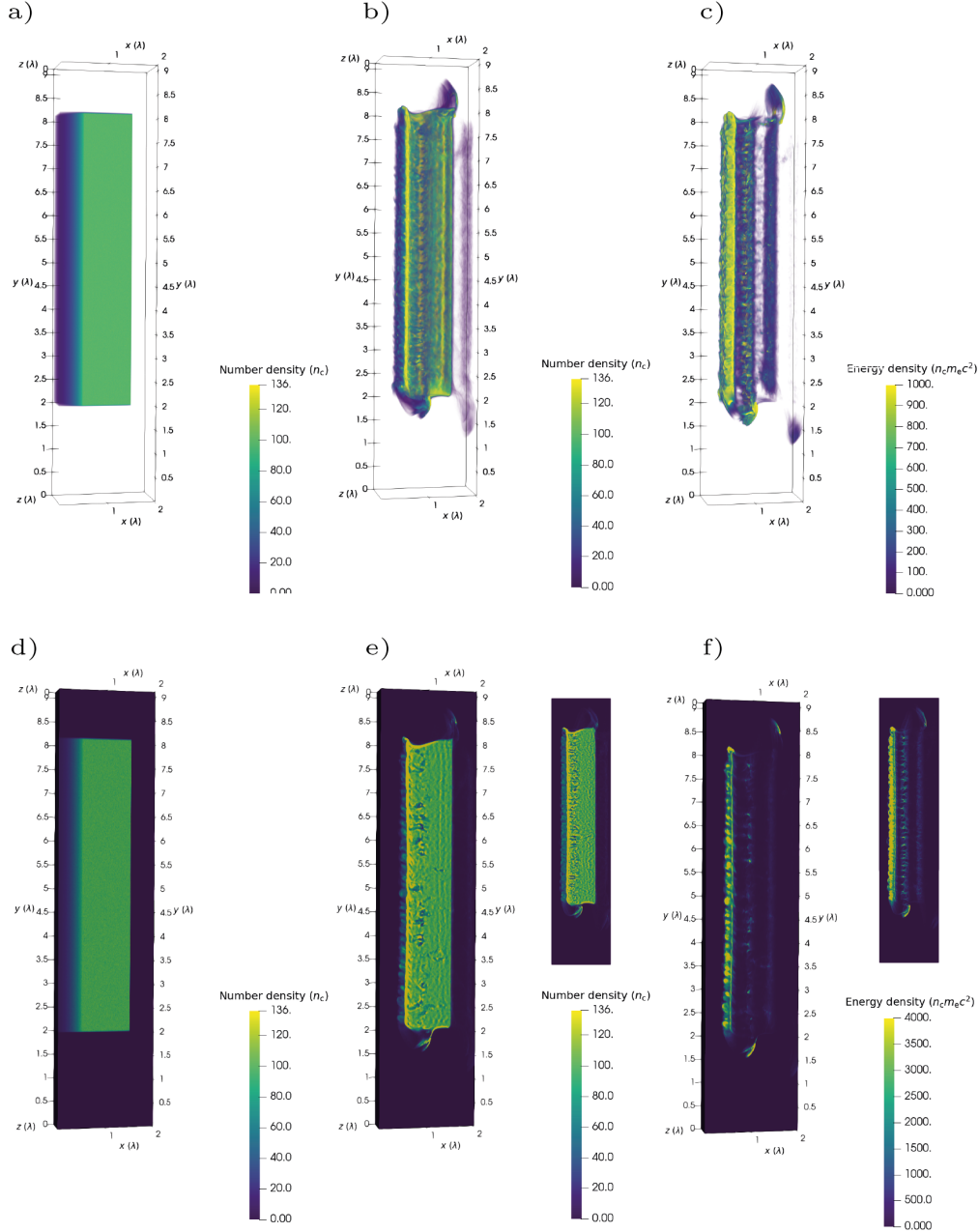


**Figure 2.3:** Simulation results from a 3D PIC simulation of the ZVP mechanism. a) The initialised electron number density. b) The electron number density several cycles later, the plasma bulk is intact, however, there is evidence of instabilities and electron bunches propagating through and around the plasma. c) The electron kinetic energy density at the same timestep. Note that the scale has been clipped to enable observation of both electron bunches propagating through and around the plasma bulk. Significantly higher energy density, corresponding to a higher charge density and attosecond duration is observed for the electron bunches propagating around the bulk. d-f) Plots clipped through  $z = \lambda_L/2$  for a-c) respectively to access the internal structure of the plasma bulk. The accompanying plots for figures e) and f) are equivalent 2D PIC simulations demonstrating excellent agreement.

Laser (3D, normal incidence)		
Parameters	Real	Smilei
Wavelength, $\lambda$ (nm)	1060	$2\pi$
Angular frequency, $\omega_L$ (fs $^{-1}$ )	1.8	1
Beam waist, $w_L$ (nm)	$6\lambda$	$12\pi$
Focal point, $(f_x, f_y, f_z)$ (nm)	$(0.5\lambda, 5\lambda, 0.5\lambda)$	$(\pi, 10\pi, \pi)$
Spatial envelope, $E_i$ , $i = y, z$	$E_i \sim e^{-(i-i_f)^2/w_L^2}$	
Temporal envelope, $E_t$	$E_t \sim e^{-(t-4\lambda/c)^2/((4\lambda/3c)^2 \ln 2)}$	
Simulation box		
Size, $x \times y \times z$ (nm)	$2\lambda \times 9\lambda \times \lambda$	$4\pi \times 18\pi \times 2\pi$
Sim length (fs)	35.22	$20\pi$
Spatial resolution, $\Delta x$ (nm)	$\lambda/128 = 8.28$	0.0491
Temporal resolution, $\Delta t$ (as)	$\Delta x/11c = 2.51$	0.00446
Collisionless, pre-ionised randomly-initialised aluminium plasma		
Electron $x$ profile, $n(x)$	$\begin{cases} n_e & \text{for } 2\lambda \leq x \leq 3\lambda, \\ n_e e^{(x-2\lambda)/0.2\lambda} & \text{for } x \leq 2\lambda. \end{cases}$	
Electron $y$ profile, $n(y)$	$\begin{cases} 1 & \text{for } 2\lambda \leq y \leq 8\lambda, \\ 0 & \text{otherwise.} \end{cases}$	
Electron $z$ profile, $n(z)$	$\begin{cases} 1 & \text{for } 0.125\lambda \leq z \leq 0.875\lambda, \\ 0 & \text{otherwise.} \end{cases}$	
Ion profile, $n_i(x, y, z)$	$n_i = n(x)n(y)n(z)/13$	
Macro-electrons per cell	729	
Macro-ions per cell	8	
Ion temperature, $T_i$ (keV)	0	0
Electron temperature, $T_e$ (keV)	10	0.02
Stability criteria		
$\lambda_D/\Delta x$	0.288	
$1/\Delta t \omega_p$	24.4	
$\Delta x/c\Delta t$	11	
Macro-particles in the Debye sphere	210	

**Table 2.1:** Simulation parameters in both real and normalised Smilei simulation units for the 3D3V simulations.

rapidly blow apart due to spurious large amplitude fields generated on the large plasma surfaces due to macroscopic electron-ion charge separation at initialisation. 2D simulations with randomly initialised particles tend to produce nano-structures reminiscent of the cosmic web. The absence of these structures in 3D is telling. Unsurprisingly this error can be reduced by increasing the plasma temperature.

The longitudinal thickness of the target does not impact the interaction and is chosen for computational efficiency, indeed it is standard to consider such targets of thickness  $\geq \lambda_L$  as bulk targets [71], however, for sufficiently long pulse durations, the effect of hole boring necessitates thicker targets to make this approximation as is necessary in the following Chapter.

The initial 3D simulation parameters were chosen to be consistent with previous work on the ZVP mechanism, however, such simulations are cumbersome. In order to query the defining characteristics outlined by Baeva, a lower-resolution simulation was performed with similar parameters to the initial simulation. Comparisons between the simulation outputs are made in Figure B.1 in Appendix B.1. Good convergence is qualitatively demonstrated by the presence of characteristic features of the ZVP mechanism. While the instabilities are similar in structure, the change in seeding changes their exact positions. As instabilities are not the focus of this thesis this variation is of no cause for concern.

## Confirmation of ZVP in 3D

Figure 2.4 tracks the transverse momentum distribution along the polarisation axis of the laser pulse of an electron bunch during its ablative journey, clearly demonstrating the existence of a singular zero of the vector potential propagating through the electron bunch and away from the plasma bulk. The zero propagates at a speed of  $\approx 1.4c$ , corresponding to a surface velocity of  $\approx 0.71c$ . In this simulation, the zero propagates through the bunch over a few nanometres and before crossing the pseudocapacitor. Note that consideration of the moving zeroes reframes the problem of the advanced time bunch width [126] (the determiner of attosecond

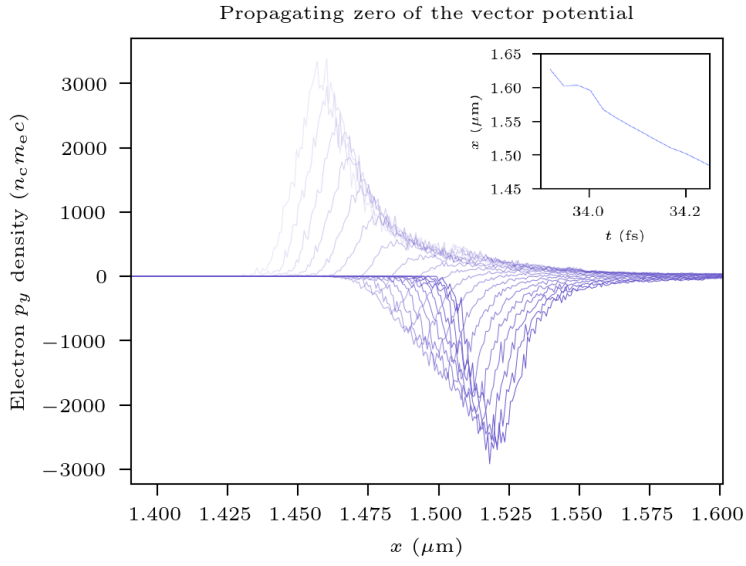


**Figure 2.4:** Propagation of a vector potential zero through the ablating ZVP electron bunch via the proxy of transverse momentum conservation. The zero of the vector potential exists where the transverse momentum is macroscopically zero. Each line represents a timestep with time increasing with decreasing colour. With increasing time the bunch and the zero move in the  $-\hat{x}$ -direction with the zero overtaking the electron bunch. The inset tracks the position of the zero of the vector potential with time.

CSE pulse duration). Gonoskov *et al* have determined a scaling for electron bunch width [120] thus the only unknown is the surface velocity.

Further simulation results are presented in Figure 2.5. In Figures 2.5a)-d), comparisons are made in the electron energy distributions for simulations with zeros present in the vector potential (linearly polarised) and without (circularly polarised). Clearly, zeroes are required for the formation of high energy, short duration attosecond bunches. From Figure 2.5a) it is clear that electron bunches are injected, propagating through the plasma bulk in the laser propagation direction. Figure 2.5c) demonstrates the quasi-monoenergeticity of the high-energy electron bunches as initially identified in 1D by Baeva. Although the shape in the phase space is more complex in 3D, the attosecond duration at a given energy is retained. Figures 2.5e) and f) describe the surface dynamics in the linearly polarised case. One can observe the high-density bunches on the front surface with the peak in energy density occurring after acceleration across the pseudocapacitor.

### 2.3. Numerical simulations of the ZVP mechanism

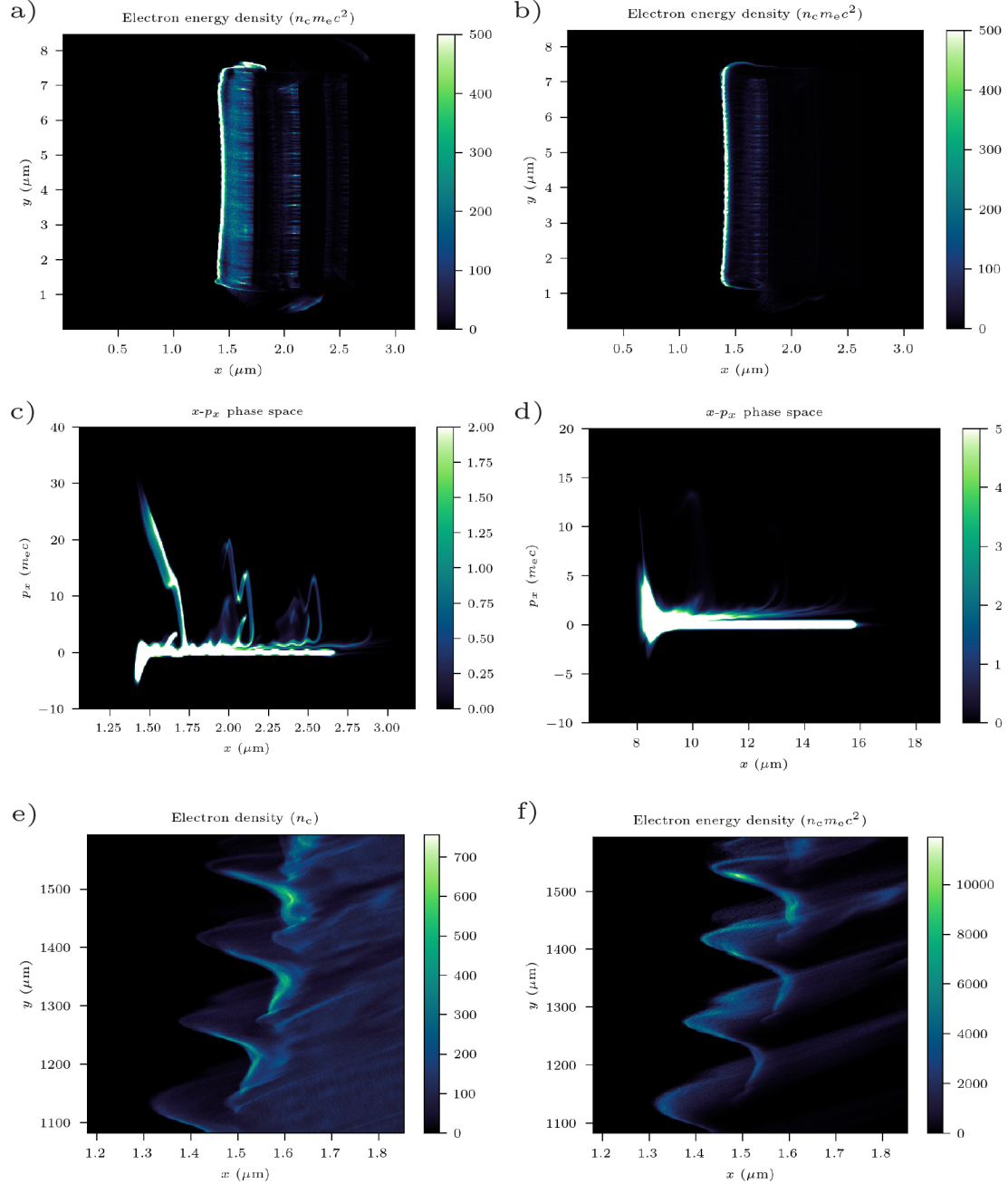


**Figure 2.5:** Electron dynamics in a 3D PIC simulation. a) and b) Electron energy density for linearly and circularly polarised laser pulses respectively. c) and d) Electron longitudinal momentum for linearly and circularly polarised laser pulses respectively. e) Electron density at the plasma surface streaked in time. f) Electron energy density at the plasma surface streaked in time.

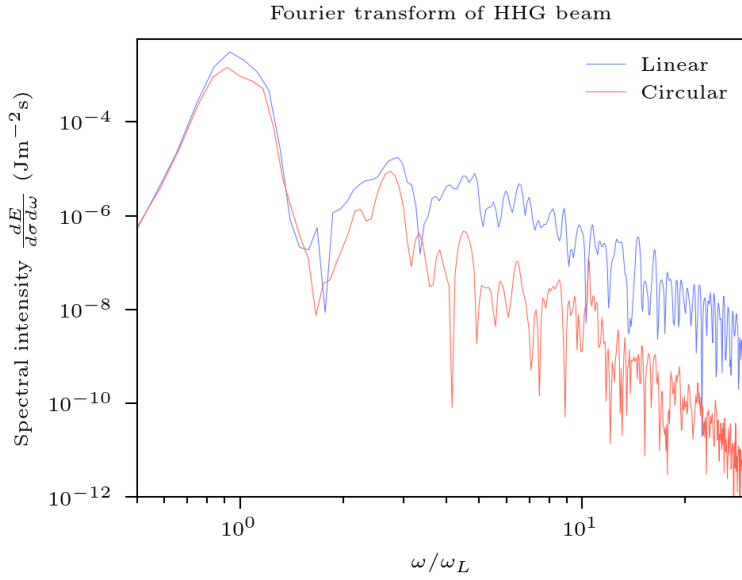


**Figure 2.6:** The Fourier transform of the reflected laser pulse in 3D PIC simulations both with and without zeroes in the vector potential.

Finally, Figure 2.6 compares the spectra of the reflected light in the presence and absence of zeros of the vector potential. Individual harmonics are not resolved due to blueshifts between successive pulse cycles from considerable hole boring, a phenomenon discussed in great detail in the following Chapter. The spectrum from the circularly polarised light is typically over two orders of magnitude below that of linearly polarised light. Thus, all defining characteristics of the ZVP mechanism have been identified in 3D simulations with the notable exception of the energy scalings. Next-generation supercomputers will be required to perform such parameter scans.

## 2.4 The ZVP electron bunch

Following the excellent agreement demonstrated between 2 and 3D PIC simulations, the remainder of this Chapter explores ZVP primarily in 2D. Previous work on the ZVP mechanism has highlighted the high energy and short duration of electron bunches, what follows is a full characterisation of their properties. A ZVP electron bunch is an electron bunch produced via the ZVP mechanism. Once produced and accelerated across the pseudocapacitor field, it is launched back in the laser propagation direction. While the bunch has no spatial separation over energies

when propagating with the zero of the vector potential, the turning point of the electrons is longitudinal momentum dependent due to the Coulomb attraction of the ions after overshooting the pseudocapacitor field. Baeva *et al* showed that the electron bunch has a quasi-monoenergetic spectrum: the electron bunch is now of attosecond duration in the spectro-temporal domain and there is a one-to-one relationship between energy and position with the higher energies trailing the lower energies. The full bunch is confined to 130 as while a single energy is confined to 5 as. If, however, the plasma bulk is transversely mass-limited relative to the laser spot size, when rotated back towards the plasma block, some of the electron bunch will overshoot and escape the potential well without significant chirping of the bunch as can be seen in Figure 2.3. Such electron bunches retain their high charge density and ultra-short duration with the tradeoff of increased divergence. Note that electron bunch properties are imprinted in the transmitted harmonics: high divergence but attosecond duration.

ZVP electron bunches can therefore be placed into two categories: ultra-high charge, ultra-short duration electron bunches from mass-limited targets, hereafter labelled mass-limited electron bunches, of interest due to their unique properties, and bulk propagating bunches, hereafter labelled bulk bunches, which have lower charge densities, are imprinted with instabilities and are instead of interest due to their connection to energy absorption and reflection in this post-ponderomotive regime. To investigate these two bunch types further, 2D PIC simulations were performed, see the Appendix for parameters.

### Attosecond nano-Coulomb mass-limited electron bunches

The plots of Figure 2.7 describe a typical mass-limited ZVP electron bunch qualitatively. The electron bunch under interrogation is ultra-relativistic with a mean energy of 51(11) MeV and a duration of 35 as. It propagates at an angle of -0.393 rad relative to the laser propagation direction, *i.e.* the  $x$ -axis, and has a transverse geometric emittance in the simulation plane (the  $x$ - $y$  plane) of 35(7) nm rad. The calculation of the transverse geometric emittance, a measure

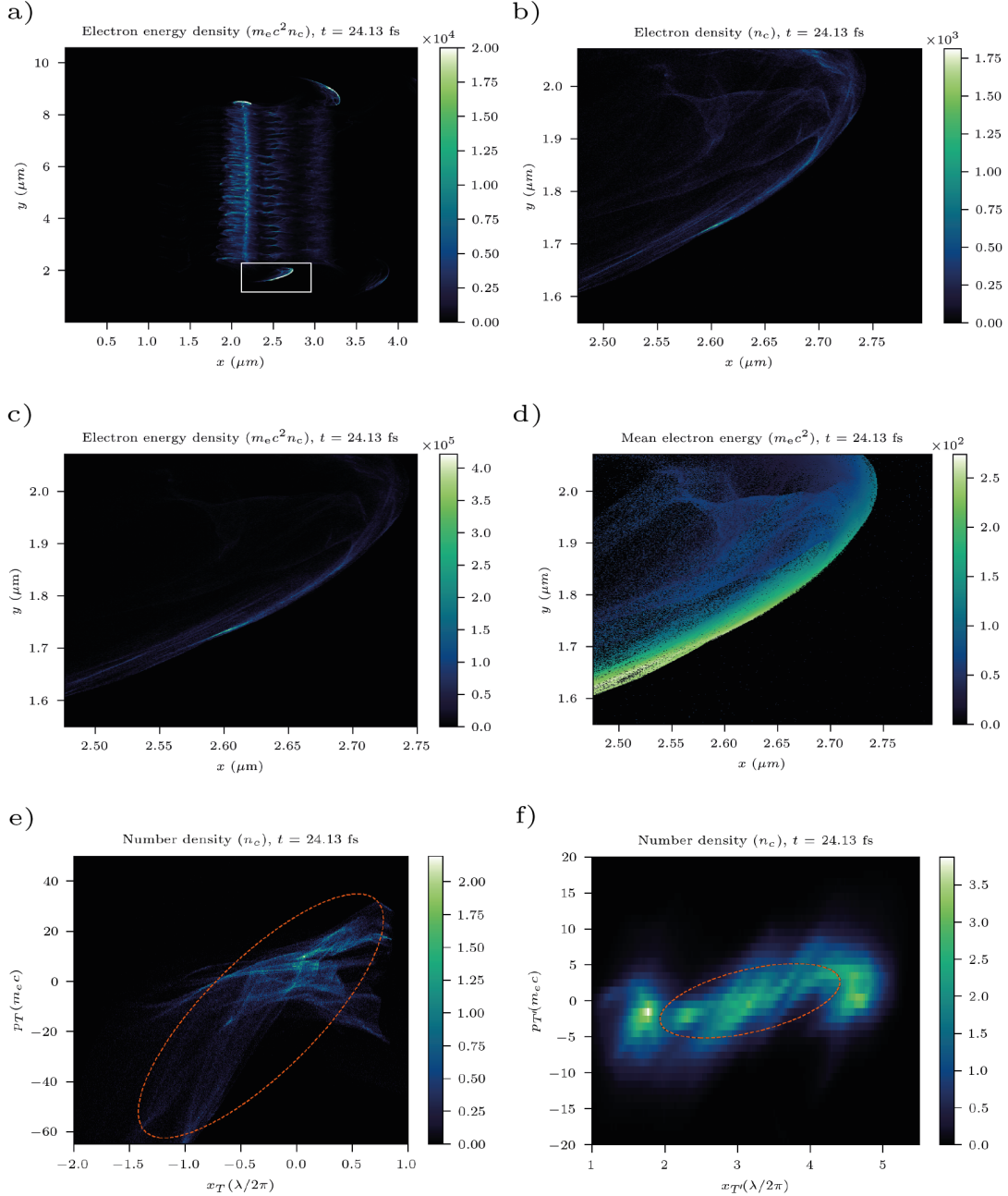


**Figure 2.7:** 2D PIC simulation results qualitatively describing typical mass-limited ZVP electron bunch structure. a) Electron energy density for the full simulation window, corresponds to Figure 2.3f). The box highlights the bunch presented in the following plots. b) Electron number density of the electron bunch. c) Electron energy density of the electron bunch, the colour bar scale has been increased compared to Figure a) to observe the internal structure. d) The mean electron energy across the electron bunch, suggesting a position-dependent energy or quasi-monoenergetic nature to the electron bunch [118]. Cells with no macroparticles are black. e) The transverse phase space in the 2D simulation plane. The ellipse describes the calculated emittance. The skew of the ellipse is a consequence of a low-density tail on the phase space beyond the bottom left corner. f) This plot was extracted from the equivalent 3D simulation and describes the transverse emittance in the  $z$ -direction. Again the ellipse marks the emittance. The relatively well-defined border to the phase space and the mild tilt (indicating only mild divergence) are direct consequences of the 2D nature of the interaction.

of the quality of the electron beam, is given in Appendix A.3. Note that while the bunch does not propagate in the laser propagation direction, this does not mean it must be rejected under consideration of the ZVP bunch conditions. We must expand the definition of a ZVP electron bunch. In the mass-limited case, a bunch must propagate at some angle to the laser due to conservation of canonical momentum while it remains in the thrall of the laser pulse. For an equivalent bunch in a corresponding 3D simulation, the transverse geometric emittance in the  $z$  plane is  $7.4(10)$  nm rad. This electron bunch has a total charge of  $0.35$  nC for a slab of plasma of thickness  $0.75\lambda$  in the  $z$ -direction. Note again the two-dimensional nature of the interaction geometry. Electrons a distance less than twice the relativistic Larmor radius,

$$r_L = \frac{\gamma m_e v}{e|\mathbf{B}|} \quad (2.45)$$

will escape to the side of the target when rotated back towards the plasma. Here,  $\gamma$  and  $v$  correspond to the electron velocity. The total number of electrons in the mass-limited bunch is

$$N = 2n_e r_L L_z \Delta x, \quad (2.46)$$

where  $L_z$  is the width of the plasma in the  $z$ -direction. Combining Equations 2.45 and 2.46 with 2.24 and 2.27 and taking  $v \approx c$  for the ultra-relativistic electron bunch,

$$N \approx 2\gamma n_c \frac{L_z}{k^2}. \quad (2.47)$$

Equation 2.47 can be rewritten in terms of fundamental constants as

$$N \approx 2(1 + 0.5 \frac{a_0^2}{n_e}) L_z \frac{m_e \epsilon_0 c^2}{e^2}. \quad (2.48)$$

For these simulation parameters, this corresponds to a total bunch charge,  $Q = eN$ , of  $0.37$  nC, a remarkably successful prediction of the ZVP model. Perhaps counter-intuitively, it would appear the total charge scales inversely with the plasma density. Instead, charge can be increased either by increasing the laser pulse intensity or  $L_z$ . Indeed, provided the laser pulse intensity remains relativistic, the focal spot can

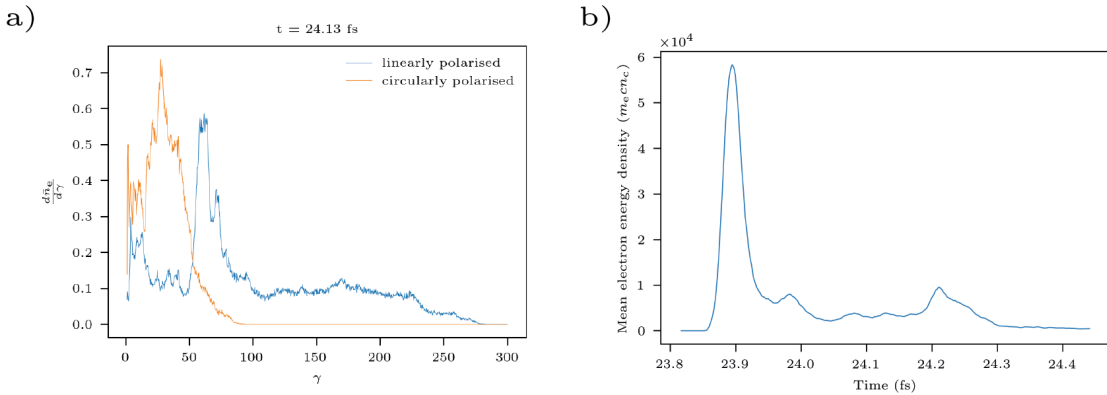


**Figure 2.8:** a) Energy spectra for mass-limited electron bunches formed via linearly and circularly polarised laser pulses. b) Mean energy density streaked in time through the centre of a mass-limited ZVP electron bunch demonstrating the attosecond duration.

be increased indefinitely and there is no limit to the mass-limited electron bunch total charge. For a realistic laser pulse with beam width  $10\lambda$  incident on a larger plasma block, Equation 2.48 predicts a charge of 9.3 nC.

Caution is necessary when the standard definition of emittance is applied to a non-Gaussian beam profile risking over- or underestimating the emittance. When applied to an ideal Gaussian distribution, the elliptical contour that defines the emittance contains 39.3 % of the beam particles [133], however, Figures 2.7 e) and f) contain 75.5 % and 38.6 % of the beam respectively. The large overestimate of the former is a consequence of the long low-density tail on the distribution to the bottom left of the plot.

Figure 2.8a compares the electron bunch energy to an equivalent bunch produced by a circularly polarised laser pulse<sup>3</sup>. The mean electron bunch energy is over three times lower as there is no ZVP acceleration phase and there is no quasi-monochromatic structure [118]. Figure 2.8 b) plots the mean electron bunch energy in time at a point as the bunch passes, clearly demonstrating the attosecond duration of the electron bunch.

<sup>3</sup>A circularly polarised laser pulse will expel electrons from a mass-limited target in a corkscrew shape, the bunch is therefore only loosely equivalent.

### Applications: from electron bunches to attosecond light

There are a plethora of applications for high charge, attosecond electron bunches, primarily for the purpose of resolving attosecond scale phenomena [134]. Already femtosecond pump, attosecond probe experiments are underway [135, 136] but the higher intensities and charge densities accessible in the laser-solid regime compared to in laser-gas interactions [113, 126] would represent a step-change in the field by enabling atto-pump atto-probe experiments [109]. Potential applications include: electron microscopy and atomic diffraction to temporally resolve photoelectric processes such as Bragg diffraction [137], ultra-fast electron radiography to probe the evolution of the formation of magnetic fields in dynamical systems [138] or for XFEL seeding [114]: the record XFEL X-ray pulse duration stands at 280 attoseconds [139], substantially longer than the durations accessible using this technique. Electron bunches are also a promising alternative for radiotherapy due to their superior penetration depth in biotissues compared to X-rays [140].

Analogously to the HHG process, rapid acceleration of an electron bunch generates a burst of radiation whose properties (brightness, coherency, duration, spectrum) are determined by the corresponding properties of the electron bunch (charge, emittance, duration and energy). Thus globally electron bunches are used as a diagnostic tool in synchrotrons and XFELs. Other acceleration mechanisms for X-ray generation include: bremmstrahlung radiation from firing the electron bunch at a secondary high- $Z$  target [141], interaction with a counter-propagating laser pulse [142, 143] or injection into a laser or plasma wakefield accelerator, including accessing the solid density plasma wakefield regime [113]. The mass-limited electron bunches produced via the ZVP mechanism have transverse emittances comparable in all planes to those conditioned in state-of-the-art nano-Coulomb electron bunch accelerators [144, 145]. Such facilities typically produce electron bunches with geometric emittances of  $\sim$  mm rad prior to damping ring injection [146] and  $\sim$  nm rad post-injection [144]. Thus, the mass-limited ZVP electron bunches are ideal candidates for the production of bright X-rays of unprecedentedly short

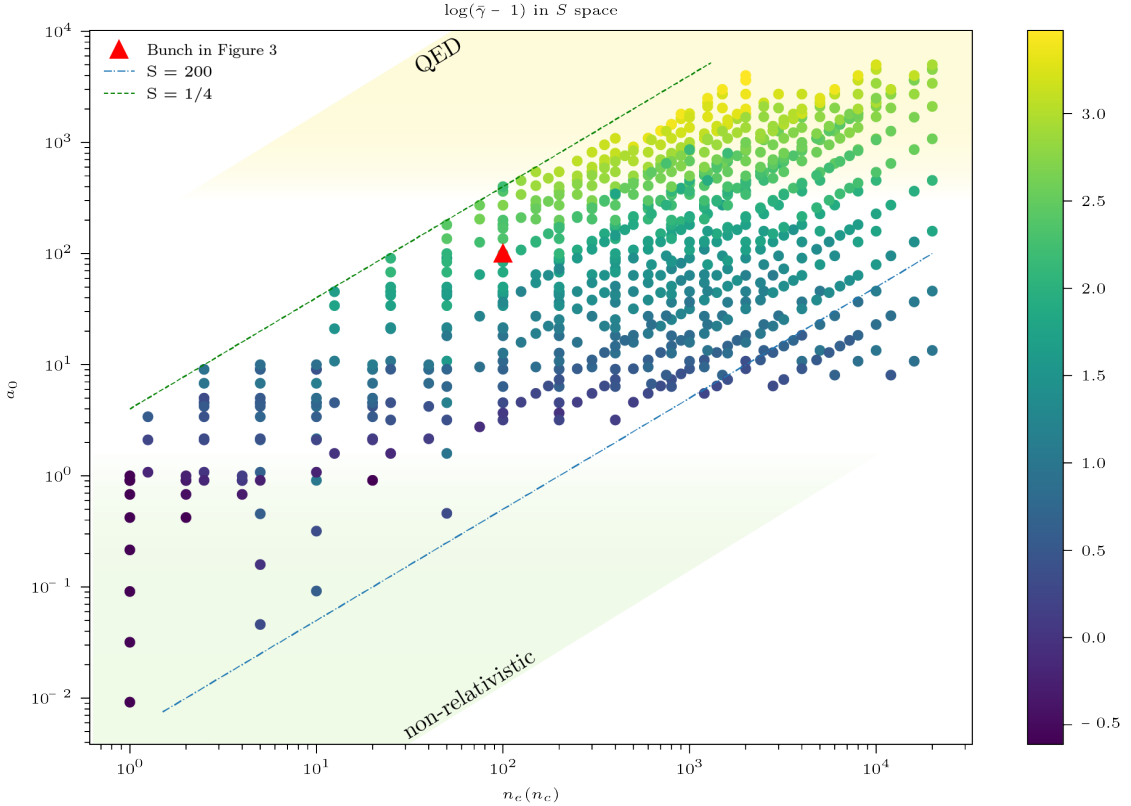


**Figure 2.9:** Mean mass-limited ZVP electron bunch normalised kinetic energies extracted from 2D PIC simulations. The bunch detailed in Figure 2.7 is highlighted.

duration and are suitable for study in the new attosecond regime with applications to physical, chemical and biological systems.

#### Parameter scan of electron bunch mean energy

It is important to confirm that mass-limited electron bunches follow the same scaling relations as has previously been confirmed for bulk ZVP electrons in both 1D [118] and 2D [117] PIC simulations. The mean mass-limited electron bunch kinetic energies were extracted from 120 2D PIC simulations and are plotted in Figure 2.9. The dependence of the energy on both  $a_0$  and  $\bar{n}_e$  is immediately apparent and therefore these electron bunches are accelerated by a non-ponderomotive mechanism.

The parameter scan took plasma block densities ranging from the critical plasma density to well-beyond solid density for the aluminium target and with laser pulse peak intensities ranging from non-relativistic ( $a_0 < 1$ ) through to the Quantum Electro-Dynamics (QED) plasma regime ( $a_0 > 300$ ) up to a peak  $a_0 = 5000$  to

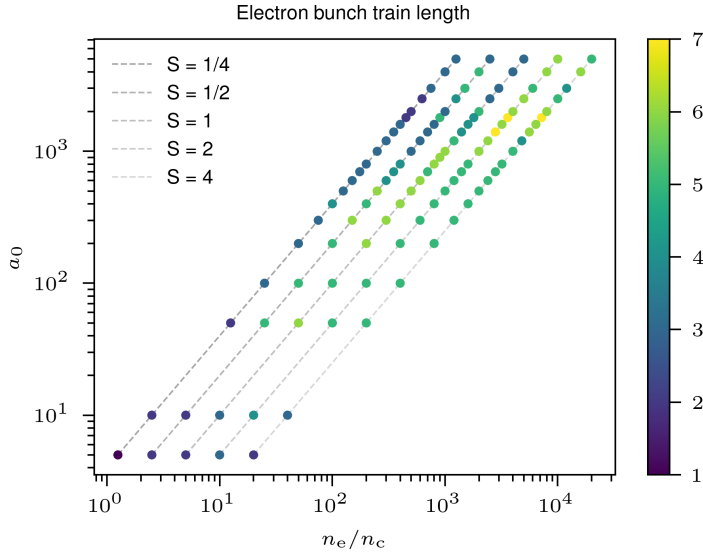


**Figure 2.10:** Mass-limited electron bunch train length as a function of laser intensity and plasma density. Lines of constant peak  $S$  parameter are plotted for reference. Clearly, decreasing  $S$  reduces the bunch length.

investigate the change in scaling observed by Savin *et al* [127] at the onset of QED effects. This study is also the first to extract specific bunch energies as opposed to total simulation box energy gain, representing a far more precise test of ZVP theory. Particle merging was turned on for macro-photons and macro-electrons for  $a_0 \geq 1800$  to prevent overloading of the available supercomputer memory due to the vast number of particles produced in this SF-QED regime.

A total of 856 data points for mass-limited electron bunch mean energies were extracted from the simulations. Bunches are arranged in trains with an average length of 4, however, isolated bunches are more useful for attosecond diagnostics. The number of bunches in a given train as a function of simulation peak intensity and plasma density is plotted in Figure 2.10. It is clear that reducing the peak  $S$  reduces the train length. Where  $S < 1$ , the transition to relativistic self-induced transparency occurs in the rising edge of the laser pulse corresponding to a breakdown of ZVP and an early cutoff to the bunch train. Other routes to isolated attosecond electron bunches can be likely borrowed from CSE theory given the close relation between the two. The interest in isolated attosecond pulse of radiation has led to the proliferation of ideas, suggested techniques include using the attosecond lighthouse

technique using laser pulse wavefront rotation [147], few-cycle laser pulses[148], non-collinear laser pulse gating [149] and circular polarisation gating [150].

Return now to Figure 2.9. The ZVP energy relations must be modified before comparison to the data since these electron bunches experience a further direct laser acceleration phase before reaching the measurement point. Thévenet *et al* [115] suggested that attosecond electron bunches produced in reflection exhibit precisely the phase and energy properties required to ‘surf’ the reflected laser pulse and experience vast acceleration gradients over the Rayleigh length of the laser pulse. This process is known as Vacuum Laser Acceleration. Potentially providing a route to a fully optical scheme to create GeV nano-Coulomb electron bunches. Certainly, some of the bunch will have the necessary injection close to the laser propagation axis, however much of the bunch propagates at an angle to the laser and this must be accounted for. Interestingly in Figure 4.1 modelling oblique incidence, more of the bunch appears to propagate along the axis. A parameter scan is necessary to find the optimal parameters.

Electrons are ejected from the plasma in phase with the subsequent laser pulse cycle peak and diverge outwards from that point. Near to the laser focus, the electrons experience a field

$$\mathbf{E}(x, y, t) = E_0 e^{-(y-f_y)^2/w_L^2} \cos(k_L(x - f_x) - \omega_L t) \hat{\mathbf{y}} = E_0 f(x, y, t) \hat{\mathbf{y}}. \quad (2.49)$$

The work done by this field is then

$$\Delta T = \int e \mathbf{E} \cdot d\mathbf{x}. \quad (2.50)$$

Note that for this process, the laser pulse electric field and electron bunch direction of travel will always be aligned no matter to which side of the plasma bulk the electrons are accelerated and therefore  $\Delta T$  will always increase the energy of the electron bunch. The electron trajectories can be approximated at linear from the ejection point  $(y_e, x_e)$  to the observation point  $(y', x')$ , correspondingly,

$$x = y \frac{(x' - x_e)}{(y' - y_e)}, \quad t = \sqrt{x^2 + y^2}/c. \quad (2.51)$$

Equation 2.50 can now be integrated along a given electron's path and therefore the gamma factor increases by

$$\Delta\gamma = \int \frac{eE_y(y)dy}{m_e c^2} = a'_0(y)F, \quad (2.52)$$

where  $a'_0$  is the vector potential of the subsequent laser pulse cycle peak and

$$F = \frac{2\pi}{\lambda} \int f(y)dy. \quad (2.53)$$

The gamma factor gain from the ZVP acceleration phase is determined by the electric field at the corner of the plasma block,

$$\Delta\gamma_{ZVP} = \frac{(a_0 e^{-(2\lambda - y_f)^2/L_0^2})^2}{2\bar{n}_e} = 0.31 \frac{a_0^2}{\bar{n}_e}. \quad (2.54)$$

Thus,

$$\gamma = 1 + (0.31) \times \frac{a_0^2}{\bar{n}_e} + F \times a'_0. \quad (2.55)$$

This final term could be neglected or at least reduced somewhat once super-Gaussian spatial laser pulses become standard in this intensity regime or by using a suitable plasma separator [151], as applied in [152]. Both acceleration phases fail to meet the criteria of the Lawson-Woodward theorem. The ZVP phase is dependent on the existence of electrostatic forces, while the secondary phase occurs for a finite interaction region.

The data of Figure 2.9 is taken from two measurement points, enabling two  $F$  values to be investigated. Fits to Equation 2.55 were made for each data set using the Ordinary Least Squares regression model of the statsmodels Python module [seabold2010statsmodels], allowing the constants to vary. The non-linear ZVP energy can be applied to the linear model via construction of the necessary composite parameter. Both fits were successful with  $r^2$ -values of 0.81 and 0.84 and found the same ZVP pre-factor  $F_{ZVP} = 0.47 \pm 0.02$ , slightly above that anticipated from the model. The model is sensitive to the laser pulse intensity, likely much of the bunch originated from closer to the laser pulse focus than the target corner explaining the higher value.

The first data set measurement point was  $(0.41 \mu\text{m}, 0.25 \mu\text{m})$  from the target edge. This gives  $F = 0.31$  compared to  $0.22 \pm 0.02$  predicted by the fit. The second, at  $(0.41 \mu\text{m}, 0.31 \mu\text{m})$  from the target edge giving  $F = 0.39$  compared to  $0.34 \pm 0.02$  from the fit.

This is the first demonstration of ZVP theory to calculate absolute values and not only the scaling relationship. Such order of magnitude calculation is essential for the comparison to other absorption models and the determination of dominant modes. It is certainly remarkable that such a simple theory for energy absorption has such predictive success in this highly non-linear and seemingly chaotic many-particle system. It is interesting that increasing laser intensity to such extremes will, at least for a short time, cause relativistic effects that simplify the dynamics before the total annihilation of a target.

The relative error between data and theory is plotted in Figure 2.11. Those points marked by an orange triangle have associated errors of over an order of magnitude. Reassuringly, such points occur only after the onset of QED effects, known to impact the ZVP mechanism [127] and for  $S < 1$ , that is, where the plasma becomes relativistically transparent to the laser pulse, a fundamentally different regime. The model is inconsistent in the non-relativistic domain as can be expected. It is particularly interesting that there is no indication that large  $S$  causes a breakdown of the model, extending the applicability of the model further than previously considered and opening up the field to a wider range of conditions, such as that of shock compressed plasmas. To summarise, it would appear the ZVP model is valid for  $10 \leq a_0 \leq 300$  and  $S \geq 1$ .

### 2.4.1 Energy absorption in the ZVP regime

As stated previously the laser-plasma coupling exists in a state of adiabaticity with the exception of the ZVP acceleration phase and hence Equation 2.29 describes the absorption of laser pulse energy. As two bunches are produced per laser pulse cycle, the rate of energy transfer is, therefore,

$$R = \frac{U\omega_L}{\pi}, \quad (2.56)$$

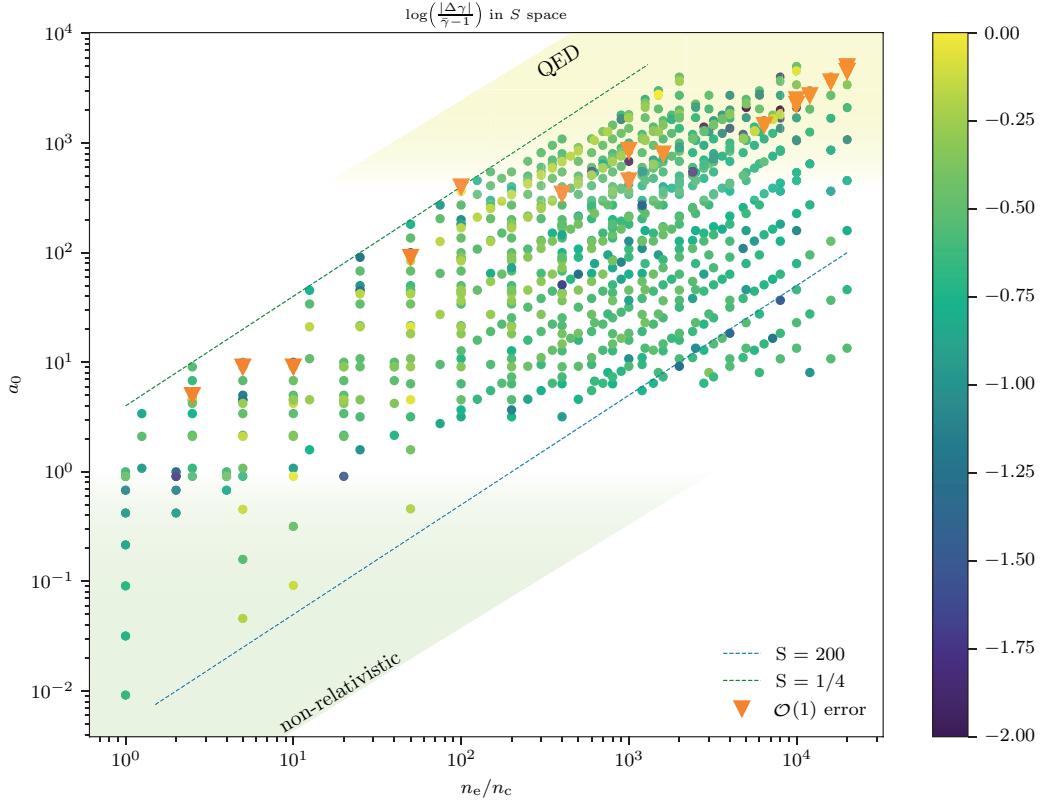


**Figure 2.11:** The relative errors for each mean energy data point compared to Figure 2.9. The orange triangles indicate data points for which the model fails to predict the mean energy.

for normal incidence. To observe the scaling for  $U$  in 2D PIC simulations, peak instantaneous electron bunch energies escaping to the rear of the bulk were extracted from those PIC simulations with  $S = 1$ . For constant  $S$ ,

$$U \sim a_0^2. \quad (2.57)$$

Energies are plotted in Figure 2.12. Fitting the total energy within the range of validity established for the ZVP model finds

$$U \sim a_0^{2.01 \pm 0.003}, \quad (2.58)$$

reproducing with great success the anticipated scaling within the ZVP regime. It is satisfying that the number of electrons and bunch mean energies both follow their anticipated ZVP scalings. It was not possible to reproduce the constants of Equation 2.29 as the neutralising return current in the plasma bulk generates an electrostatic

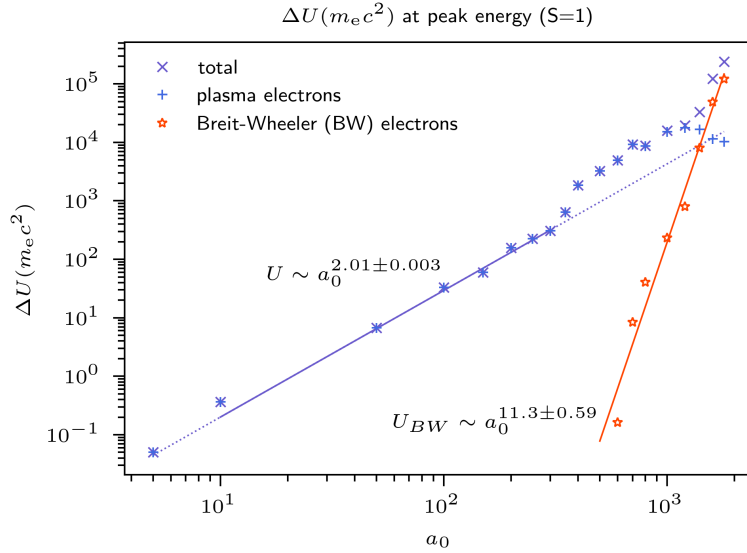


**Figure 2.12:** Peak instantaneous bulk electron bunch total energies after escaping to the plasma bulk rear. Energies begin to deviate from the anticipated scaling at approximately  $a_0 = 300$ . Above  $a_0 = 1000$ , BW pair-produced electrons begin to dominate and the peak energies rise rapidly.

field on the rear side of the plasma block, decelerating bulk electron bunches as they escape the plasma. It should be possible to calculate the deceleration by considering the number of electrons expelled by the plasma. It is, however, clear from the simulations that at least some electrons in the escaping bunch are trapped by this rear-side potential well reduces its ability to slow electrons.

While Equation 2.29 describes energy absorption into hot electron bunches, the coupling of such hot collisionless electrons to the bulk plasma given the lack of collisionality is naturally indirect. There are two key mechanisms [153]. Firstly, via a cooler resistive return current of electrons that neutralises the current of the injected hot electrons that escape the potential well of the front surface. Since all hot electrons travel at approximately speed  $c$ , the magnitude of the return current depends not on the total energy absorbed but instead on the total number of electrons injected, as given by Equation 2.28, depending linearly on laser spot area and the electric field magnitude and not on the plasma density<sup>4</sup>. Secondly, via the formation

<sup>4</sup>Note that for a sufficiently thin target, the return current induces an electrostatic field on the back surface of the target which can then reflect hot electron bunches and decelerate them to the point of a return to collisionality. This is a reality for the PIC simulations explored in this thesis, however, since realistic targets are much thicker this shall be neglected.

of large amplitude bulk plasma waves induced in the wake of the hot electron bunches. Sherlock *et al* [153] calculate the magnitude of the induced wakefield to be

$$E_W = \frac{eN_e c}{\omega_p \epsilon_0} = \sigma \sqrt{\frac{m_e \epsilon_0}{n_e}} E_L, \quad (2.59)$$

where here the bunch velocity has been set to  $c$ , bulk electrons will be accelerated by  $E_W$  and their kinetic energy converted to heat via collisions. Interestingly, this reproduces the mid-temperature electron scaling with density that was observed by Chrisman *et al* [154] in their study of hot electron energy coupling in cone-guided fast ignition of inertial fusion targets. This is a different possible explanation to their self-declared ‘hand waving argument’. Excluding this study, such formulations for heat transfer to the plasma bulk within the ZVP regime remain untested in simulations.

Note also that as the laser pulse intensity rises, the fraction of energy absorbed by the ion species increases. Savin [119] determined for  $S = 1/2$ ,  $a_0 = 100$ , that this would be almost 20%. Energy is absorbed by ions via the hole-boring mechanism as described later in this Thesis.

#### 2.4.2 Unpacking the QED effects of Figure 2.12

In Savin’s acclaimed paper [127], they determined theoretically and demonstrated in simulation that at  $a_0 = 300$ ,  $n_e = 50n_c$ , there is a transition from standard ZVP scalings to an enhanced QED scaling associated with Breit-Wheeler (BW) electrons increasing the pseudocapacitor plate charge. Explicitly,

$$T \sim \frac{a_0^5}{\bar{n}_e}. \quad (2.60)$$

At first glance of Figure 2.12, Savin’s results are inconsistent with this parameter scan. Perhaps the measurement method can explain this via the well-known effect of radiation trapping from to RR [155], also observed in these PIC simulations. After acceleration across the pseudocapacitor, the electron bunch encounters the subsequent laser peak. If the electron bunch gamma factor and laser intensity are both large enough, electrons radiate a significant fraction of their energy and are thus stopped in their tracks. Unable now escape the potential well at the plasma

surface they are trapped and are not observed to escape the plasma until the laser pulse intensity reduces. Such an effect would not impact Savin's scalings but would of course inhibit the observation of the scaling for electrons rear of the plasma block. Note that should this be the case and the collisionless electron bunches remain within the plasma bulk, Savin's ZVP QED model truly applies directly to energy absorption by the plasma bulk.

There is another interpretation. Returning now to Figure 2.12, there are two interesting aspects. Firstly, the sudden jump in total energy at  $a_0 \approx 300$ . This cannot be explained by ZVP theory nor QED theory since the jump is observed with QED effects switched off. Secondly, the even sharper jump in total electron bunch energy above  $a_0 = 1000$ . Decomposing the total energy into bulk electrons and those produced via the BW process, this is clearly a QED effect. Energy in BW produced electrons scales at a staggering

$$U_{\text{BW}} \sim a_0^{11.3 \pm 0.8}, \quad (2.61)$$

while the energy of bulk plasma electrons decreases. Perhaps this is a signal of Savin's QED ZVP electron bunches only at a higher energy due to the substantially greater plasma density of these simulations. The reduction in bulk electron energy can be attributed to an oversaturation of the front surface with BW electrons.

Combining equations 1.54 and 2.29 and assuming the electron radiates all its energy to the photon, for the ZVP mechanism, at the point of emission one finds

$$\chi_\gamma = \frac{\sqrt{2}|\mathbf{E}|}{E_S} \frac{a_0^2}{\bar{n}_e}. \quad (2.62)$$

The probability of BW pair production begins to rapidly increase around  $\chi = 1$ , therefore, the transition to QED will occur at

$$a_0 \approx \left( \frac{E_S}{\sqrt{2}} \frac{e\bar{n}_e}{m_e c \omega_L} \right)^{1/3} = \left( \frac{a_s \bar{n}_e}{\sqrt{2}} \right)^{1/3}, \quad (2.63)$$

where  $a_s = 7.73 \times 10^5$  is the normalised vector potential associated with the Schwinger Field. Repeating the calculation instead as a function of  $S$ , one finds instead

$$a_0 \approx \left( \frac{a_s S}{\sqrt{2}} \right)^{1/2}. \quad (2.64)$$

This corresponds to a transition to rapid pair production with Savin's parameters of  $a_0 \approx 301$  versus  $a_0 \approx 739$ , consistent with both studies. This is interesting, ZVP with Savin parameters predicts a significantly lower transition to QED compared to the Wilks scaling for  $\mathbf{J} \times \mathbf{B}$  heating. Following Savin's QED ZVP theory, one can predict

$$U_{\text{QED}} \sim \frac{a_0^7}{S}, \quad (2.65)$$

therefore much work remains to understand the scaling of Figure 2.12 and unify these results, starting with the application of the methods of this analysis to the parameter space explored by Savin. Undoubtedly, the advent of next-generation exa-watt scale lasers and access to this regime will be exceedingly interesting if such scalings in bunch energy can be maintained.

Linear Breit-Wheeler can safely be neglected in these simulations. There is simply not enough energy in the system. For two interacting photons of energy  $E_1$ ,  $E_2$ , by consideration of four-momenta, the threshold condition for pair production is

$$E_1 E_2 \geq (m_e c^2)^2. \quad (2.66)$$

For a near-infrared laser photon of energy  $\hbar\omega_L$ , the interacting photon must have an energy in excess of 200 GeV. Despite the extreme acceleration gradients considered in this thesis, the ZVP mechanism predicts photons of energies no greater than 10 GeV and thus linear Breit-Wheeler is suppressed.

He *et al* [156] identified an alternative mechanism for linear BW using solid density targets, where forwards- and back-scattered high energy radiation reaction-produced photons interact within a hollowed-out plasma channel. In the geometry of interest in this thesis, while photons are produced in both directions, their production is localised to the plasma surface and at no points do their paths cross thus this mechanism does not occur.

### 2.4.3 Errors

A set of simulations were undertaken to explore the stability of some assumptions of the PIC simulations. The effect of including collisions, increasing the temperature

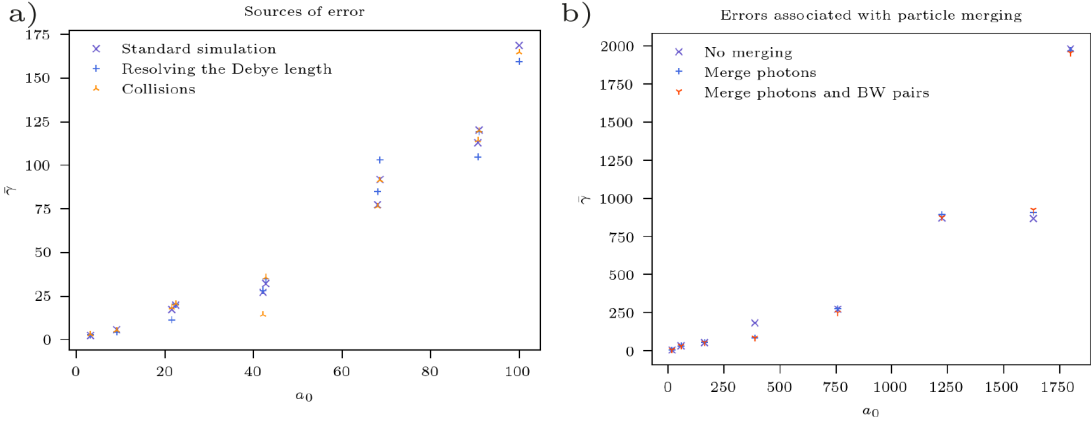


**Figure 2.13:** An exploration of ZVP 2D PIC simulation stability and assumptions. a) Electron bunch mean energies extracted from simulations with  $a_0$ ,  $\bar{n}_e = 100$ . Here, the  $x$ -axis is the normalised vector potential of the laser pulse cycle that made them, this is why there appears to be results stacked. b) Electron bunch mean energies extracted from simulations with  $a_0$ ,  $\bar{n}_e = 1800$  both with and without particle merging.

to resolve the Debye length and particle merging were explored. The results are presented in Figure 2.13. In general, including collisions had little to no effect on the results and changing the Debye length had a small but not systematic impact on the results. Note that while numerical heating is not directly dependent on laser intensity, increases to  $a_0$  would increase the electron bunch density. Thus, resolving the Debye length of the ultra-high density (orders of magnitude greater than solid density) electron bunches produced by the higher laser pulse intensities considered here is no straightforward task. Particle merging was essential for simulations with  $a_0 > 1800$  due to the proliferation of high energy photons and electron-positron pairs. At least at  $a_0 = 1800$ , it would appear particle merging had negligible impact, however, it is likely the error would increase with  $a_0$ .

## 2.5 Conclusions

The Zero Vector Potential mechanism describes the post-ponderomotive rapid absorption of ultra-relativistic laser energy by a solid density overdense, collisionless and fully ionised plasma on the timescales of ion immobility. The defining characteristics of the mechanism have been identified in 3D PIC simulations including the observation of a zero of the vector potential propagating at speed  $\approx 1.4c$  through

a high-density ZVP electron bunch at the front surface of the plasma early in the ablative journey of the electron bunch. Simulations have suggested that from currently operational 10 PW short pulse laser facilities and foam targets, the ZVP mechanism can produce a train of attosecond duration, nano-Coulomb electron bunches, each with a transverse emittance of a few nm rad. Such charge and quality are comparable to state-of-the-art electron bunch accelerators but on paradigm-shifting timescales. Such timescales being those on which atomic processes occur, these electron bunches could be manipulated to literally ‘shed light’ onto fundamental biological and chemical processes. Via a massive 2D PIC parameter scan the energies of such mass-limited electron bunches have been compared to those predicted by the ZVP model, identifying a range of validity for the model, specifically  $a_0 > 10$ ,  $S > 1$ . These simulations were also used to confirm the energy absorption scaling in 2D up to and into the QED regime. Chapter 4 details the upcoming GEMINI PW experiment to observe ZVP electron bunches for the first time. On the theme of experimentation, the following Chapter will now switch gears from absorption to reflection for the discussion of recent results from the ORION laser facility.

# 3

## Attosecond X-ray harmonics on the ORION laser facility

### Contents

---

<b>3.1</b>	<b>Introduction</b>	<b>72</b>
<b>3.2</b>	<b>Theory</b>	<b>73</b>
3.2.1	The ROM model	73
3.2.2	The normalisation factor	78
3.2.3	Hole boring	79
3.2.4	Harmonic source size	83
3.2.5	The SHHG optimal parameter space	83
<b>3.3</b>	<b>Simulations</b>	<b>85</b>
3.3.1	1D PIC simulations of HHG	85
3.3.2	Hydrodynamic simulations of preplasma formation	91
<b>3.4</b>	<b>The experiment</b>	<b>96</b>
3.4.1	Targets	100
3.4.2	Contrast and plasma mirrors	101
3.4.3	KBRXM	101
<b>3.5</b>	<b>Experimental data processing</b>	<b>102</b>
3.5.1	Image plate calibration	102
3.5.2	OHREX calibration	104
3.5.3	Extracting the data	105
<b>3.6</b>	<b>Experimental results</b>	<b>108</b>
<b>3.7</b>	<b>Summary</b>	<b>112</b>

---

### 3.1 Introduction

The simulations of Chapter 2 are a relatively efficient and cost-effective means of study. High-power laser experiments are a cumbersome technical challenge. However, the proliferation of errors in simulation codes inevitably generates significant deviation from reality, while reality itself diverges from the idealistic conditions modelled by the codes. For now, at least, experimentation remains an essential component of the scientific method. Expectations must also be scaled back to reality. This chapter reports on the March 2023 experiment on the ORION laser facility, AWE, Aldermaston, the UK’s most powerful laser system. And yet, it cannot access the ZVP parameter space at these intensities and pulse durations: the  $S$  parameter is too large and the preplasma scale length too steep. Instead, this chapter will focus on the ROM model of HHG. This model describes the properties of radiation reflected from a relativistic laser pulse interaction with a solid-density plasma, another related route to bright attosecond light sources.

A fundamentally different mechanism to its Nobel prize-winning counterpart, SHHG from solids has demonstrated significantly higher conversion efficiencies and, relying on plasma oscillations not ionisation, does not suffer from the same limits to applied intensity [157]. SHHG has thus become a field of considerable interest for the production of bright coherent attosecond harmonics. It was first observed from the interaction of a CO<sub>2</sub> laser-solid interaction in 1981 [158], followed shortly by the theoretical justification [159]. Interest in HHG was revived by the arrival of CPA technology enabling access to unprecedented laser pulse intensities and ever higher harmonic orders. To describe this relativistic interaction, 1994 saw the arrival of a new theory, the **OMM!** (**OMM!**) [160]. In this regime, harmonics were seen to be formed by the Doppler effect induced by a thin reflecting charge sheet at the plasma surface oscillating periodically with the laser pulse. This theory predicts a cutoff harmonic number of  $n_c = 4\gamma_s^2$ , where  $\gamma_s$  is the maximum gamma factor of the charge sheet. This relatively low cutoff is at odds with experimental results, the current record standing at the 3200<sup>th</sup>harmonic observed on the Vulcan PW laser system in 2007 [161]. It was only after the development of relativistic

similarity theory [78], which laid the groundwork for Baeva's ROM model, that the experimentally observed cut-off could now be explained [125]. Since ORION and Vulcan parameter spaces are similar, this is the most appropriate description of SHHG and is described in more detail in Section 3.2.

There are many fascinating applications for SHHG beyond that of attosecond physics. The high photon energy content of the harmonic beam has excellent penetration into dense materials with preliminary studies indicating notable improvement in energy absorption, suitable for auxiliary heating of ICF targets [162]. This high energy content also enables the focusing of the harmonic beam to significantly smaller spot sizes than the incident diffraction-limited laser pulse. An all-optical coherent focusing of high harmonics with realistic laser parameters has been shown to produce over 1000 times intensity gain [163], thus providing a realistic route to the Schwinger limit [164], improving the odds of observation of photon-photon scattering [165] or of gravitational waves from twisted light [77]. Simulations have shown how a harmonic beam can probe SF-QED if a solid target is placed at the new focal position [82].

This chapter reports on the March 2023 experimental campaign at ORION to observe and measure the absolute intensity of X-ray harmonics generated via ROM HHG. Section 3.2 covers the theory of the ROM model of HHG from relativistic laser solid interactions. Section 3.4 outlines the experiment design while 3.3 presents simulation results that guided both that design and the data analysis.

## 3.2 Theory

### 3.2.1 The ROM model

For the moderately relativistic sub-picosecond ORION SP1 and SP2 beamlines, the most appropriate description of their non-linear interaction with a solid density target is the Relativistic Oscillating Mirror (ROM) model. The full technical formulation constitutes the main body of Baeva's 2008 thesis [166]. A notably more rigorous derivation than the original paper on the same topic [125]. This is achieved via application of the highly generalised **ARP!** (**ARP!**) formalism

to the case of  $S > 1$  in relativistic similarity theory, showing that the **ARP!** coincides with the relativistic critical density surface. This section provides a more qualitative, physically motivated description of this theory. The salient point of Baeva's thesis is that, while the surface motion is generally complex and parameter space dependent, at the moment relevant for HHG, the surface motion is always parabolic. By application of the Bourdier method [167], Baeva demonstrated that the envelope of the spectral content of the reflected beam does not deviate from the normal incidence linearly polarised case for either s- or p-polarised incidence. Hence, the following discussion is restricted to normal incidence. Starting with relativistic similarity theory and Equation ??,  $\mathbf{p} \sim a_0$ . As discussed in Section 2.2, microscopically electrons follow similar relativistic trajectories. However, from Equation 2.5,  $v_{\text{prop}}$ , the velocity of electrons along the propagation axis of the laser pulse, is not necessarily relativistic except at the passing of the zero of the vector potential where  $v_{\text{prop}} \rightarrow c$ . Macroscopically, the well-defined critical density surface within the skin depth (located at  $S = 1$ ), has a gamma factor that tracks the electrons' velocity along the propagation direction ( $x$ -direction) at that point,

$$\gamma_s = \frac{1}{\sqrt{1 - v_{\text{prop}}^2/c^2}} = \sqrt{\frac{1 + a(t, x)^2 + p_{\text{prop}}^2/(m_e c)^2}{1 + a(t, x)^2}}. \quad (3.1)$$

Equation 3.1 indicates surface gamma factors of order unity except at zeros in the vector potential where  $\gamma_s \sim a_0$ . In the vicinity of the zero,  $a \sim a_0 \sin(\omega_L t) \approx a_0 \omega_L t$ . Thus, while the velocity of the surface is a smoothly varying function around the maximum,  $v_{s,\max} \sim 1 - \mathcal{O}(a_0^{-2})$ , the *gamma factor spikes* as the vector potential passes through zero. At this point, the surface emits high-frequency photons. The surface radiates such photons only in the vicinity of the gamma spike. Thus, the pulse width can be approximated. In ZVP theory, zeros overtake the emitted photons and radiation from the extended electron bunch that is emitted first arrives at the observer last. In the ROM regime, Baeva demonstrates zeroes move at speed  $c$ . Consequently, all points in the skin depth radiate coherently. Since the radiation overtakes the sub-light speed surface, photons emitted from the surface first are

observed first. The radiation emitted therefore has a duration of

$$\Delta l \approx (c - |\mathbf{v}_{s,\max}|) \Delta t \approx \frac{\Delta t}{\gamma_{s,\max}^2}, \quad (3.2)$$

where  $\Delta t$  is the temporal duration of the gamma spike.

Writing the surface velocity as a smooth function around its maximum,

$$\mathbf{v}_s(t) = -(v_{s,\max} - c\alpha(\omega_L t)^2) \hat{\mathbf{x}}. \quad (3.3)$$

Without loss of generality, the peak of the gamma spike is set to  $t = 0$  for cleaner notation. Around the gamma spike, the surface gamma factor is thus

$$\gamma_s(t) \approx \frac{1}{\sqrt{1 - (\mathbf{v}_{s,\max}/c)^2 - 2\alpha(\omega_L t)^2}}. \quad (3.4)$$

Since  $1 - (\mathbf{v}_{s,\max}/c)^2 = 1/\gamma_{s,\max}^2$ , the duration of the gamma spike scales as

$$\Delta t \sim \frac{1}{\sqrt{\alpha}\omega_L \gamma_{s,\max}}. \quad (3.5)$$

Hence,  $\Delta t \sim a_0^{-1}$  and  $\Delta l \sim 1/a_0^{-3}$  and the cut-off frequency corresponding to the highest frequency component of the pulse is

$$\frac{\omega_c}{\omega_L} \sim \sqrt{\alpha}\gamma_{s,\max}^3 \sim a_0^3. \quad (3.6)$$

Equation reproduces the cut-off of the full derivation. Within the ROM model, this sharp pulse of radiation is masked by the low-order harmonics. Filtration is necessary to realise the attosecond duration of the high harmonic pulse.

The harmonic spectrum envelope for photon energies below the cut-off can be calculated from examination of the fields at the surface. Consider the Poynting vector

$$\mathbf{S} = \frac{1}{\mu_0} \mathbf{E} \times \mathbf{B}. \quad (3.7)$$

Regardless of the complex internal dynamics of the skin layer, an external observer will identify based on the fields observed in vacuum that the point of reflection (the apparent reflection point,  $x_s$ ) occurs where  $\hat{\mathbf{n}} \cdot \mathbf{S}(x_s, t(x_s)) = 0$ , here  $\hat{\mathbf{n}}$  is normal to the plasma surface. Correspondingly,

$$\hat{\mathbf{n}} \times \mathbf{E}(x_s, t(x_s)) = 0. \quad (3.8)$$

This represents a balance of the electric fields at the ARP. Decomposing into the incoming and reflected waves at the boundary,

$$E_i(x_s(t) - ct) = -E_r(x_s(t) + ct) \quad (3.9)$$

for all  $t$ . Applying the approximation of a plane wave, the phase structure at the reflection point is maintained as the reflected wave propagates away from the interaction region to the observation point ( $E_r(x_s(t) - ct) = E_r(x' - ct')$  for an observation point  $(x', t')$  near an electric field peak.). Thus, determining the modulation of the reflected beam is akin to solving Equation 3.9.

Writing  $\Phi = x_s(t) - ct$ ,  $\Psi = x_s(t) + ct$  and taking the time derivative of Equation ??,

$$\frac{dE_r(\Psi)}{d\Psi} = \frac{c - v_s(t)}{c + v_s(t)} \frac{dE_i(\Phi)}{d\Phi} \quad (3.10)$$

where  $v_s(t)$  is given in Equation 3.3. Integrating Equation 3.3, the reflected wave phase is

$$\Psi(t) = \Psi(0) + \frac{ct}{\gamma_{s,\max}^2} + \frac{1}{3}c\alpha\omega_L t^3. \quad (3.11)$$

Very close to the gamma spike peak the linear term dominates the interaction, corresponding to the highest order harmonics as previously discussed. The non-linear term dominates for

$$\delta\Psi = |\Psi(t) - \Psi(0)| \gg \left(\frac{3}{\alpha}\right)^{1/2} \frac{c}{\omega_L \gamma_{s,\max}^3}. \quad (3.12)$$

Note the correspondence between Equation 3.2.1 and the right-hand side of Equation 3.12. In this regime,

$$t = \left(\frac{3\delta\Psi}{c\alpha\omega_L}\right)^{1/3}. \quad (3.13)$$

At such intermediate times around the gamma spike, the linear term can be neglected, this is equivalent to writing  $v_{s,\max} = c$ . Thus,

$$\frac{dE_r(\Psi)}{d\Psi} = \left(\frac{2c - c\alpha(\omega_L t)^2}{c\alpha(\omega_L t)^2}\right) \frac{dE_i(\Phi)}{d\Phi}. \quad (3.14)$$

Assuming the incoming radiation is slowly varying around the short duration of the gamma spike,  $dE_i(\Phi)/d\Phi \approx dE_i(\Phi)/d\Phi|_{\Phi=\Phi(0)}$  produces something easily integrated,

$$\frac{dE_r(\Psi)}{d(\delta\Psi)} = \frac{2}{\alpha^{1/3}} \left( \frac{c}{3\omega_L^2 \delta\Psi} \right)^{2/3} \frac{dE_i(\Phi)}{d\Phi}|_{\Phi=\Phi(0)}. \quad (3.15)$$

Hence,

$$E_r(\Psi) = -E_i(\Phi(0)) - \left( \frac{3c^2}{\alpha\omega_L^2} \right)^{1/3} \frac{dE_i(\Phi)}{d\Phi}|_{\Phi=\Phi(0)} \times (\delta\Psi)^{1/3}. \quad (3.16)$$

From simple phase modulation, the reflected radiation gains the quasi-singularity

$$E_r(x, t) = \text{const}_1 - \text{const}_2 \times (ct - x)^{1/3}. \quad (3.17)$$

Accordingly, the harmonic content near the gamma spike follows the envelope obtained by the Fourier transform,

$$|E(\omega)|^2 \sim \left| \int (ct - x)^{1/3} e^{-i\omega t} dt \right|^2 \sim \frac{1}{\omega^{8/3}}. \quad (3.18)$$

From the full derivation, Baeva finds that each gamma spike contributes a spectral intensity

$$I_n \sim \frac{1}{n^{8/3}} \text{Ai}^2 \left( \frac{n^{2/3}}{N} \right), \quad (3.19)$$

where  $N = \alpha^{1/3} n_{\text{cr}}/2$ ,  $n_{\text{cr}} = 2/(1 - v_s)$ . For  $a_0 \gg 1$ ,  $n_{\text{cr}} \approx 2/(1 - (1 - 1/2\gamma_s^2)) = 4\gamma_s^2$ .

This is the roll-off from **OMM!**. The Airy-function is

$$\text{Ai}(x) = \frac{1}{\sqrt{\pi}} \int_0^\infty \cos \left( ux + \frac{1}{3} u^3 \right) du. \quad (3.20)$$

Equation 3.19 has two distinct regions. For  $n < N^{3/2} = \sqrt{8\alpha}\gamma_s^3 = n_c$  and

$$I_n \sim n^{-8/3}. \quad (3.21)$$

Above the cut-off, the spectrum decays exponentially.

Note that Equation 3.19 only accounts for the contribution from a single gamma spike. In general, the slow envelope of the spectrum is unchanged [166] but there can be destructive interference between spikes leading to modulations in the spectrum for specific harmonics. This can cause certain orders to vanish such as is the case for even order harmonics for s-polarised incident light [168]. This results from symmetries in the equations of motion [169].

### 3.2.2 The normalisation factor

Baeva's theory provides the relative intensity of harmonics. However, for comparison with the absolute spectral intensity of harmonics in the experiment, the normalisation factor is required. This can be calculated from conservation of energy. For arbitrary harmonic order scaling,  $n^{-p}$ , the spectral intensity of the harmonic beam is

$$I_\omega(\omega) = \frac{dE_\omega(J)}{dAd\omega} = I_0 \sum_{n=1, \text{ odd}}^{n_C} n^{-p} S_n \left( \frac{\omega}{\omega_L} - n \right) \quad (3.22)$$

up to the cut-off,  $n_C$ . Here  $S_n(\omega/\omega_L - n)$  is the spectral shape function of the  $n^{\text{th}}$  harmonic in reciprocal space and  $I_0$  is the normalisation factor of interest.

From conservation of energy,

$$\int I_\omega(\omega) d\omega dA = ER, \quad (3.23)$$

where  $E$  the total energy of the laser pulse and  $R$  is the reflectivity of the Relativistic Plasma Mirror (RPM). Intuition suggests the spectral shape function for the  $n^{\text{th}}$  harmonic retains the spectral shape of the incident laser pulse, *i.e.* for a laser pulse with a Gaussian temporal profile, this corresponds to a Gaussian centred at  $n\omega_L$  of width  $\sigma_L = 1/t_L$ , where  $t_L$  is the laser pulse width. Simulations show this is a reasonable approximation for ORION parameters <sup>1</sup>.

Simulations also show that for the SP1 laser, the incident laser pulse significantly suppresses the even harmonics, hence,

$$ER = \int_0^\infty I_0 \sum_{n=1, \text{ odd}}^{n_C} n^{-p} e^{-(\omega/\omega_L - n)^2/\sigma_L^2} d\omega. \quad (3.24)$$

The integral and summation order can be reversed. Since  $\sigma_L \ll \omega_L$ , all integrals in the summation are  $\approx \int_{-\infty}^\infty$  and therefore,

$$ER \approx I_0 \sum_{m=0}^{n_C/2-1} (1+2m)^{-p} \sqrt{\pi} \sigma_L \omega_L, \quad (3.25)$$

---

<sup>1</sup>Hole boring discussed in the following section can lead to a Doppler shift in harmonic energy across the laser pulse corresponding to a Doppler broadening of the spectral shape function in reciprocal space, however, unlike the ZVP simulations of the previous chapter, this is negligible for ORION parameters.

thus,

$$ER \approx I_0 \sqrt{\pi} \sigma_L \omega_L ((1 - 2^{-p}) \zeta(p) - 2^{-p} \zeta(p, \frac{n_C + 1}{2})), \quad (3.26)$$

where  $\zeta(p)$  and  $\zeta(p, (n_C + 1)/2)$  are the Riemann Zeta and Hurwitz Zeta functions respectively. The final term can be neglected for a petawatt class laser pulse where  $n_C \gg 1$ . In the case of an ideal  $p$ -polarised laser pulse,

$$ER \approx I_0 \sqrt{\pi} \sigma_L \omega_L \zeta(p). \quad (3.27)$$

For the Relativistic Oscillating Mirror (ROM) regime,  $p = 8/3$  and the RPM is extremely efficient,  $R \approx 1$ . Thus,  $I_0$  can be estimated from the system parameters.

### 3.2.3 Hole boring

As observed in the ZVP plots, on long timescales relative to the laser pulse cycles, via the ponderomotive pressure of the laser, the plasma front moves inwards. This is hole boring [124]. The velocity of hole boring can be derived by consideration of conservation of momentum in this quasi-static state. Since the hole boring velocity is laser pulse intensity dependent, the spatial profile of the laser will be imprinted on the surface. Typically Gaussian in shape, for high-power laser systems, this can to first order generate a focusing RPM and a beaming of the specularly reflected signal, as in Figure 3.1. To access the highest possible electromagnetic field intensities, the laser pulse is focused on target to the diffraction limit. However, since the diffraction limit scales linearly with the wavelength, higher-order harmonics can be refocused to a smaller spot via this mechanism allowing access to unprecedented peak intensities. Vincenti *et al* demonstrated intensity gains of over 1000 with currently accessible parameters in 3D PIC simulations [163], suggesting a realistic route to the Schwinger Limit using next-generation laser facilities. Regardless of any blue-skied pursuits, it is evident that any prediction of HHG beam intensity must account for hole boring and is therefore an essential component of the ORION experiment analysis.

Applying momentum balance between the laser pulse and particles in the rest frame of the RPM surface, the hole boring velocity is

$$\frac{v_{HB}}{c} = \sqrt{\frac{R \cos \theta}{2} \frac{Z m_e}{A m_p} \frac{n_c}{n_e(x_i(t, y))} a_L(t, y)} = \Pi a_L(t, y), \quad (3.28)$$

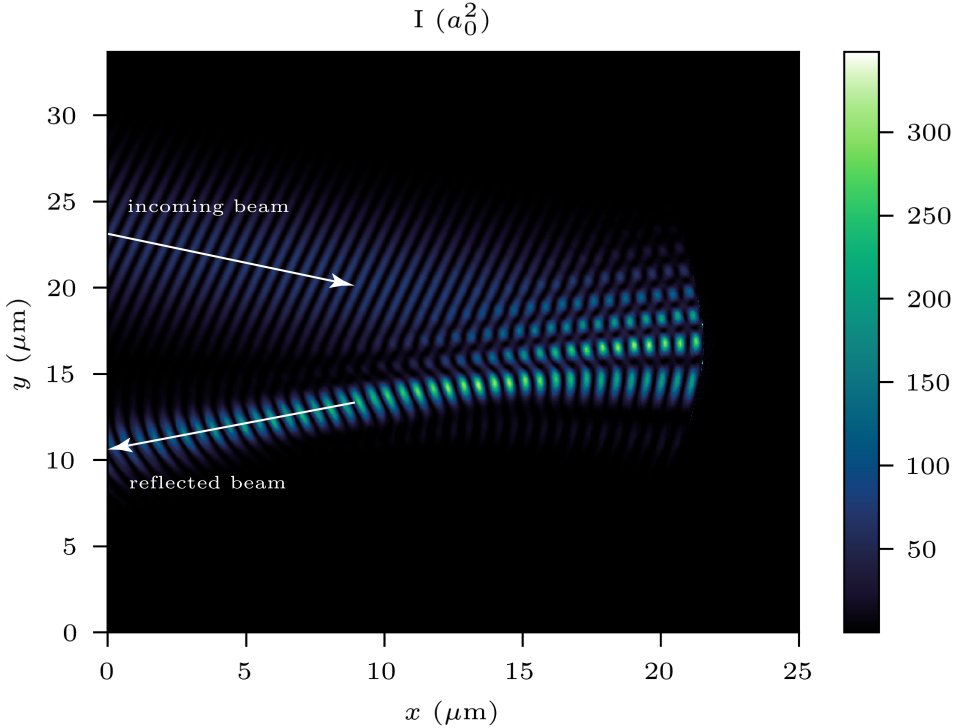


**Figure 3.1:** Electromagnetic field intensity in a 2D PIC simulation of a relativistic ( $a_0 = 30$ ) laser pulse incident on a solid density plasma. The incoming beam is specularly reflected off the target which is curved by the radiation pressure leading to beaming in the reflected harmonic beam.

where  $R$  is the RPM reflectivity,  $\theta$  is the angle of incidence,  $16^\circ$  in the ORION experiment,  $Z$  and  $A$  are the atomic and atomic mass numbers respectively for the plasma ions,  $n_c$  is the plasma critical density,  $n_e(x_i(t, y))$  the electron number density and  $x_i(t, y)$  the depth of hole boring, from the Supplementary Material [122]. For the ORION laser pulse parameter space  $\Pi \ll a_L \forall t$ , *i.e.* relativistic electrons and non-relativistic ions. Hence, the relativistic correction derived by Robinson *et al* [170] to Equation 3.28 can be neglected. Due to the high contrast and long duration of the ORION beamlines, there is minimal pre-plasma formation on the front surface and therefore the number density is simply the number density of the material in solid form and  $n_e$  is independent of  $x_i(t, y)$ . Robinson *et al* [171] generalised momentum conservation to multiple species. Replacing the mass density

with the composite mass density  $\rho = \sum_j m_{ij} n_{ij}$ , then

$$\frac{An_e}{Z} \rightarrow \sum_j \frac{A_j n_{ej}}{Z_j}, \quad (3.29)$$

where  $n_{ej}$  is the number density of electrons that originated from the  $j$  ion.

The spatiotemporal envelope of the normalised vector potential of the laser pulse incident on the target surface can be modelled as

$$a_L(t, y) = a_0 e^{-\frac{y^2}{2w_L^2}} g(t - t_0) \quad (3.30)$$

where  $w_L$  is the beam waist on target and  $g(t)$  the temporal envelope, typically a Gaussian or sech profile and  $t_0$  the main pulse peak time.

Integrating Equation 3.28,

$$x_i(y) = \int v_{HB} dt = \Pi \int_{-\infty}^t a_L(t, y) c dt. \quad (3.31)$$

At the peak of the main pulse,

$$x_i(y) = \Pi a_0 c e^{-\frac{y^2}{2w_L^2}} G, \quad (3.32)$$

where  $G = \int_{-\infty}^{t_0} g(t - t_0) dt \sim t_L$  and  $t_L$  is the laser pulse temporal width.

The total denting is a combination of the peak electron-ion charge separation,  $x_e$  (which leads to the intrinsic phase of the HHG beam [172]) and Equation 3.31. Note that for the long pulse duration of the ORION laser,  $x_i \gg x_e$  and therefore  $x_e$  can be neglected.

Applying a Taylor expansion to the spatial profile of Equation 3.31 around the laser spot centre,

$$x_i = \text{constant} - \frac{y^2}{4f_p} + \mathcal{O}(y^4), \quad (3.33)$$

where, to first order, this is the equation of a parabolic mirror with focal length

$$f_p(t) = \frac{w_L^2}{4\Pi a_0 c G}. \quad (3.34)$$

Following the Vincenti *et al* derivation [122], the denting parameter is defined as,

$$\delta_T = x_i|_{(y=0)} - x_i|_{(y=\sqrt{2}\omega_L)}. \quad (3.35)$$

Hence,

$$\delta_T = \frac{w_L^2}{2f_p} = 2\pi a_0 c G, \quad (3.36)$$

and is independent of laser focal spot size.

If the spatial profile of the  $n^{\text{th}}$  harmonic beam can be adequately described by a Gaussian at the plasma mirror plane, with a beam width described by the harmonic source size,  $w_n$ ,

$$h_n \sim e^{-r^2/w_n^2}, \quad (3.37)$$

then the beam profile is known at all distances,  $z$  from the target. Its divergence, defined as

$$\theta_n = \lim_{z \rightarrow \infty} \frac{w_n(z)}{z}, \quad (3.38)$$

is therefore

$$\theta_n = \theta_n^0 \sqrt{1 + \Psi_n^2}, \quad (3.39)$$

where  $\theta_n^0 = \lambda_n / \pi w_n$  is the harmonic divergence in the absence of RPM denting and

$$\Psi_n = \frac{2\pi}{\cos \theta} \left( \frac{w_n(0)}{w_L} \right)^2 \frac{\delta_T}{\lambda_n} \quad (3.40)$$

is the dimensionless focusing parameter. If  $\Psi_n \gg 1$ , as is true for the short wavelength X-ray harmonics of interest,

$$\theta_n \approx \frac{w_n(0)}{f_p \cos \theta} \quad (3.41)$$

and the divergence is dominated by RPM curvature.

Far from focus, at the detector plane a distance  $z$  from the target,

$$w_n \approx z \tan \theta_n. \quad (3.42)$$

The corresponding magnification factor at detection is thus

$$\gamma_n(z) = \frac{w_n(z)}{w_n(0)}, \quad (3.43)$$

thus the laser intensity at detection is reduced by a factor  $\gamma_n(z)^{-2}$ .

At large distances,

$$\gamma_n \approx \frac{z \tan(w_n(0)/(f_p \cos \theta))}{w_n(0)} \quad (3.44)$$

Taking the Taylor expansion of the tangent, one sees that the magnification factor is only weakly dependent on the harmonic source size ( $f_p$  is independent of the source size), whereas the magnification is strongly dependent on the laser spot size ( $\sim w_L^4$ ).

At the new RPM focal point,  $z = z_f$ , the demagnification factor is [122]

$$\gamma_n(z_f) = \frac{1}{\sqrt{1 + \Psi_n^2}}, \quad (3.45)$$

this determines the new peak intensity yielded by hole boring.

### 3.2.4 Harmonic source size

Include plots and fits for near roll-off.

### 3.2.5 The SHHG optimal parameter space

Interest in SHHG has prompted many numerical and experimental studies for the determination of its optimal parameters. The interaction efficiency increases with laser pulse intensity [126, 129] with a relativistic similarity parameter close to unity being preferable [120, 126]. The effective similarity parameter can be reduced with a finite preplasma scale length. The transverse coherence of the incident beam should be as good as possible to mitigate phase errors, this is best achieved with a diffraction-limited beam [**dromeyHighHarmonicGeneration2006**]. While HHG in transmission from thin foils is the optimum for currently accessible laser pulse intensities, HHG in reflection is more efficient for next-generation systems [130].

One might assume that target surface variation, root-mean-square roughness,  $\Delta s$ , need be less than the highest harmonic order that one wished to generate. However, Dromey *et al* demonstrated categorically in both experiment and simulation that surface roughness need only be less than the excursion amplitude of the oscillating electrons at the target front surface thus ensuring specular reflection and preventing scattering into the wings of the harmonic beam [175]. This is generally satisfied by

$\Delta s \ll \lambda_L$ . In their experiment, harmonics were visible provided  $\Delta s < \lambda_L/16$ . Note that furthermore preplasma expansion will lead to an increase in target smoothness before the main pulse arrival.

There is some debate regarding the angle of incidence with simulation parameter scans finding optima ranging from 45–62° [**thauryHighorderHarmonicAttosecond2010**, 120, 126]. However, all can agree that normal is not preferable. For ideal normal incidence odd harmonics are suppressed [168]. Even harmonics are suppressed for s-polarised incident light due to the symmetry of the interaction [71] while circularly polarised light significantly suppresses the entire mechanism [117]. This led to the suggestion of polarisation gating for the generation of isolated attosecond pulses [150].

Waveform tailoring with the inclusion of multiple laser wavelengths can improve HHG efficiency [**edwardsWaveformControlledRelativisticHighOrderHarmonic2016**]. Simulations have suggested the production of denser electron bunches and stronger acceleration for two colour pulses [**edwardsEnhancedAttosecondBursts2014**] and has been confirmed in experiment [38]. Interestingly the polarisations of the two colours must be identical, this is the inverse of HHG from gases.

High-power laser systems have inherent prepulses of ionising intensities. They will preheat a target leading to thermal expansion prior to the arrival of the main pulse, producing an exponential preplasma,  $n_e \sim e^{x/L}$ . HHG is exceedingly sensitive to this preplasma formation, evoking particular interest in the field [163, 173, 197–199]. While there is some variation in quoted optimal values, they are generally small relative to the laser wavelength, with scale lengths,  $L \approx 0.1\lambda_L$ . The difficulty in measuring such small lengths perhaps goes some of the way to explain the variety of suggested optima.

For  $L \leq 0.01\lambda_L$ , **CWE!** (**CWE!**) dominates over HHG. Kahaly *et al* demonstrated experimentally that harmonic emission varied smoothly from the CWE regime to the HHG regime to HHG suppression as the laser contrast was reduced [199]. Increasing the preplasma scale length increases the amplitude of surface oscillations, increasing HHG production. However, if the scale length is too large,

parametric instabilities in the underdense region begin to dominate and HHG is suppressed [173]. The use of 1D hydrodynamic codes to measure prepulses from laser contrast trace measurements has become standard practice [173, 197, 200]. Although, this shall be called into question in the following.

Fortunately, there are many approaches to control the various steps of preplasma generation. The heating effect of the prepulse can be reduced by reducing the angle of incidence or the prepulse itself can be reduced by reducing the intensity of the beam through apodisation or use of a frequency doubling crystal. A secondary beamline can generate a controllable prepulse [199], and the surface can be recompressed using a circularly polarised prepulse that will cause minimal heating [200].

Plasma mirrors are effective and now standardised tools for the improvement of laser contrast. These single-use optics initially have an **AR!** (**AR!**) coating of reflectivity  $R_1$ . As the incident laser fluence passes the damage threshold of the optic, plasma forms on the front surface. The optic is ‘switched on’ with a reflectivity  $R_2$ . The **PM!** (**PM!**) therefore improves the contrast by a factor  $R_2/R_1$ . There is a balancing act in choosing the peak intensity on the **PM!**. Too early and the PM will switch on before the arrival of the main pulse. Too low and switch on occurs too late and  $R_2$  is reduced. A peak intensity around  $1 \times 10^{16} \text{ W cm}^{-2}$  is best [201]. PMs act as a low-pass spatial filter, improving the quality of the focal spot on target [176].

### 3.3 Simulations

#### 3.3.1 1D PIC simulations of HHG

Numerical simulations of the SP1 and SP2 interactions with CVD and PMMA were performed using the Smilei PIC code to confirm the analytical results of Section 3.2 for ORION beamline parameters. Application of the Bourdier method (plasma initialised streaming at  $\mathbf{v} = c \sin \theta \hat{\mathbf{y}}$ ) enabled the computationally efficient simulation of the interactions in 1D, a necessity for the sub-ps ORION laser pulse duration. Even so, resolution, numerical heating and noise remain a serious problem for the accurate reconstruction of the physical phenomena despite the optimised supercomputer architecture. At least 10 cells per wavelength are necessary for

the highest resolved harmonic [126]. Incidentally, for X-ray harmonics, this is on the order of the Debye length for solid-density plasmas ( $T_e = 115$  eV,  $n_e(\text{CVD}) = 1.05 \times 10^{30} \text{ m}^{-3}$ ,  $\lambda_D = 7.8 \times 10^{-11} \text{ m}$ ,  $E_{n,\max} = 1.6 \text{ keV}$ ). For the simulation of only a single laser pulse cycle, Edwards and Mikhailova required up to 5000 particles per cell [126] to resolve X-ray harmonics above error from noise and numerical heating. Unfortunately, numerical heating scales linearly with time further increasing the computational cost for ORION timescales [104].

Thankfully, to make comparisons to the derivations of Section 3.2 only a low resolution is necessary. Simulation parameters are detailed in Table 3.1. Parameters are given in real units in the laboratory frame and normalised Smilei units in the boosted Bourdier frame. Note that polarisation angles and normalised vector potentials are unchanged by the frame transformation. The fourth interpolation order for the particle shape function was found to be an efficient choice for the minimisation of numerical heating for such low-resolution non-Debye length-resolving simulations.

Figure 3.2 presents typical simulation results for the SP1 laser geometry, SP2 parameters produced similar results. Figure 3.2a depicts ion density profile evolution via hole boring. While the density increases to several times its initial level near the plasma surface, this need not be accounted for in the hole boring calculation since additional ions accumulated near the surface have already acquired the necessary momentum and are simply co-propagating inwards with the surface. Figure 3.2b plainly exhibits the harmonic content of the specularly reflected beam with harmonics retaining the spectral shape of the incident beam. Even harmonics are significantly suppressed relative to odd harmonics. The bump in the distribution around the 18<sup>th</sup> harmonic is entirely spurious, a consequence of numerical heating. Increasing the simulation resolution shifts the bump to the right. Allowing for 10 cells per maximum harmonic wavelength, this distribution can only be trusted up to the 12<sup>th</sup> harmonic. It is here the signal begins to deviate. Undoubtedly, energy conservation does not hold for this simulation. However, it is still possible to extract  $I_0$ . Making the reasonable assumption that Debye heating does not affect

SP1 Laser (1D, 16° angle of incidence)		
Parameters	Real	Smilei
Wavelength, $\lambda$ (nm)	527	$2\pi$
Angular frequency, $\omega_L$ (fs $^{-1}$ )	3.58	1
Polarisation, $\phi$ (°)	-42.2	-42.2
Normalised vector potential, $a_0$	7 - 10	7 - 10
Temporal FWHM, $t_{FW}$ (fs)	470	1690
Temporal envelope, $E_t$	$E_t \sim e^{-(t-t_{FW})^2 \ln 2/t_{FW}^2}$	
SP2 Laser (1D, 16° angle of incidence)		
Parameters	Real	Smilei
Wavelength, $\lambda$ (nm)	1053	$2\pi$
Angular frequency, $\omega_L$ (fs $^{-1}$ )	1.79	1
Polarisation, $\phi$ (°)	19.6	19.6
Normalised vector potential, $a_0$	20 - 30	20 - 30
Temporal FWHM, $t_{FW}$ (fs)	470	843
Temporal envelope, $E_t$	$E_t \sim e^{-(t-t_{FW})^2 \ln 2/t_{FW}^2}$	
Simulation box		
Parameters	Real	Smilei
Size, $x$ (nm)	$10\lambda$	$20\pi$
Sim length, $T_{sim}$ (fs)	$2t_{FW} + 5\lambda/c$	
Spatial resolution, $\Delta x$ (nm)	$\lambda/128$	
Temporal resolution, $\Delta t$ (as)	$\Delta x/2c$	
Macro-electrons per cell	1000	
Macro-ions per cell	1000	
Ion temperature, $T_i$ (keV)	0	0
Electron temperature, $T_e$ (keV)	0.115	$2.25 \times 10^{-4}$
Collisionless, pre-ionised, regularly-initialised plasma		
Parameters	Real	Smilei
CVD density, $n_e$ (m $^{-3}$ )	$1.05 \times 10^{24}$	$\begin{cases} 294 \text{ for SP1} \\ 1175 \text{ for SP2} \end{cases}$
PMMA density, $n_e$ (m $^{-3}$ )	$3.90 \times 10^{23}$	$\begin{cases} 109 \text{ for SP1} \\ 435 \text{ for SP2} \end{cases}$
Electron $x$ profile, $n(x)$	$n_e$ for $\lambda \leq x \leq 9\lambda$	

**Table 3.1: Smilei parameters to compare Section 3.2 analytical results to numerical simulation for ORION parameter space.** Real parameters are taken in the laboratory frame with the given units, while Smilei parameters are in the boosted frame with normalised units. The CVD ion distribution consists of carbon ions with number density  $n/6$  while the PMMA ion distribution consists of carbon, oxygen and hydrogen ions with number densities  $1/6, 1/12, 1/12$  respectively, each with 1000 macroparticles per cell.

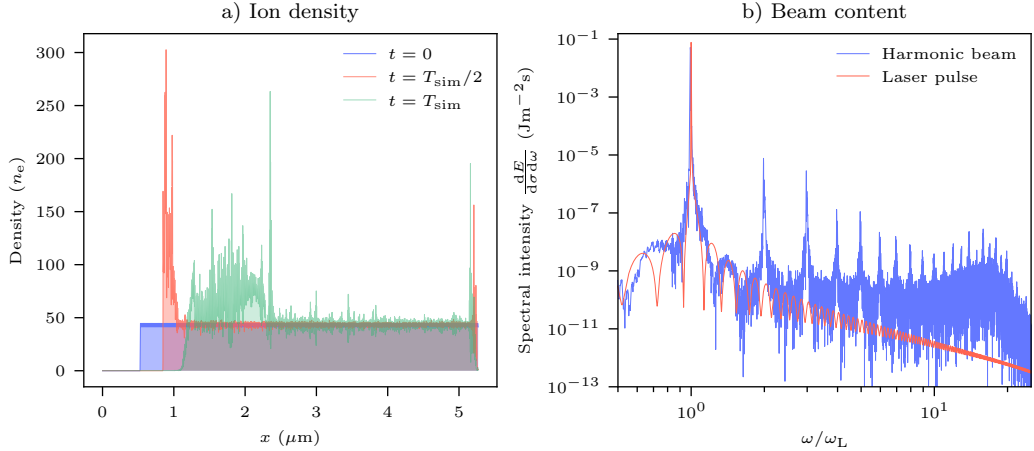
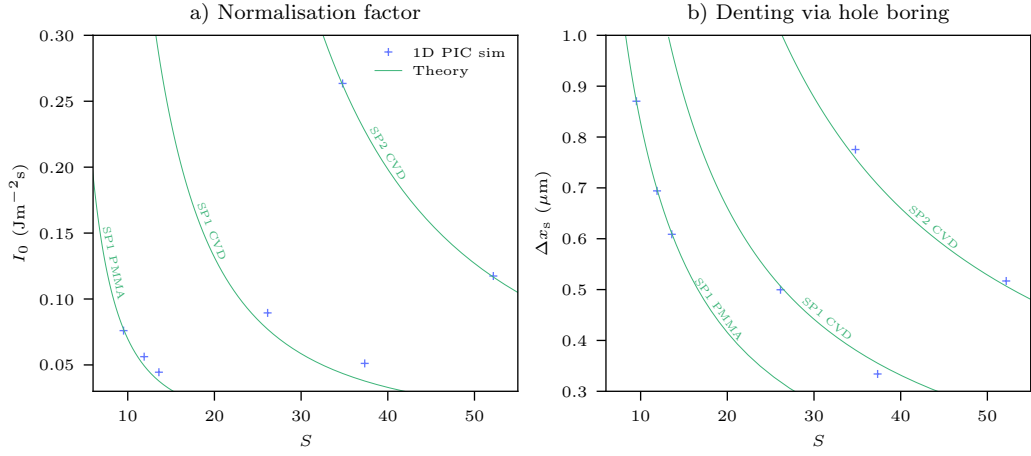


**Figure 3.2: 1D PIC simulation of the SP1 ORION beamline geometry at  $a_0 = 7$  interacting with a pre-ionised CVD target.** a) Ion density at initialisation ( $t = 0$ ), halfway ( $t = T_{\text{sim}}/2$ ) and at the simulation end ( $t = T_{\text{sim}}$ ) demonstrating hole boring. b) Absolute spectral intensity of the laser pulse and reflected harmonic beam obtained via Fourier transform. The harmonic beam retains the laser pulse spectral width. Even harmonics are significantly suppressed at this polarisation. The large bump in the distribution around the 18<sup>th</sup> harmonic is spuriously generated via numerical heating.

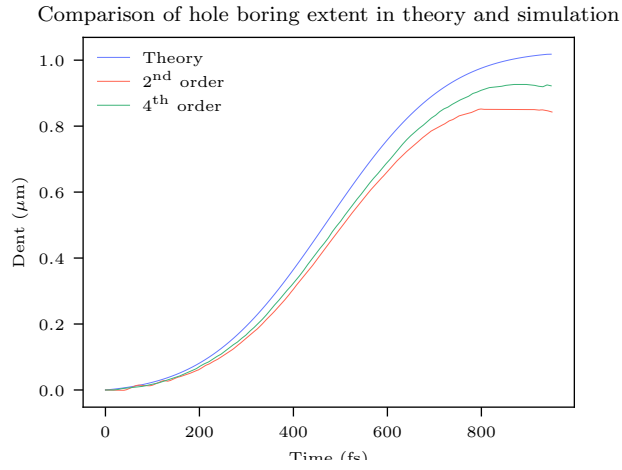
the HHG process and that the spectrum is simply the sum of the two contributions (justified by the observation of the continuation of harmonics over the bump in the distribution),  $I_0$  can simply be extracted as the peak intensity of the distribution corresponding to the intensity at  $\omega/\omega_L = 1$ ).

Figure 3.3 compares the analytically calculated parameters with those extracted from the simulations. There is remarkable agreement for the parameter space accessible with the ORION laser facility and the assumptions made in the analysis. The effect of numerical heating on the hole boring extent is illustrated by Figure 3.4 where the change in the surface position is plotted over time for the analytical calculation and PIC simulations with 2<sup>nd</sup> and 4<sup>th</sup> order shape function. The deviation from the theoretical prediction increases with time. Numerical heating leads to higher electron temperatures at the plasma surface and correspondingly a spurious preplasma expansion analogous to prepulse preplasma expansion. Artificially increasing the plasma temperature to increase the Debye length and reduce numerical heating, while improving HHG accuracy<sup>2</sup> reduces hole boring accuracy.

<sup>2</sup>Albeit up to a point, it is known that changes to the preplasma scale length can also affect HHG efficiency.



**Figure 3.3:** Comparison between simulation and analytical predictions of hole boring and HHG normalisation factor in the ORION laser facility parameter space for CVD and PMMA targets. a) The normalisation factor,  $I_0$ , where the spectral intensity,  $I = I_0 n^{-p}$  for low order harmonics. b) The depth of hole boring compared to the initialised plasma surface. Note that the steep density gradient as visible in Figure 3.2a ensures the surface position is well-defined. Both parameters are expressed in the laboratory frame.



**Figure 3.4:** The effect of the PIC code particle shape function on numerical heating demonstrated via the extent of hole boring. The deviation from the theoretical prediction increases with time, and the error decreases for increasing order of the shape function.

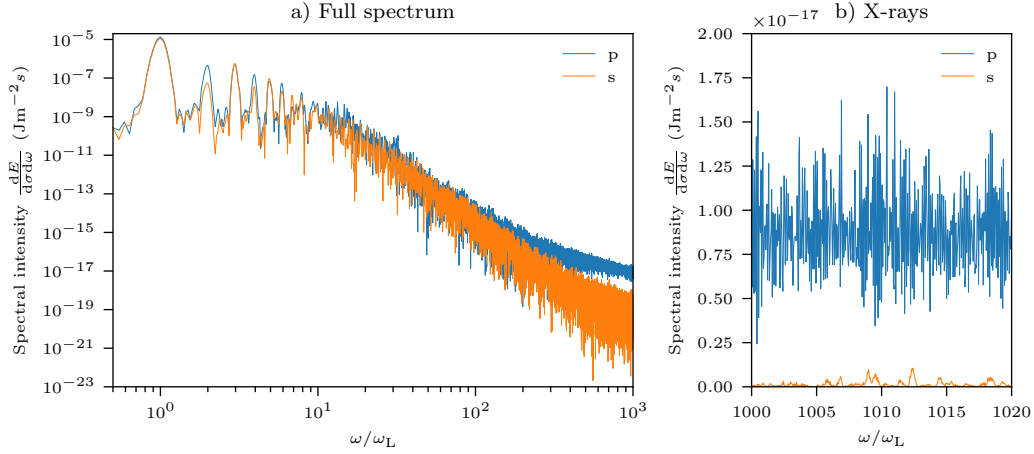


**Figure 3.5: Reflected beam harmonic content up to the keV range in a high-resolution 1D PIC simulation of a test pulse with SP1 ORION beam geometry incident on a CVD target.** The absolute spectral intensity is calculated from the Fourier transform of the reflected beam electric field. The s- and p-polarised components of the beam are analysed separately for both a) the full spectrum and b) the X-ray harmonics accessible with the OHREX quartz ( $10\bar{1}1$ ) crystal.

The X-ray harmonic spectrum produced from a CVD target irradiated by an SP1-type laser pulse is resolved in Figure 3.5. The simulation has 16384 cells per laser wavelength, the minimum multiple of 2 required to resolve the harmonics accessed with the OHREX quartz crystals. It was necessary to use a short test laser pulse with a  $5\lambda_L$  FWHM. The simulation time before the peak of the laser pulse was increased to reduce the error in the spectrum from unphysical hard cutoffs to the laser pulse profile. A steep preplasma scale length was applied to the plasma distribution of  $0.04\lambda_L$  to model the peak of the ORION pulse and suppress CWE!. At the X-ray intensities of Figure 3.5b, no harmonic structure is visible, indeed for the non-optimal ORION target chamber geometry, harmonics begin to merge from around the 20<sup>th</sup>. Note the s-polarised part of the reflected beam is over 50 times weaker than the p-polarised beam at the 1000<sup>th</sup> harmonic. It would be interesting to extract the reflected beam temporal profile after filtering sub-X-ray harmonics. This can be achieved by applying the inverse Fourier transform to the Fourier-transformed temporal profile with the lower-order harmonics removed. Unfortunately, beyond  $n = 50$ , noise overwhelms the signal of interest (from ROM theory, the X-ray harmonic intensity is at least 8 orders of magnitude below the laser

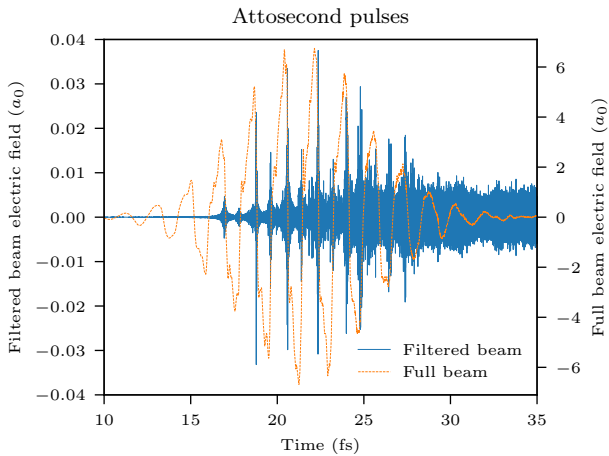


**Figure 3.6: Attosecond pulse train from the filtered reflected laser pulse.** The filtered beam contains only harmonics above  $n = 50$ .

pulse intensity). A substantially larger simulation would be required to produce the filtered signal. Figure 3.6 compares the reflected pulse structure to the reflected pulse structure with harmonics below  $n = 50$  removed. The filtered beam consists of a series of attosecond pulses of radiation, the brightest pulse is of duration 30.3 as. This is an order of magnitude above the duration of the X-ray pulse as predicted from the cut-off expression. Note that the intensity of the first few laser cycles is insufficient for the generation of harmonics above  $n = 50$  and there is therefore no signal here, effectively reducing the pulse train length.

### 3.3.2 Hydrodynamic simulations of preplasma formation

?? Following Dollar *et al* [173], hydrodynamic simulations of the ORION laser systems were performed using HYADES to confirm the suitability of the contrast conditions.

Simulations were performed in 1D planar geometry with a mesh of 511 evenly spaced points covering 20  $\mu\text{m}$  of the target (SiO<sub>2</sub>, PMMA, CVD, etc). Equation of state data was taken from the in-built HYADES data tables. For low temperatures and pressures, the data for the minimum value in the tables is used, for temperatures and pressures above the highest value in the tables, the values are linearly extrapolated from the highest value. Ionisation was calculated using the local

thermal equilibrium average atom model. Low temperature ( $T < 0.15\text{eV}$ ) values for the absorption and refractive indices of the target materials were input [178]. The threshold for laser energy absorption is set to  $1 \times 10^6 \text{ ergs cm}^{-2} = 0.1 \text{ W cm}^{-2}$ . Electrons and ions were initialised at a temperature  $1.551 \times 10^{-2} \text{ eV}$ . The real polarisation of the interaction cannot be treated using a 1D code since the electric field vector is rotated during propagation [**larsenQuestionSourceWave2023**]. Instead, simulations were performed in both s- and p-polarisation to provide some idea of the scale of the interaction.

No pre-ionisation or preplasma formation was observed in the simulations of the high-contrast SP1 laser pulse with any target material. This is in stark contrast with the SP2 laser, in the absence of a PM, the preplasma expansion of the targets is many orders larger than the laser pulse wavelength, necessitating the use of a PM and further HYADES simulations.

The distance between the PM and the main target is 15 mm, thus the beam diameter at the PM is  $\approx 15/(f/3) = 5 \text{ mm}$  and hence the intensity at the PM can be approximated. To account for variation around this approximation, simulations were performed with plausible high and low intensities.

First, the interaction between the SP2 and a  $\text{SiO}_2$  PM was simulated. Note that it is not possible to model the AR coating in hydrodynamic codes, instead it was assumed that the thin coating has minimal impact on the interaction. No ionisation was observed from the high-intensity laser prepulse starting from 10 ns out from the main pulse. Figure 3.7 plots the interaction between a low-intensity main pulse and the plasma mirror. Similar results were obtained for s- and p-polarisation. These simulations suggest ionisation begins at the start of the main pulse. There is some preplasma expansion and hole boring. The focusing effect of this hole boring is minimal for the large spot size on PM and can thus be ignored. The collisionless skin depth and plasma frequency can be calculated at each mesh point in the plasma from the electron density. The corresponding laser attenuation at each point is plotted in Figure 3.8 at the peak of the main pulse. The laser is

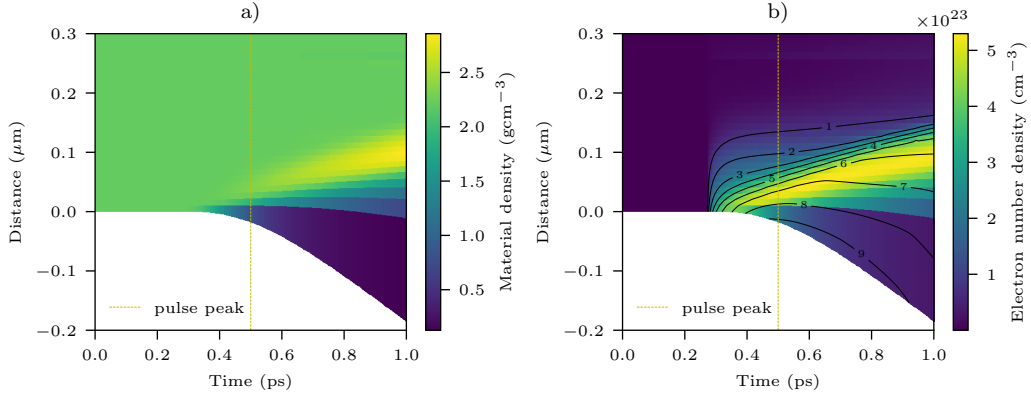


**Figure 3.7: Silicon dioxide plasma mirror switch on from irradiation by the SP2 main pulse at  $45^\circ$  angle of incidence and p-polarisation.** The laser pulse travels in the  $+\hat{x}$ -direction. The main pulse peak intensity is marked at 500 ps in the simulation. a) Material density as a function of time, a short preplasma is formed alongside hole boring. b) Electron number density as a function of time. The contours map the ionisation level.

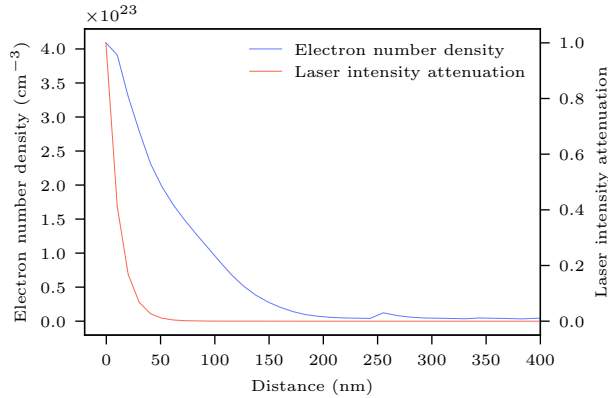


**Figure 3.8: The attenuation of the SP2 laser pulse is calculated as it propagates through a switched-on PM.**

rapidly attenuated and therefore switched on despite not attaining total ionisation at the front surface (at a cost to its reflectivity).

Satisfied that the PM operates as anticipated, a parameter scan of the targets was then conducted. Figure 3.9a describes the typical evolution of target density with the application of the SP2 prepulse, in this case after that prepulse has been attenuated by a plasma mirror with a reflectivity of 0.004. By the time of the main pulse arrival in this simulation, hole boring dominates over preplasma expansion. Indeed, the laser pulse intensity has already reached relativistic intensities a couple

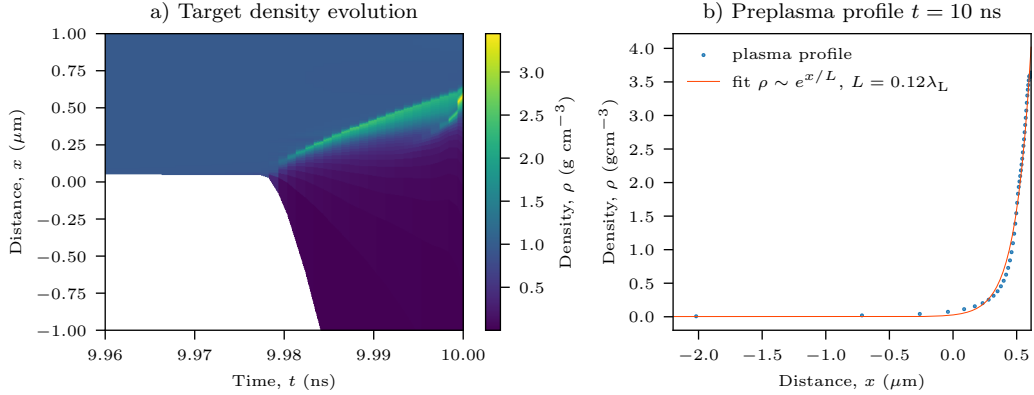


**Figure 3.9: Typical preplasma formation from the p-polarised  $16^\circ$  angle of incidence of the ORION SP2 laser prepulse on an HDPE target.** In this simulation the laser is modelled from 10 ns before the main pulse with  $a_0 = 30$  and attenuated by a PM of reflectivity 0.004. a) Typical preplasma expansion elucidated via target density. By the time of the main pulse, hole boring is dominant over plasma expansion. b) An exponential fit ( $\rho \sim e^{x/L}$ ) for the preplasma scale length,  $L$ , at the time of arrival of the main pulse. For this simulation the optimum fit is  $L = 0.12\lambda_L$ .

of picoseconds out from the main interaction. Figure 3.9b includes an exponential fit to obtain the corresponding close to optimal preplasma scale length of  $L = 0.12\lambda_L$  at the time of arrival of the SP2 main pulse.

Figure 3.10 repeats the analysis of 3.9 for a variety of target materials, reflectivities, polarisations and laser intensities. The s-polarised light simulations follow a clear trend: increasing incident laser energy leads to an increased scale length up to a transition point that will be determined by the point at which hole boring overcomes plasma expansion. This will depend on the interplay of target ion density, ionisation potential and heating. Interestingly, the trend is much less consistent for p-polarised light. It is known that heating increases for p-polarised light as there is now a component of the laser pulse electric field acting into the plasma, however, the crossing of the high and low intensities suggests a dynamic balance between hole boring and plasma heating. Regardless, the change in scale length is not significant at these PM reflectivities. Unfortunately, it was not possible to conduct a similar parameter scan for the CVD targets, it would appear that the EOS tables for such a target material are not suited for this interaction type, the two tables offered provided inconsistent and unphysical results with specific

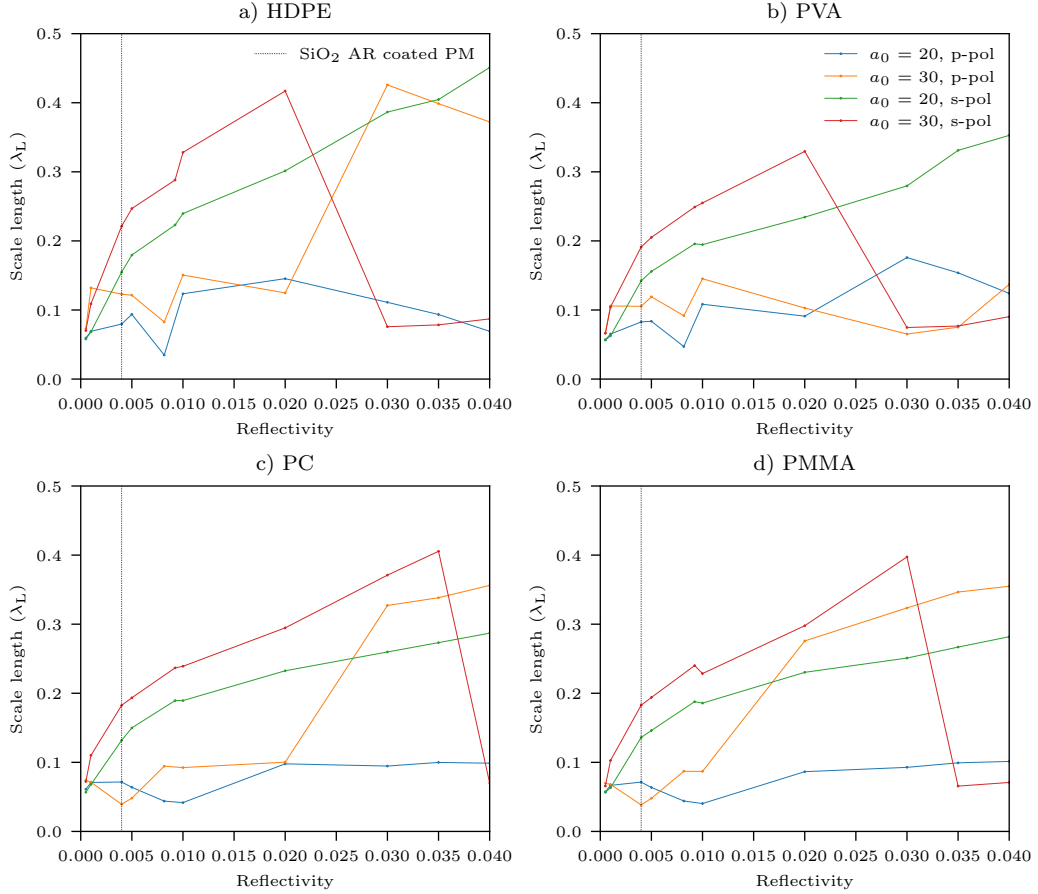


**Figure 3.10: Preplasma scale length parameter scan for a variety of plastic targets.** Target materials are a) HDPE, b) PVA, c) PC and d) PMMA. The dashed line highlights the reflectivity of the  $\text{SiO}_2$  AR-coated PM for the SP2 wavelength. The preplasma scale length remains small for the range of parameters explored.

simulations crashing at random. However, one can assume that the preplasma scale lengths of irradiated CVD targets would be lower than those established in Figure 3.10 due to the high damage threshold of the material.

It is interesting to return to the question of temperature raised with regards to the initialisation of PIC code main pulse simulations as presented in Chapter ???. Figure 3.11 plots the plasma electron temperature from 40 ps before the main pulse arrives. Once plasma expansion initiates the extent of heating rapidly diverges across the preplasma and bulk. Evidently, it does not make sense to define a temperature for a system not in equilibrium. Indeed, there is no standardised practice within the field and yet temperature can have a significant effect such as

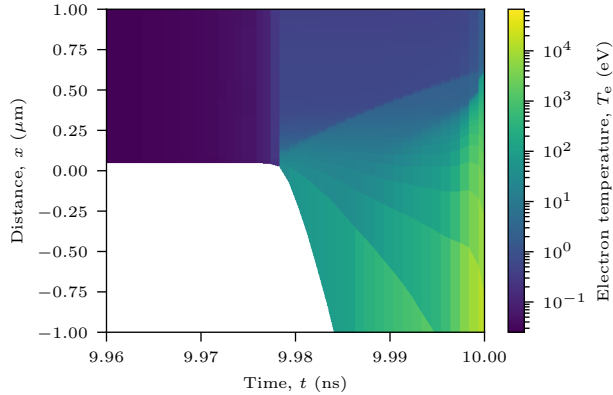


**Figure 3.11:** The typical electron temperature of a plastic target after irradiation by a petawatt class laser prepulse. This is the same simulation as presented in Figure 3.9. Namely, an  $a_0 = 30$  p-polarised laser pulse attenuated by a plasma mirror of reflectivity 0.004 incident on an HDPE target at  $16^\circ$ . The bulk and preplasma temperatures differ by multiple orders of magnitude.

has already been seen in simulations on hole boring. There is also some experimental evidence to say HHG efficiency scales inversely with plasma temperature [199].

Plasma temperature is highly sensitive to the precise experimental conditions. At the time of the main pulse arrival at the plasma surface (as defined by the peak of the electron density distribution), the temperature is 112 eV, consistent with the value chosen for PIC simulations. Hydrodynamic codes are unsuitable for the prediction of the plasma temperature increase induced by the main pulse interaction given the high non-linearity of the dynamics in this regime that could not be adequately captured by such a code.

## 3.4 The experiment

The two experimental goals were to resolve and measure the absolute intensity of X-ray harmonics produced with the ORION SP2 beamline. After debris from the plasma mirror optic damaged the parabola it was necessary to switch to the higher contrast but lower energy SP1 beamline and only after the experiment was it established that it was not possible to resolve X-ray harmonics with the ORION target chamber geometry. However, absolute intensities were measured for both

the SP1 and SP2 beamlines and for CVD and PMMA targets. ORION short pulse beamline parameters are provided in Figure 1.3

The experimental design is relatively straightforward. CAD drawings of the experimental setup are presented in Figure 3.12. The laser was focused onto the target at **TCC!** (**TCC!**) with the ORION High Resolution X-ray (OHREX) spectrometer positioned along the specular reflection direction. Additional X-ray pinhole diagnostics monitored the spot size. The SP2 beamline reflects off an additional **PM!** optic at  $45^\circ$  **AOI!** (**AOI!**) to improve the laser prepulse contrast. Then both the SP1 and SP2 beamlines arrive at **TCC!** along the same axis.

Both the non-linear HHG interaction and the linear OHREX crystal spectrometer are sensitive to the polarisation of incident light. It is therefore important to track the polarisations of the beamlines as they propagate through the system.

The ORION target chamber has its own defined geometry with the target located at the origin (**TCC!**), sketched in Figure 3.13. The polarisation angles are  $\phi_1 = 11.8^\circ$  and  $\phi_2 = 16.4^\circ$ . Following the reflection of the SP2 beam off the plasma mirror, both the SP1 and SP2 beamlines propagate in the  $-\hat{\mathbf{x}}$ -direction towards the origin. The OHREX crystal is located at

$$\mathbf{r}_{\text{OHREX}} = r_0(\cos B \cos A, -\cos B \sin A, \sin B), \quad (3.46)$$

where  $r_0 = 2.4\text{ m}$ ,  $A = 26.82^\circ$  and  $B = 18.15^\circ$ , setting the rotation angle of the target. This was achieved using the ORION Multi-Target-Mounts. Alignment was performed offline by Dr Ed Gumbrell and no further details will be provided here on that process. As in Figure 3.12e, the OHREX spectrometer sits on the outside of the target chamber tilted an angle  $18^\circ$  to the vertical.

The interaction plane is defined by the vector

$$\mathbf{n} = \frac{\mathbf{r}_{\text{OHREX}}}{r_0} \times \hat{\mathbf{x}} = (0, \sin B, \cos B \sin A). \quad (3.47)$$

The cosine rule can be applied to determine the polarisation of the laser pulses in the interaction plane, for polarisation vector  $\hat{\mathbf{E}}$ ,

$$\frac{\mathbf{n}}{|\mathbf{n}|} \cdot \hat{\mathbf{E}} = \cos \theta, \quad (3.48)$$

### 3.4. The experiment

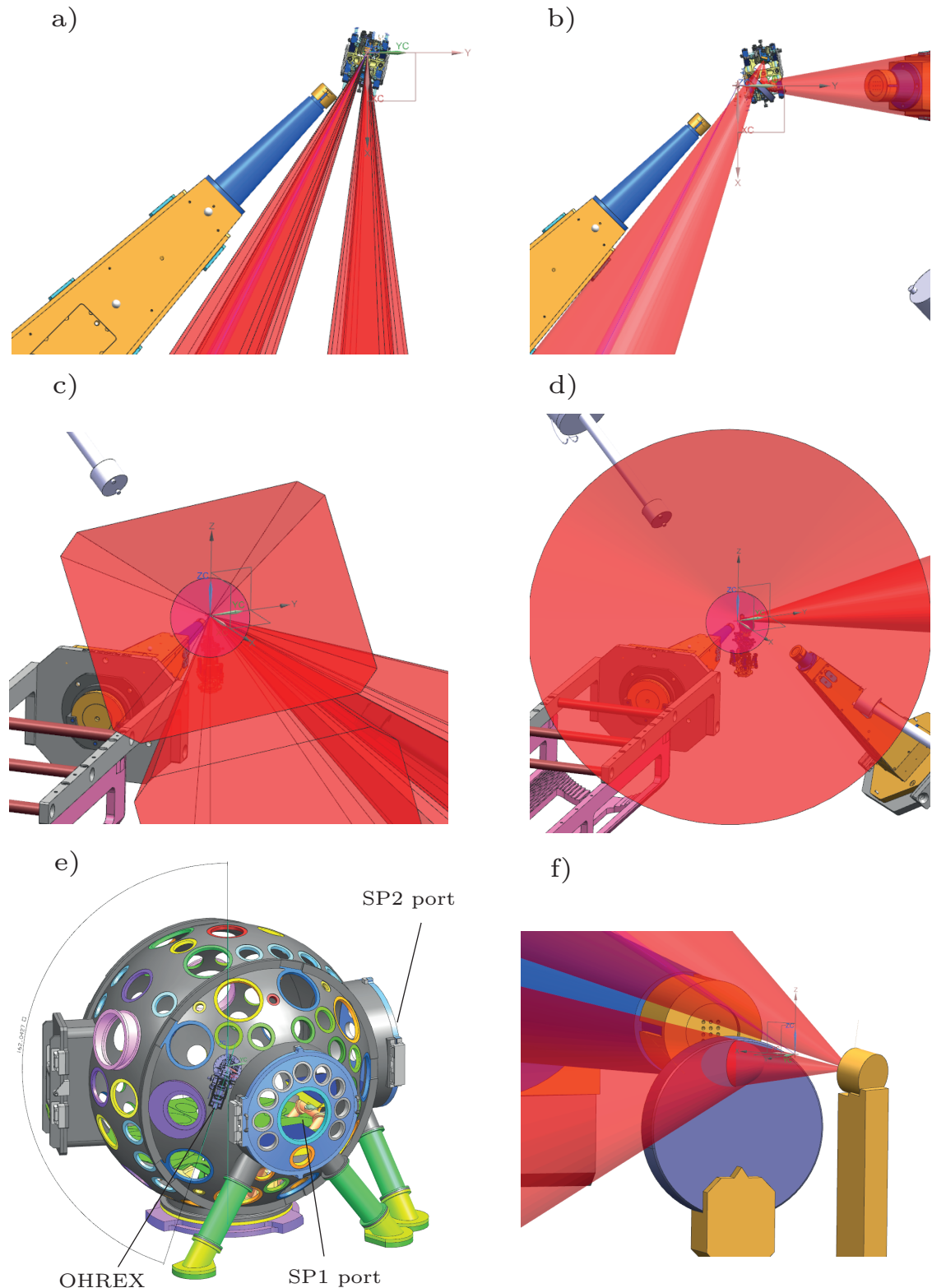


**Figure 3.12:** CAD images of the ORION target chamber set up for this experiment. a) and b) SP1 and SP2 beamlines respectively from parabola to TCC to OHREX spectrometer. c) and d) SP1 and SP2 beamlines respectively looking from OHREX to TCC. e) Annotated ORION target chamber model. f) SP2 beamline reflecting off plasma mirror before main target incidence.

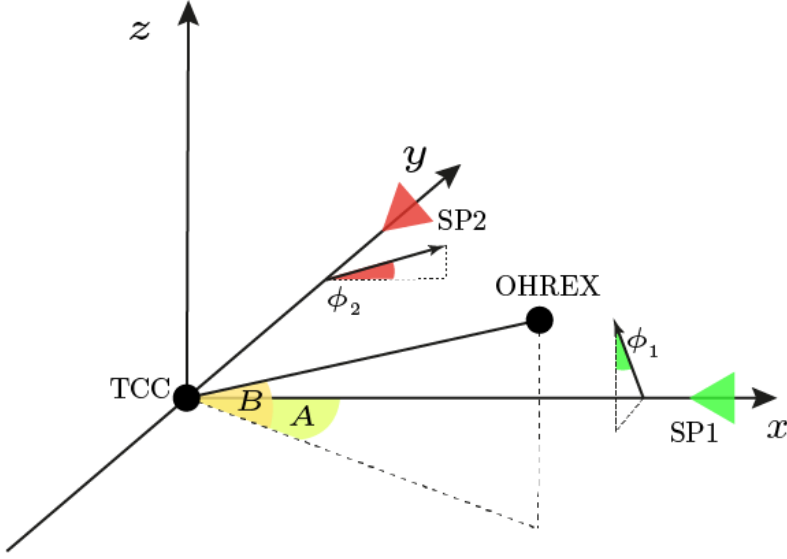


**Figure 3.13:** ORION target chamber geometry with the location of the target, OHREX spectrometer and the SP1 (green) and SP2 (infra-red) beamlines and their corresponding polarisations,  $\phi_1 = 11.8^\circ$  and  $\phi_2 = 16.4^\circ$ .

where  $\theta$  defines the angle between the polarisation vector and the vector normal to the interaction plane. This corresponds to angles out of the interaction plane of  $42.2^\circ$  for the SP1 beam (rotating anticlockwise out of the interaction plane when looking from TCC to parabola) and  $19.6^\circ$  for the SP2 beam (rotating clockwise out of the interaction plane when looking from TCC to parabola). Again applying the cosine rule, the angle of incidence is  $16^\circ$ .

The polarisation vector can then be split into s- and p-polarised components. The s-polarised component remains unchanged by the interaction but the p-polarised component must be rotated, its direction along  $\mathbf{n} \times \mathbf{r}_{\text{OHREX}}$ . Figure 3.5 illustrates the suppression of the s-polarised component at the X-ray photon energies of interest. This component is therefore neglected.

The OHREX spectrometer sits flat on the target chamber wall but rotated an angle  $C = 18^\circ$  to the vertical. The OHREX interaction plane is correspondingly rotated. Again, applying the cross-product, the OHREX interaction plane is

$$\mathbf{n}_O = [-\cos(A)\sin(B)\sin(C) - \sin(A)\cos(B)\cos(C), -\cos(A)\cos(B)\cos(C) + \sin(A)\sin(B)\sin(C)]$$
(3.49)

**Figure 3.14: ORION experiment 3D scans of target roughness.** a) CVD with roughness  $\Delta s = 4 \text{ nm}$  and  $S \approx 26, 35$  for SP1 and SP2 beamlines respectively. b) PMMA with roughness  $\Delta s = 11.2 \text{ nm}$  and  $S \approx 10, 13$  for SP1 and SP2 beamlines respectively.

Applying the cosine rule between the p-polarised vector and  $\mathbf{n}_O$ , the angle of the polarisation vector of the harmonic beam out of the plane of the OHREX interaction is  $77.23^\circ$  for both SP1 and SP2.

### 3.4.1 Targets

Specialised target holders were designed and built by the AWE and CLF target fabrication teams. These hold the targets at the required angle out of the horizontal plane with an additional fiducial wire for alignment. Targets were mounted on the ORION Multi-Target-Mount and alignment was performed offline by Dr Ed Gumbrell.

There are multiple considerations when it comes to target density. In practice accessing the  $S \approx 1$  regime is not possible using a petawatt class laser system with even the lowest density solid plastic targets. However, the 2007 Vulcan experiment successfully reproduced the  $8/3$  scaling up to the X-ray regime for  $S \approx 50$  [161] despite simulations repeatedly emphasising the improvement of harmonic efficiency for reduced similarity parameter. At the same time, as discussed in Section 3.2, target hole boring leads to an increased harmonic beam divergence. High electron density targets are perhaps therefore more suited to the petawatt class laser system thereby maintaining the beaming of harmonics.

The surface roughness of a selection of low-density plastic targets was analysed by the CLF target fabrication team leading to the choice of PMMA plastic targets. CVD targets were also selected, having the highest ionisation potential (and therefore lowest susceptibility to laser prepulse) of solids that can be polished optically flat albeit at a higher  $S$  parameter. Scans performed by AWE and CLF of the target surfaces are given in Figure 3.14.

### 3.4.2 Contrast and plasma mirrors

As illustrated in Figure 3.12, a plasma mirror optic is included before the main target to improve the contrast of the SP2 beamline [176]. HYADES simulations of the effect of this optic are detailed in Section ???. The distance between the PM and the main target is 15 mm, thus the beam diameter at the PM is  $\approx 15/(f/3) = 5$  mm and the intensity on PM can be calculated. Provided the harmonic beam divergence is less than or equal to the  $f/3$  cone, as is anticipated, the harmonic beam should not be clipped by the PM in this setup.

The intention was to use **AR!**-coated fused silica optimised for  $45^\circ$  **AOI!** and the SP2 pulse wavelength (BCP45R) [177]. This has a reflectance of 0.398 % at  $\lambda_L = 1053$  nm for unpolarised light. Unfortunately, the debris from the PM caused damage to the parabola. For the second SP2 shot, the high reflectivity fused silica PM was replaced with a thin foil of silicon nitride. The reduction in available material of the thin foil reduces the risk of damaging debris. At  $45^\circ$  **AOI!**,  $\lambda = 1.053 \mu\text{m}$  and  $\phi_2 = 16.4^\circ$ , the silicon nitride PM pre-switch-on has a reflectivity of 5.55 % [178]. One can assume its behaviour after switch-on is consistent with the other PM since it is simply a plasma interaction now.

### 3.4.3 KBRXM

The ORION SP1 and SP2 spot size was routinely monitored on shot by the AWE laser team via two X-ray pinhole cameras and the time-integrating Kirkpatrick-Baez X-ray microscope (KBXRM) diagnostic, sat on the target chamber Port 21 and pointed at the notional **TCC!**. This reflective X-ray microscope optic has a ten times magnification and spatial resolution of  $15 \mu\text{m}$ , comfortably resolving the laser spot size. Images were again recorded with TR-type IP. Direct mapping between the recorded images and real laser irradiance profiles is a highly non-trivial problem with any proposed model depending strongly on the assumptions made. However, by making the very reasonable assumption of spatial and temporal blurring of the spot size in the X-ray image due to electron transport away from the laser spot, the measured spot size will be an upper bound on the real spot

size. It follows that the upper bound on optical spot widths corresponds to a lower limit of irradiance (since the on-shot energy is well-defined). These diagnostics determine sensible upper bounds for the laser spot size are  $20\text{ }\mu\text{m}$  and  $10\text{ }\mu\text{m}$  for the SP1 and SP2 beamlines respectively.

## 3.5 Experimental data processing

### 3.5.1 Image plate calibration

Image plates (IPs) are reusable recording media that detect ionising radiation and are particularly suitable for the detection of X-rays produced in laser-plasma interactions. Their response is well understood and their sensitivities to a wide spectrum of photon energies have been absolutely calibrated on the ORION facility [179]. Albeit for the FLA3000 scanner, not the FLA7000 used in this experiment. However, the deviation in response is negligible for the photon energies measured. In this experiment, the Fuji Biological Analysis System (BAS) TR-type IPs were used. They have a phosphor layer composed of  $\text{BaFBr}_{0.085}\text{I}_{0.15}$  with density  $2.61\text{ g cm}^{-3}$  and thickness  $60\text{ }\mu\text{m}$  but no mylar layer. This makes them suitable for low-energy X-ray detection. When scanned, the IP releases blue photons via photostimulated luminescence (PSL), which are then collected by a photomultiplier tube. The PSL value is generalised across scanner types from the measured ‘Grey’ ( $G$ ) value by

$$\text{PSL} = (0.23284G^2 \times 10^{-9}) \left( \frac{\Delta x}{100} \right)^2 W \times 10^{-L/2}, \quad (3.50)$$

where  $\Delta x$  is the scanner resolution ( $= 25\text{ }\mu\text{m}$  in this experiment),  $L$  is the latitude parameter, and

$$W = 0.092906 + 1370.8e^{-0.014874V} + 654.24e^{-0.011026}, \quad (3.51)$$

where  $V$  is the scanner voltage [180].

IP photon sensitivity,  $\psi$ , the number of PSLs per incident photon, is dependent on photon energy. Meadowcroft *et al* modelled this as,

$$\psi_j = \eta(m_j h\nu + c_j), \quad (3.52)$$

where  $h\nu$  is the photon energy and  $m_j$  and  $c_j$  are linear fit parameters valid for specific energy ranges,  $j$ . For the Fuji BAS TR-type IP and X-rays in the range 0-6.0 keV,  $m_j = 0.54(5)$  mPSL keV $^{-1}$  and  $c_j = 0.020(2)$  mPSL. The IP absorption efficiency in mPSL per photon is

$$\eta(h\nu, T_i, T_s) = \exp(-n_i \Phi_i(h\nu) T_i) [1 - \exp(-n_s \Phi_s(h\nu) T_s)], \quad (3.53)$$

where  $n$  is the layer density,  $\Phi(h\nu)$  is the total cross-section of the layer,  $T$  the effective layer thickness, s and i correspond to the sensitive (phosphor) and insensitive (mylar) layers of the IP respectively [181]. The first term is neglected in the absence of an insensitive (mylar) layer in TR-type IP. Below 50 keV, the dominant mode for X-ray absorption into the IP is the photo-electric effect, where

$$\Phi_{ph} \approx 3 \times 10^{12} \frac{Z^4}{(h\nu)^{3.5}} \quad (3.54)$$

and  $Z$  is the atomic number [182] and  $\Phi_{ph}$  is given in units of Barn per atom. At 2.4 keV, that corresponds to a sensitivity of 1.32 mPSL per incident photon.

It is generally inevitable that some time will elapse between the laser shot and the IP scan. For this experiment, 30 minutes was typical, in which time some fading of the IP occurs that must be accounted for. IP fading can be modelled as an attenuation factor,

$$F(t) = A \exp(-t/\tau) + B, \quad (3.55)$$

where  $t$  is the time between shot and scan and  $A$ ,  $\tau$  and  $B$  are found from fits to experimental data. A key aspect of the exponential decay is that the attenuation depends only on the signal at that moment in time and not the initial conditions. This has been shown to be true in experiment [179].

At 20 °C at the ORION facility, *Meadowcroft et al* [179] determined that for the Fuji BAS TR-type IP, the optimum fit for the parameters of Equation 3.55 is  $A = 0.347(22)$ ,  $B = 0.693(11)$  and  $\tau = 35.5(53)$  minutes. Therefore at 30 minutes,  $F(t) = 0.84$ .

In summary, the number of PSL measured on an IP can be converted to an incident number of photons via

$$N(h\nu) = \frac{\text{PSL}}{F(t)} \frac{10^3}{\psi(h\nu)} = P(h\nu)\text{PSL}. \quad (3.56)$$

### 3.5.2 OHREX calibration

The Orion High REsolution X-ray (OHREX) spectrometer, housed on the ORION laser target chamber outer wall, utilises a spherically bent crystal geometry to spatially focus and spectrally analyse photons from the target chamber [183] with a high signal-to-noise ratio. The measured signal has been absolutely calibrated for a range of energies using a variety of crystals [184]. The OHREX spectrometer can hold two crystals at a time. At each crystal's spatial focal plane, a two-dimensional image is formed, one dimension is spatial, the other spectral. The energy range accessed by a given crystal is determined by the crystal rotation but all OHREX crystals are designed for operation at a nominal central Bragg angle of  $\theta_B = 51.3^\circ$  with the corresponding wavelength determined from Bragg's Law,  $n\lambda = 2d \sin \theta_B$ , for the appropriate crystal plane. The range around that central photon energy is determined by the crystal width in the spectral dimension.

MacDonald *et al* determined a quadratic fit for each crystal's dispersion relation to connect position along the image to photon energy [184]. Unfortunately in this experiment, the image lengths varied from those in the previous experiment, a likely consequence of slight defocusing of the optic. Note that the OHREX geometry is designed such that precise focus is not necessary to achieve good results [183].

Instead, a simple linear dispersion relation based on the known maximum and minimum energies accessed by the crystal was applied across the crystal images, a reasonable approximation to the dispersion relation determined by MacDonald *et al* [184] (the quadratic correction is small). The energy ranges for the three lowest energy OHREX crystals are given in table 3.2.

Provided full illumination of the  $6\text{ cm} \times 4\text{ cm}$  crystal, the spatial dimension can be safely integrated over to calculate the measured signal,  $M(h\nu)$  in  $\text{J mm}^{-1}$  and remove uncertainty from the IP drifting from the ideal focal plane. (In this

Crystal	Range, $n = 1$ (eV)	Range, $n = 2$ (eV)
KAP (100)	585-625	1170-1245
Quartz (10̄10)	1830-1950	3660-3900
Quartz (10̄11)	2330-2480	4660-4960

**Table 3.2:** Photon energy ranges captured by the three lowest energy OHREX crystals when operating at their nominal central Bragg angle of 51.3 or first and second diffraction orders,  $n$ .

experiment we assume that the harmonic beam width at the crystal position is larger than the size of the crystal, a reasonable assumption since beam divergence  $\approx 10^\circ$  and the 6 cm x 4 cm crystal sits 2.4 m from the target.). This corresponds to a source spectral intensity incident on the crystal  $S(h\nu)$  measured in  $\text{J keV}^{-1} \text{ sr}^{-1}$  via the spectrometer response,  $G(h\nu)$ , explicitly,

$$M(h\nu) = S(h\nu)G(h\nu). \quad (3.57)$$

The absolute throughput of the crystals was measured by MacDonald *et al* in a previous ORION experiment and fit parameters for

$$G(h\nu) = A(h\nu)^2 + B(h\nu) + C, \quad (3.58)$$

where  $(h\nu)$  is the photon energy measured in eV, determined for both p- and s-polarised incident light and for first and second diffraction orders [184]. The parameters for the lowest few energy crystals are presented in Table 3.3. There is unfortunately no spectrometer response data for the 10̄10 crystal to first order due to the Si K edge sitting within the energy range and the dramatic effect this has on absorption in its vicinity [185].

The OHREX is equipped with a 50  $\mu\text{m}$  Beryllium filter to protect the crystals. The corresponding signal attenuation can be calculated using X-ray transmission data [186].

### 3.5.3 Extracting the data

The quartz OHREX crystals 10̄10 and 10̄11 were fielded on the experiment. Crystal images were recorded with BasTR2040 Fuji Image Plate. A typical shot image

Crystal	Order	Polarisation	<i>A</i>	<i>B</i>	<i>C</i>
KAP (100)	1	s	$1.72 \times 10^{-15}$	$-4.69 \times 10^{-12}$	$2.89 \times 10^{-9}$
		p	$1.40 \times 10^{-14}$	$-1.74 \times 10^{-11}$	$5.42 \times 10^{-9}$
	2	s	$3.64 \times 10^{-16}$	$-9.64 \times 10^{-13}$	$6.95 \times 10^{-10}$
		p	$5.03 \times 10^{-10}$	$8.09 \times 10^{-13}$	$5.03 \times 10^{-10}$
Quartz (10̄10)	1	s	...	...	...
		p	...	...	...
	2	s	$4.50 \times 10^{-15}$	$-3.40 \times 10^{-11}$	$6.52 \times 10^{-8}$
		p	$1.13 \times 10^{-15}$	$-8.86 \times 10^{-12}$	$1.73 \times 10^{-8}$
Quartz (10̄11)	1	s	$1.00 \times 10^{-16}$	$-1.74 \times 10^{-12}$	$4.93 \times 10^{-9}$
		p	$2.78 \times 10^{-15}$	$-1.41 \times 10^{-11}$	$1.79 \times 10^{-8}$
	2	s	$4.70 \times 10^{-16}$	$-4.50 \times 10^{-12}$	$1.11 \times 10^{-8}$
		p	$2.10 \times 10^{-16}$	$2.11 \times 10^{-12}$	$5.30 \times 10^{-9}$

**Table 3.3:** Sensitivity fit parameters as a function of photon energy,  $h\nu$  in electron-volts ( $G(h\nu) = A(h\nu)^2 + B(h\nu) + C$ ) for the three lowest energy OHREX crystals for p- and s-polarised incident photons and first and second diffraction orders [184]. Note that no data is available for the first order of the quartz (10̄10) crystal.

**Figure 3.15:** Unprocessed shot data from a FLA7000 scanned image plate converted to PSLs. The image plate and two crystal images are clearly visible.

scanned with the FLA7000 scanner and converted to photostimulated luminescence units (PSLs) is given in Figure 3.15. The average background signal was subtracted. The *x*- and *y*-axes were converted from pixels to mm using the scanner resolution, ( $25\text{ }\mu\text{m px}^{-1}$ ) and then energies using the appropriate dispersion relations. The data was then integrated over *y* to obtain the intensity in units of  $\text{PSL mm}^{-1}$  across each crystal image. Then the corresponding source signal is

$$S(h\nu)[\text{J keV}^{-1} \text{sr}^{-1}] = \frac{d\text{PSL}}{dx} \frac{P(h\nu)}{G(h\nu)} h\nu, \quad (3.59)$$

which can then be converted to a measured spectral intensity per harmonic at distance  $r = 1$  from the source, ready to be directly compared to the theory,

$$I_{\text{n}}^{\text{meas}}|_{(r=1\text{ m})} = S(h\nu) \frac{dh\nu(\text{keV})}{dn}. \quad (3.60)$$

No sensitivity data is available for the 10̄10 quartz crystal, instead, this lower energy crystal was fielded to attempt resolving of the X-ray harmonics. At the

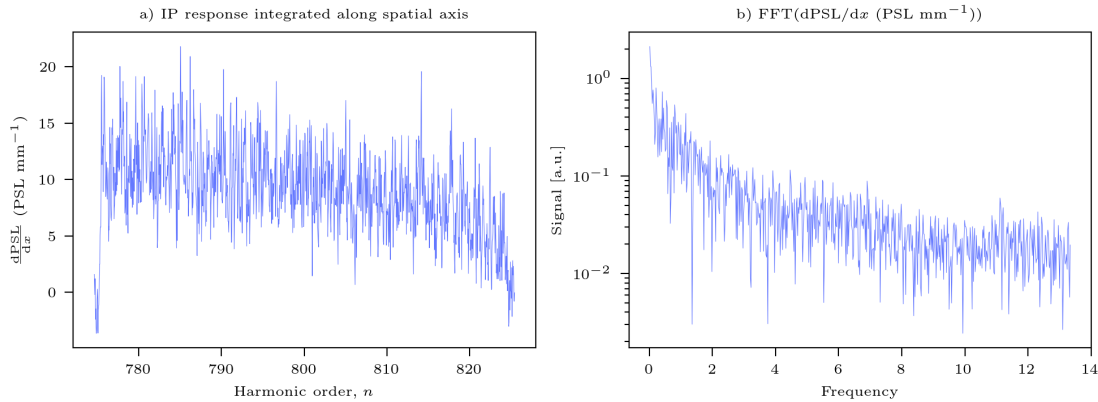


**Figure 3.16: Typical (SP1, PMMA) uncalibrated shot data for the quartz (10\bar{1}0) image** a) IP spatial axis integrated signal with dispersion axis. b) Fourier transform of a) with no evidence of harmonics.

experiment planning stage, it was unknown if this would be possible. Now that the simulations have been performed, we know that the non-optimal ORION target chamber geometry leads to the merging of the harmonics even before the water window at 282 eV. This is consistent with the findings, Figure 3.16 is a typical integrated signal in PSL mm and the corresponding Fourier transform for the quartz (10\bar{1}0) crystal image.

### Calibration and polarisation

The choice of the spectrometer response function,  $G(h\nu)$ , is non-trivial. One must first be assured that the second-order contribution is small relative to the first, true for this source spectrum. And also think carefully about the anticipated polarisation in the OHREX interaction plane. The OHREX response to p-polarised light is approximately an order of magnitude lower than for s-polarised light. From Figure X we are assured that only the p-polarised (with respect to the target interaction plane) X-rays are specularly reflected to the OHREX. The corresponding polarisation out of the OHREX interaction plane is calculated in the Appendix. The polarisation of the HHG beam relative to the OHREX plane of incidence and reflection is 10.5° out of the plane. Unlike the RPM interaction, the OHREX crystal reflection is an entirely linear process and it is therefore acceptable to decompose the laser pulse

into its constituents, explicitly, the field incident on the crystal is

$$\mathbf{E}_O = \mathbf{E}_{O,s} + \mathbf{E}_{O,p}. \quad (3.61)$$

After interaction with the crystal, the field is

$$\mathbf{E}_{\text{detector}} = \alpha_s(h\nu)\mathbf{E}_{O,s} + \alpha_p(h\nu)\mathbf{E}_{O,p}, \quad (3.62)$$

where  $\alpha_i(h\nu)$  is the energy-dependent ( $h\nu$ ) amplitude sensitivity of the reflection for s- and p-polarised respectively. Since the two polarisations are orthogonal, the intensity is

$$I = \alpha_s^2(h\nu)|\mathbf{E}_{O,s}|^2 + \alpha_p^2(h\nu)|\mathbf{E}_{O,p}|^2. \quad (3.63)$$

Noting that  $\alpha_i^2(h\nu)$  are the calibration factors,  $G_i(h\nu)$ , and that

$$|\mathbf{E}_{O,s}| = |\mathbf{E}_O| \sin \phi \quad (3.64)$$

and

$$|\mathbf{E}_{O,p}| = |\mathbf{E}_O| \cos \phi, \quad (3.65)$$

where  $\phi$  is the angle out of the interaction plane,

$$I_{\text{detector}} = (G_s(h\nu) \sin^2 \phi + G_p(h\nu) \cos^2 \phi) |\mathbf{E}_O|^2 = F(h\nu) |\mathbf{E}_O|^2, \quad (3.66)$$

where  $F(h\nu) = (G_s(h\nu) \sin^2 \phi + G_p(h\nu) \cos^2 \phi)$  is the energy-dependent calibration factor for this OHREX orientation.

## 3.6 Experimental results

Figure 3.17 is a typical calibrated signal from the quartz (10̄11) crystal, ready for comparison to the theoretical prediction. For each shot the mean signal across the dispersion axis was calculated and the errors from statistics, the fade time (11 %), the IP sensitivity (1.5 %), the dispersion axis (2.9 %) and the OHREX crystal reflectivity (11 %) accounted for.

As demonstrated in Section 3.2, the intensity of X-ray harmonics is highly sensitive to the intensity of individual pulse cycles due to the proximity of the

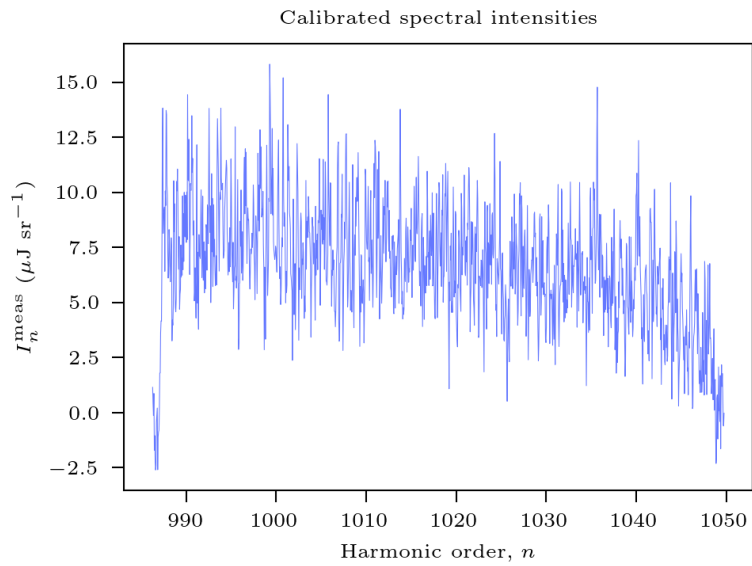


**Figure 3.17:** Typical (SP1, PMMA) ORION experiment calibrated IP response for the quartz (10̄11) crystal.

measurement to the exponential roll-off in the spectrum. However, even neglecting the shot-to-shot variation, it is not possible to know the precise sub-cycle spatio-temporal structure of a petawatt-class laser pulse. Indeed, the simple measurement of the peak intensity of such a pulse remains an open problem [187, 188]. Instead, we must rely on our assumptions and approximations, that is that the SP1 and SP2 beamlines can be adequately described by spatial Gaussians and temporal  $\text{sech}^2$  and  $\text{sech}$  profiles respectively, and that the duration and energy are well defined. The tight focused laser spot is subject to jitter on a shot-to-shot basis. This was routinely monitored via a KBRXM diagnostic that measures X-ray emission from the target. The spot measured by this diagnostic will always be larger than the actual laser pulse focal spot due to the energy transport of electrons moving away from the interaction area. This upper limit on laser pulse spot size corresponds to a lower limit on laser pulse intensity and therefore also of HHG efficiency. Figure 3.18 plots HHG spectral intensity curves for the quartz (10̄11) crystal central energy as a function of laser spot size for the targets and laser pulse configurations explored in the experiment. The thick lines range from the upper limits of spot size as measured by the KBRXM diagnostic to the spot area being halved. The spectral intensity of the harmonic

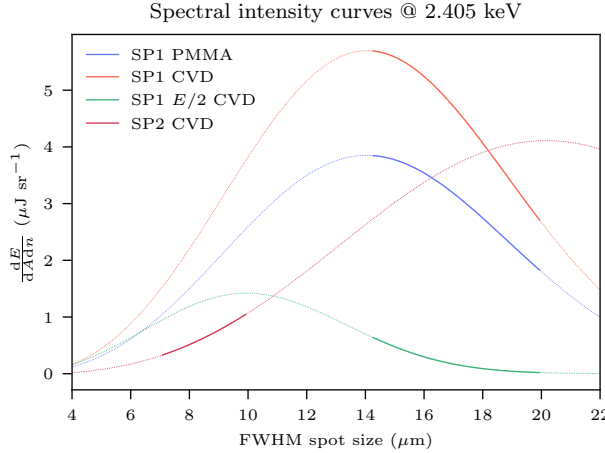


**Figure 3.18: Dependence of the harmonic beam spectral intensity on laser spot size at 2.405 keV.** Targets and beamlines relevant to the experiment are plotted. The half-energy single beamlet SP1 laser is demarcated by  $E/2$ . The thick lines indicate likely values for the laser spot sizes in this experiment. The SP1 harmonic beams are strongly affected by the exponential roll-off, unlike the SP2 beamline.

beam from the SP1 beamline sits in a delicate balance between beam divergence via hole boring and the exponential roll-off. Note that only the roll-off leads to a reduction in the total energy contained within the harmonic beam. The strong non-linearity of the interaction leads to the single beamlet SP1 beamline producing a harmonic beam over 6 times weaker than the double beamlet configuration. Interestingly, the higher intensity of the SP2 beamline leads to a greater divergence and a lower spectral intensity of the harmonic beam than for the SP1 laser pulse.

Figure 3.19 plots the experimental results with comparison to theory and simulation. Experimental data points are consistent within their errors with one another, the theory and the simulation, albeit with large uncertainties with such a low shot number. Significantly, the SP2 beamline is on average almost 6 times brighter than the SP1 beamline despite the greater energy content and greater component of the laser pulse electric field directed into the plasma for the SP2 beamline while the single beamlet shot is over 7 times weaker in intensity compared to the mean intensity of the full SP2 beamline. These highly non-linear (with respect to energy) scalings are consistent with HHG theory but cannot be understood as originating from bremsstrahlung lending huge credibility to these results. Bremsstrahlung

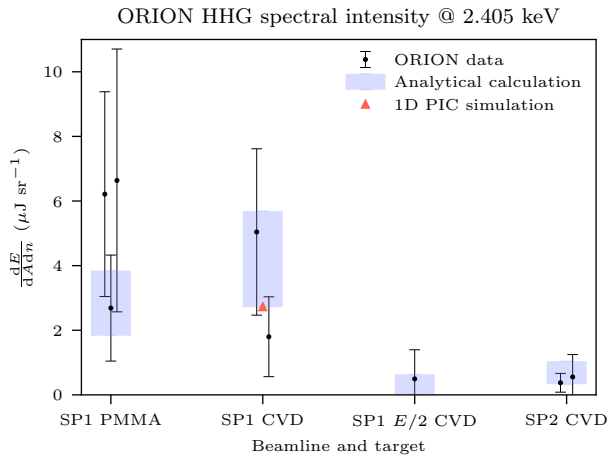


**Figure 3.19: X-ray harmonic spectral intensities at 2.405 keV measured on the ORION experiment compared to theory and simulation.** The analytical calculation corresponds to the thick lines marked in Figure 3.18. The 1D PIC simulation result is derived from Figure 3.5 and scaled to the ORION laser pulse duration.

emission scales sub-linearly with temperature and temperature scales sub-linearly with energy on target. The total energy is well-constrained and this is far more relevant for Bremsstrahlung than the uncertain intensity (dependent on the variable spot size). Thus, at the best-case scenario, one could anticipate twice the intensity being observed for the double beamlet SP2 compared to the single.

Bremsstrahlung emission from steep density profile low-Z solid density targets irradiated by relativistic laser pulses remains an area of active research with experiments to explore this in the planning stages at the University of York. However, provided a few assumptions it is possible to derive approximate best-case scenario scalings of spectral intensity with incident energy. First, assume that energy absorption into the plasma target does not increase with increasing energy. From Equation the plasma temperature scales linearly with the incident energy. Now, assuming the target can be treated as a radiating black body, the Equation increases most rapidly with temperature when  $h\nu \ll k_B T$  at which point the spectral radiance scales linearly with temperature. Thus, in the best case, we could expect a linear increase in the spectral intensity measured from the double beamlet compared to the single if that signal originated from Bremsstrahlung emission. Note further that this scaling depends not on the incident intensity but only on

the incident energy which is a well-constrained quantity on ORION, *i.e.* we do not anticipate significant shot-to-shot variation.

The above discussion relied on the assumptions of equilibrium and a black-body radiation spectrum. While this is valid for the long radiating period after the interaction, in much of this thesis, emphasis has been placed on the non-equilibrium state of the interaction itself. There are two species of relevance during this time: the hot electrons around the front surface directly heated by the laser pulse and prepulse, and the hot electrons that are reflected specularly and are responsible for the HHG. In [189], bremsstrahlung of these species is measured experimentally for a 30 fs laser pulse and  $a_0 = 2.8$ . As the populations of each of these species are so small, the peak contribution to the photon spectrum is many orders of magnitude smaller than that of the experimental signal and can therefore be neglected.

These findings are highly significant. Then write up the new peak intensity and the efficiencies. Comment on flying focus

## 3.7 Summary

This chapter has described in full the experimental methods and results of the recent ORION experiment. The X-ray harmonic intensities were measured using the OHREX spectrometer. Finding X and X. To describe the results, the ROM model of SHHG was laid out, combining all pieces of the puzzle to reconstruct the measured intensities analytically. The experimental campaign was supported by PIC and hydrodynamic simulations of the main pulse and prepulse interactions respectively. PIC simulations agree with the analytical results for the ORION parameter space. No preplasma expansion was observed for the SP1 beamline and reasonable preplasma scale lengths for the SP2 beamline provided the use of a single PM optic. Some discussion of plasma temperature was provided.

SUMMARY of the X-ray harmonic beam produced: include efficiencies, include duration

ADD MOST EFFICIENT HHG CONDITIONS SECTION - 30 mins - done  
Go through the HYADES section - 30 mins - done Harmonic source size - 30

mins Finish off discussion of results - 30 mins Summarise findings of the chapter, including presentation of the result in context - 30 mins misc stuff to main body  
- 30 mins HYADES outline - 30 mins

Tomorrow: assess state of TODOs, check sims



# 4

## Attosecond electron bunches and X-ray pulses on GEMINI PW

### Contents

---

4.1	Overview	115
4.2	X-ray harmonics on GEMINI PW	117
4.3	Observation of ZVP electron bunches	119
4.4	Application of HHG to white light Laue diffraction	123
4.5	Contrast	124
4.5.1	Contrast on GEMINI PW	124
4.5.2	Kahaly mirror	128
4.6	Beyond GEMINI PW	129

---

### 4.1 Overview

The intensity of the attosecond duration X-ray harmonics on the ORION SP1 and SP2 beamlines has been measured. even so, the uncertainties remained large, the geometry sub-optimal and the pulse train exceedingly far from an isolated attosecond pulse. Indeed, none of the proposed mechanisms for isolation (polarisation gating, lighthouse technique, etc.) could have any hope of success. The high shot rate, few femtosecond, highly customisable GEMINI PW facility at CLF can address all points while also providing conditions suitable for the production of attosecond ZVP

electron bunches discussed in Chapter 2. Naturally, attended by its own suite of technical challenges. The prior chapters of this thesis formed the body of a proposal for five weeks of beam time at the facility with shot dates planned for June 2024. This chapter outlines the extensive planning process for that experiment.

There are three primary experimental goals. First, to repeat the ORION experiment on GEMINI PW with optimised geometry and thus resolve and measure the absolute intensity of X-ray harmonics, detailed in Section 4.2. Second, to observe ZVP electron bunches in transmission while simultaneously measuring the HHG signal they generate in reflection, detailed in Section 4.3. Finally, the application of the X-ray harmonic beam in a proof of principle white light Laue diffraction setting is described in Section 4.4. Section 4.5 addresses the subject of laser contrast, a much thornier issue for the few femtosecond GEMINI beamline compared to ORION and covers the parallel experiment proposed by collaborators at Queen’s University Belfast to provide some illumination to the problem at hand. Note that no petawatt class sub-100 femtosecond laser facility has observed harmonics at oblique incidence. This section will also detail the strategy of contingency should the contrast prove to be too poor for the production of harmonics. Not discussed in this chapter is the work undertaken by Elliot Denis to perform spectro-spatial encoding and thus temporally resolve chirped harmonic beams.

CAD drawings overview where to put you?

The experimental geometry is relatively simple. Post **DPM!** (**DPM!**) contrast enhancement<sup>1</sup>, the GEMINI PW South (S) beam is focused by an  $f/2$  parabola onto the solid density target at  $45^\circ$  **AOI!** and p-polarisation, directing the specularly reflected harmonic beam to the West side of the chamber and the XUV and X-ray spectrometers.

---

<sup>1</sup>A previous experiment measured the GEMINI DPM setup produced a reduction in peak pulse intensity of 50 % but improved the contrast by 5 orders of magnitude. More details on the DPM system are given in Section 4.5.

## 4.2 X-ray harmonics on GEMINI PW

Naturally, the first action is to repeat the ORION experiment at GEMINI PW. For this purpose, the Oxford Engineering Department is designing and building a replica OHREX spectrometer to resolve and measure the absolute intensity of X-ray harmonics with OHREX crystals on loan from ORION. The lower energy KAP (100) OHREX crystal listed in Table 3.2 is more suited to GEMINI PW due to the lower energy of the beamline compared to ORION. Regardless, the quartz crystals will also be fielded.

A 1D PIC simulation of the GEMINI PW beamline for the planned geometry predicts harmonics will be resolved for the KAP energy range. [INSERT PIC SIMS HERE].

A parameter scan of **XHHG!** (**XHHG!**) as a function of  $S$  can be performed by varying the laser intensity, via beam apodisation, and the target material. The majority of shots will use target wheels of the relatively high damage threshold fused silica with the plan to advance to a Kapton tape. The fused silica targets are chemically etched in one corner to aid alignment. Since HHG is suppressed for circularly polarised light, bremsstrahlung emission and other X-ray production mechanisms can somewhat be ruled out by comparing the **XHHG!** signal observed for p- and circularly- polarised light, produced via a quarter wave plate. At 45° **AOI!**, however, this suppression is not total. And, the efficiency of heating is also reduced, reducing the signal from bremsstrahlung.

The OHREX spectrometer design is such that its technical complexity is entirely bound to the spherically bent OHREX crystals, thus reducing the challenges of alignment [183] and replica building. It is relatively insensitive to the distances between source and crystal (2.4 m) and from crystal to image plane (0.524 m). Indeed, previous experiments deemed unnecessary the adjustment of the bellows to bring the detector to the best focal plane. Variation in the angle of incidence from 38.7° shifts the spectral image away from the nominal energy range. The alignment of the spherically bent crystal planes to the crystal surface enables the relative

convenience of optical alignment. A light source placed at the target location produces a line focus on some tissue paper placed at the focal plane.

Filtering is necessary to reject the high-intensity low-order harmonics, however, for photon energies in the 600 eV range accessed by the KAP crystal, the standard beryllium filter transmission is too low. 400 nm of aluminium flash-coated onto 1 micron of mylar is more suitable, corresponding to a transmission of 16 % at 600 eV [186]. Light leakage and alignment will be checked with IP before switching to the Raptor Photonics Eagle XV in vacuum X-ray CCD camera (EA4240XV-BN-CL) [190] to utilise the high shot rate on GEMINI PW. Note that with  $2048 \times 2048$  active pixels of size  $13.5 \mu\text{m} \times 13.5 \mu\text{m}$ , not all of the 4 cm crystal image can be captured by the camera. The CCD camera must be liquid-cooled. For the prevention of damaging condensation on the camera window, a manual gate valve is required to isolate the OHREX when pumping the main chamber (waiting for the camera to reach acceptable temperatures while under vacuum would be prohibitively long).

It is essential to check there is the required resolution in both the spectrometer and the CCD camera for harmonic observation. For the highest energy crystal, nominal photon energy of 2.405 keV, 96 harmonics sit in the range accessed by the crystal, corresponding to a fractional energy  $\Delta E/E = 6.45 \times 10^{-4}$  between harmonics. At  $\Delta E/E = 1 \times 10^{-4}$ , the OHREX crystal resolution is sufficient. Characterising the spectral shape of the harmonics at such energies is probably beyond the capability of such a detector. Those 96 harmonics are spread over the 4 cm crystal image. At a resolution of  $13.5 \mu\text{m}$ , the CCD camera has 31 pixels between harmonics and the harmonic width is about a pixel.

sims: Running a new SiO<sub>2</sub> HHG sim, hopefully, will show that we have a better efficiency than the previous simulation. Then pop that in here.

Signals at the detector can be predicted using the theory of Chapter 3 using GEMINI PW parameters. Applying ROM and hole boring theory to a fused silica target and accounting for filtering and assuming no merging of harmonics, one can anticipate signals at the OHREX crystal position of  $19.6 \mu\text{J sr}^{-1}$  per harmonic at 0.6 keV for the KAP crystal and  $1.89 \mu\text{J sr}^{-1}$  per harmonic at 2.405 keV for the

quartz (10\bar{1}1) crystal. Orienting the OHREX for s-polarisation, to maximise the signal at the image plane, corresponds to an average of 3.4 photons per pixel and 0.20 photons per pixel respectively. The quantum efficiency of the detector is close to 100 %. These photon numbers are no less than those measured in the ORION experiment while the background will be lower due to the order of magnitude lower energy on target. Implying adequate statistics for the observation of such signals.

### 4.3 Observation of ZVP electron bunches

The second stage of the GEMINI PW experiment is the first observation of ZVP electron bunches both mass-limited and bulk-produced. There has been some experimental evidence of attosecond and nano-Coulomb electron bunch generation from nano-targets [110, 114] and in reflection from solids [113, 115] with the latter demonstrating satisfaction of the specific conditions for **VLA!** (**VLA!**) to 10 MeV for a mildly relativistic laser pulse ( $a_0 \approx 3.1$ ). These experiments have guided the planning process for this experiment stage.

This experiment aspires to produce mass-limited ZVP electron bunches in the configuration simulated in Figure 4.1. Emitted electron bunch energies are maximised by focusing the 2 micron laser spot onto the corner of a transversely mass-limited target. The simulations suggest it is possible to simultaneously measure the specularly reflected HHG and the attosecond ZVP electron bunches that produce it. Note via equations 2.47 and 2.26, the low-density target of Figure 4.1 are a more practical choice for the experiment relative to the aluminium targets of predominant use in Chapter 2, producing larger and more energetic bunches. Both bulk and mass-limited ZVP electron bunches will be generated. Via conservation of transverse momentum, the two species will be spatially separated at the observation point with bulk bunches at lower energies, experiencing no further acceleration phases post ZVP.

While normal incidence was most convenient for the initial ZVP simulations, oblique incidence is more optimal for HHG [120, 126] and as can be understood from equations 2.43 and 2.44, the new energy scaling expressions, for the ZVP mechanism. Not only is oblique preferable but it is essential to mitigate damage to

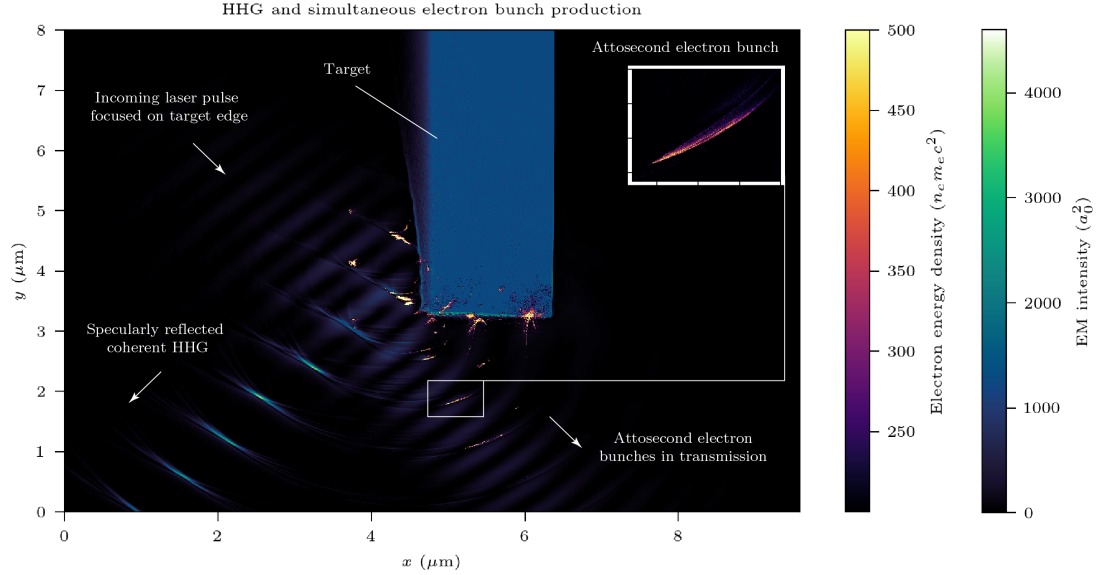


**Figure 4.1:** A simulation of the planned GEMINI-PW experimental setup for the measurement of ZVP electron bunches. This novel setup enables the simultaneous measurement of attosecond ZVP electron bunches and their coherent emission of X-ray light. The GEMINI-PW laser pulse is incident at  $45^\circ$  on the low-density polyethylene target with a preplasma scale length of  $0.2\lambda_L$ . For this angle of incidence, transmitted bunches and specularly reflected X-ray harmonics are produced at a frequency of  $\omega_L$ .

**Figure 4.2: Targets designed for observation of ZVP electron bunches.** a) Target array design with conical array holder and tapered finger, lengths in mm. b) Scan of the etched wafer, striations develop towards target rear due to etching technique. c) A 3D plot of surface variation. Scalloping and striations are visible but too small to interfere with laser pulse transmission at  $45^\circ$ . d) Lineouts of c), the  $y$ -profile is along the target edge of interest.

the laser optics via back-reflection. The HHG beam intensity at the focus can be over 1000 times that of the incident laser pulse [164]. It is necessary to conduct PIC code parameter scans for this new geometry.

High target edge precision is essential for the generation of attosecond duration ZVP electron bunches. The CLF Target Fabrication team has created  $300 \mu\text{m}$  silicon wafer targets via the Bosch process with well-defined edges of sub-micron precision. The target design is presented in Figure ??a. The tapered finger structure adds a failure point to mitigate damage to adjacent targets via shock propagation. The cone of the array holder is of sufficient size for the full laser pulse to access the target edge. Scans, detailed in Figure 4.2, found an average surface roughness

of 74.4 nm. The etching technique leads to scalloping of the surface parallel to the target surface and perpendicular striations towards the target rear. Neither pose any concern with regards to interfering with the laser pulse in transmission. The target design and scans were performed by Sam Astbury [191]. Before firing target edges, HHG production will be optimised for unstructured silicon wafer targets, providing information on the bulk propagating ZVP electron bunches for comparison with the mass-limited case. Again, a quarter-wave plate can be implemented to suppress the ZVP mechanism in the absence of vector potential zeroes.

Some relaxation can be anticipated in the requirement for sub-micron precision. There will be some target smoothing via preplasma expansion and the smoothing effect of the main pulse interaction as noted by Dromey *et al* [175]. Furthermore, transmission direction is dictated by laser vector potential and not surface angle, unlike reflection. At worst, ZVP energy scalings will be mildly affected by the change in angle. Thus tape drives will also be explored as an option. However, the 50  $\mu\text{m}$  jitter of such devices suggests a success rate of  $\sim 4\%$ . The gathering of sufficient statistics is not necessarily unreasonable with the high shot rate of GEMINI PW. Shot-to-shot variations in laser pulse focal spot position are typically on the order of the focal spot itself. It is likely therefore that a third of silicon wafer target shots will hit a adequate portion of the target edge.

Successful shots will be identified using a third harmonic imaging line [192]. This diagnostic will also reduce the uncertainty of the hole boring calculations. The non-linearity of the third harmonic production mechanism reduces the possibility of background noise, producing a clear signal and a closer match to the true spot size than the X-ray emission diagnostics of the ORION experiment. For high resolution, the collimating reflective optic must be placed roughly the distance of the  $f/2$  parabola focal length from the main interaction. Near the main interaction region, the B-integral is large thus precluding the use of ND filters and lenses. Instead, a wedge, typically double-passed acts as an attenuator to extract the lower order highly divergent harmonics. A hole allows the less divergent higher orders through, enabling on-shot measurement. Far from the interaction, the collimated third harmonic

signal can be extracted, filtered, refocused and imaged. Some light is reflected to the target via the wedge on the second pass, however this is not a concern. The focal length of the new optic is larger than that of the  $f/2$  parabola and path lengths are on the order of a nanometre at which time the target does not reflect specularly.

Resolving the  $16\text{ }\mu\text{m}$  GEMINI PW spot is significantly more challenging than the  $6\text{ }\mu\text{m}$  spot of the 1 J Astra-GEMINI laser system. This imaging line has been modelled by the ORION laser scientists using Zemax [193] accounting for all diffraction and spherical aberration. They have identified a set-up using two spherical mirrors for collimated and imaging that provides  $10\text{ }\mu\text{m}$  resolution with 20 times magnification, reasonably resolving the spot. While the high spatial orders associated with the clipping of the reflected beam at the target edge cannot be resolved, this should significantly alter the image structure, enough to identify their presence. Over time the wedge will be coated by material ablated from the main target interaction and will need to be replaced to prevent absorption increases and corresponding heat damage.

The size of the wedge hole must be established. Sitting somewhere between the near and far field, to first order, rays from all parts of the spot are lost equally through the hole in the wedge. After passing through the optical system, therefore, the wedge hole should simply reduce the signal at the image plane and not affect the resolution but should be modelled. One could argue that the wedge can reduce the spherical aberration by the removal of paraxial rays. The larger the hole the less likely the clipping of the potentially highly divergent high harmonic beam. Eventually this will impact the third harmonic image resolution. At a minimum the OHREX crystal must be fully illuminated requiring a half angle of  $0.71^\circ$ .

Applying the extended ZVP theory to the oblique incidence case for GEMINI PW parameters predicts electron bunches with a charge of  $\approx 10\text{ nC}$  and energy of  $\approx 30\text{ MeV}$ . Thus, a  $15\text{ }\mu\text{m}$  of aluminium foil filter will reject the laser light without significantly affecting the electron bunches. Firstly, mass-limited and bulk electron bunch trajectories and beam divergences will be imaged on a LANEX screen. An MeV electron spectrometer aligned to the target edge can then measure

the time-integrated energy spectrum. The spatially separated bunch types can be independently measured by adjusting the spectrometer position. Mordovanakis *et al* used Image Plate stacks to obtain the electron bunch structure and emission angle. This may prove necessary if the bunch types overlap due to high divergence [194].

While resolving attosecond durations remains a serious technical challenge of experimental science, we hope to measure the production of Coherent Transition Radiation from a secondary target and therefore infer the presence of a bunch train [113].

COTR - awaiting papers from Peter

When electrons pass from one medium to another they emit transition radiation, in this case, the aluminium filter. If they are arranged into temporally regular spaced bunches that radiation becomes coherent and harmonics of the temporal spacing of the bunches can be observed. Both bulk propagating and mass-limited ZVP electron bunches will produce COTR, however, the attosecond duration should mean the mass-limited bunches produce significantly brighter COTR that extends to XUV energies but that can be distinguished even at the optical range.

#### 4.4 Application of HHG to white light Laue diffraction

The eventual but still somewhat distant goal is the generation of an attosecond X-ray diagnostic to illuminate crystal dynamics on attosecond timescales. Inspired by Laue diffraction measurements demonstrating dislocation microstructure of shocked crystals [195], this will be a proof of principle test of Laue diffraction from an X-ray harmonic beam of a single unshocked crystal.

It was Laue diffraction that led to the discovery of Bragg's law,

$$n\lambda = 2d \sin \theta \quad (4.1)$$

for diffraction order,  $n$ , incident wavelength,  $\lambda$ , the distance between crystal planes,  $d$ , and angle between the crystal plane and the incident photon,  $\theta$  [196]. Irradiation of a crystal target with a 'white light', *i.e.* a broadband X-ray source, Equation 4.1

is satisfied for a range of crystal planes and corresponding angles simultaneously, *producing Laue spots* accordingly. The quasi-broadband X-ray harmonic beam is well suited to such an experiment provided sufficient photon numbers can be obtained.

This will be attempted using the **BBXRD!** (**BBXRD!**) diagnostic placed in the path of the specularly reflected beam and roughly 50 cm from the target. The lead-shielded and IP lined BBXRD contains the crystal sample with a hole to allow the harmonic beam to enter. The sample is placed at an angle on a rotatable washer enabling a range of angles and corresponding energies to be tested: starting with a quartz target to investigate photon energies of 1.7 - 2.5 keV and moving to silicon to explore energies of 2.4 - 3.3 keV. The IP must be shielded to reject laser light, beryllium is most suitable. It may be necessary to integrate over multiple shots to produce the Laue spot.

## 4.5 Contrast

### 4.5.1 Contrast on GEMINI PW

An underlying current of this thesis has been the subject of prepulse and corresponding preplasma expansion. While bright X-ray harmonics have been observed on both the Vulcan [161] and ORION sub-ps laser systems, few cycles laser pulse systems routinely underperform. To date only at normal incidence (thus minimising heating) have harmonics been observed on GEMINI PW [202]. Evidence points to preplasma formation. The only parameter that has been shown to suppress HHG from a p-polarised relativistic laser pulse is an overlarge preplasma [173] and indeed the transition to suppression is rapid [199]. While there exists established theories on the operation of plasma mirrors, these are based on fairly large assumptions that remain untested. Given the notoriety of the challenge of observing SHHG despite laser contrast being a relatively well understood concept and the general successes attributed to hydrodynamic codes, it seems quite possible that these large assumptions are the critical concern. They could also be responsible for the range of optimal scale lengths observed in experiments.

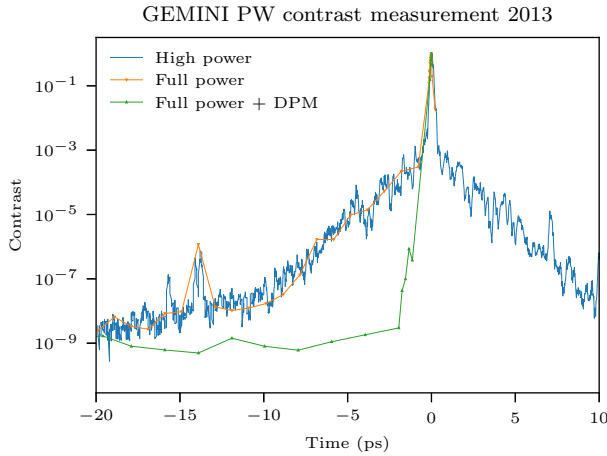


**Figure 4.3:** Native contrast of the GEMINI PW laser system measured using the Sequoia third order autocorrelator scans. The noise floor of the detector is  $\approx 1 \times 10^{-9}$ . The resolution is 100 fs, thus the main pulse is not resolved by the detector.

The last available contrast measurements of the GEMINI PW laser are presented in Figure 4.3. The **DPM!** setup improves the contrast by at least  $10^5$ . More recent measurements of the GEMINI PW DPM system have found a reflectivity of  $1.23 \times 10^{-4} \%$  and 60 % before and after switch on, corresponding to a contrast enhancement of  $4.88 \times 10^5$ . Note that the DPM setup includes an acetate debris shield, without which shot quality would quickly degrade from plasma ablation between the mirrors.

Note in Figure 4.3 the early switch-on of the plasma mirror system. For a peak intensity on **PM!** of  $1 \times 10^{16} \text{ W cm}^{-2}$ , this switch occurs an order of magnitude below typical ionising intensities [70]. Early PM switch-ons is nothing new [201], however, it points to a serious issue. Such early switch-ons cannot be described by the basic theory nor hydrodynamic simulation. Perhaps all can be explained by the complex atomic scale interaction of the laser pulse with the dielectric AR coating. Indeed, perhaps the haste to maximise the contrast at the nanosecond pedestal has been the downfall at the picosecond scale. And yet, providing the measured GEMINI PW contrast data to HYADES simulations predicts acceptable preplasmas, inconsistent with the experiment results.

Recent work has shown evidence of the propagation of an opacity front into a target due to laser prepulse before ionisation and plasma formation. Such a transition from transparency will dramatically affect laser pulse energy deposition into the

target leading to significantly earlier plasma mirror switch-on times. The interaction appears to occur a few picoseconds, a timescale to which preplasma scale length is highly sensitive. Note that such an interaction would be impossible to simulate given the multiple scales upon which preplasma formation occurs and the complexity of the transition to opacity. The GEMINI experiment, however, provides an excellent opportunity to probe this process in parallel to the main experimental goals.

A pure fused silica target consists of valence and conduction bands only. Electrons are excited to the conduction band by the laser and then simply drop back down again. As impurities are added to the target, the band structure becomes more complex and electrons can drop to intermediate states from which they cannot then return easily to the ground state. Thus, more energy can be absorbed and the transition to opacity occurs at earlier times. Hence, the more pure a silica target, the later the transition to opacity and the smaller the preplasma scale length. This also suggests switching out the first plasma mirror for a pure uncoated silica target could also improve contrast at the timescales where it matters. Now the first PM deals with the ps pedestal with its later switch on and the second PM the ns pedestal with its AR coating.

Presumably early plasma formation also occurs for Vulcan or ORION targets, however, once relativistic intensities are reached, recompression will occur. For such long pulse durations, there is sufficient time for steepening before the main interaction.

Contrast reduction will only become more critical with the arrival of sub-eta watt class next generation laser facilities where native picosecond pedestals will already be relativistic. Steep preplasma scale lengths is not only relevant to the matters presented in this thesis but is essential for any thin foil interaction including the popular use case of ion acceleration via TNSA.

To investigate early plasma switch on, a 50 ps chirped probe beam will be focused on the target. Optical spectrometers in transmission and reflection will identify the opacity and plasma generation times respectively. This measurement could categorically demonstrate the failure of hydrodynamic codes for any pre-ionisation

laser pulse intensities. One may wonder why such a failure is not identified in other branches of HED physics, such as the case of Inertial Confinement Fusion. It is simply a matter of scales. These effects are only relevant for the few femtosecond petawatt laser systems in this case of high sensitivity to preplasma scale length. To distinguish the probe beam from the bright non-linear target interaction, it will be focused on the interaction area out of the main interaction plane and with opposite polarisation.

### Strategy

A series of contingencies has been developed to ensure the observation of harmonics under the assumption that preplasma scale length is the main issue. Phases increase in cost to peak laser intensity and therefore to the theoretical harmonic limit. During optimisation, the OHREX will be replaced with an XUV spectrometer since only the lowest orders will be visible. As of 2019, no experiment to confirm HB theory had been performed on a PW system [163]. Such UV spectrometer measurements could be very interesting both to confirm the HB theory in the PW regime and to infer the intensity increase at PM focus. The first step will be to scan through the focal spot of the laser. Wavefront curvature at the target from slight defocussing can reduce divergence from hole boring thus increasing intensity levels at the detector while also reducing pre-heating.

The next action will be to apodise the beam, again this reduces the intensity on target and the harmonic beam divergence and has been shown to tip preplasma scale length into the optimal regime for HHG [199]. This will reduce the intrinsic prepulse intensity by the same factor as the main pulse. To ensure the SHHG roll-off is above the 2.4 keV harmonics (such that the signal on OHREX is non-negligible), requires  $a_0 > 8$ . Such apodisation would reduce the prepulse by  $\approx 10$  times. Corresponding a reduction in the beam radius of a factor of 2. Apodising can also help remove higher spatial orders, improving the spot at focus. While harmonics were observed on the 1 J precursor to GEMINI PW, Astra-Gemini, apodising back to Astra-Gemini parameters does not guarantee success, the new front end procudes a unique prepulse profile.

The intensity on DPM can be reduced leading to later switch-on times but a lower peak reflectivity. Failing that, there are more drastic measures available. First, a second target chamber layout has been designed that will reduce the angle of incidence on target to  $30^\circ$  to reduce target heating and second, frequency doubling is known to significantly enhance contrast. In fact, as with ORION this will likely overshoot, producing effectively zero preplasma.

Testing frequency doubling would be very useful for demonstrating the validity of the new contrast theory. The frequency doubling crystal available at GEMINI PW will reduce the intensity on target both from the generation efficiency (25 %) and apodisation (9 %) (the crystal has a diameter of 60 mm), therefore if there is an improvement in signal, it must be from the improvement to contrast. While Kahaly *et al* were able to observe harmonics for a beam apodised to  $a_0 = 0.7$  provided the scale length was optimised, resorting to this method to produce harmonics would preclude the observation of X-ray harmonics ,however, it would justify the investment into a larger frequency doubling crystal for future HHG experiments at GEMINI PW. Such a setup would not require a DPM and the diffraction limited spot is smaller. Hence, despite the inevitability of efficiency cost due to the frequency doubling process, similar intensities on target could be realised provided a 25 % efficiency non-apodising frequency doubling crystal.

Once harmonics are visible, aspects of the system can be changed and the opacity and early switch-on hypotheses can be tested by looking for quantitative improvements to the signal. Replacing the pure fused silica target with impure BK7 or AR-coated targets should reduce the harmonic signal. Equally, replacing the first PM in the DPM chain with an uncoated PM should delay the PM switch on and improve the signal. Note that the CWE signal is distinguishable from the HHG signal: it is more divergence and experiences a sharp cuts off at the plasma frequency [199].

#### 4.5.2 Kahaly mirror

At some point, the signal will overshoot and enter the CWE regime, preferably early in the list of contingencies presented, and the preplasma scale length can

now be optimised. Kahaly *et al* [199] designed a simple but elegant method to do this. Simply partially cover a mirror in the laser chain with a small mirror. The difference in path length of light on this mirror is determined by the mirror thickness and distance from the main laser mirror surface. Thus this added prepulse arrival time at the target can be controlled. Since this has effectively apodised the beam, the parabola will then focus the prepulse spot to a larger area compared to the main pulse spot ensuring a uniform preplasma across the main spot while the diffraction-limited main spot will experience minimal aberration from to the subtracted prepulse. The target must be routinely monitored to ensure the prepulse spot coincides with the main pulse spot. The mirror should have a mirrored back surface and an AR-coated front surface with a slight angle between the two faces to prevent any parasitic prepulse.

Kahaly *et al* show a linear relationship between main pulse delay relative to prepulse and scale length (due to more time for the preplasma to expand) but also note that for the same scale length, a larger delay (accompanied by smaller energy in the prepulse) produces higher quality harmonics. This could be understood as a natural consequence of the lower plasma temperatures, which improve the ability of the system to perform coherent SHHG behaviour. If harmonics are accessed using the Kahaly method, the signal can be improved our signal by moving the prepulse mirror further from the main pulse mirror while also reducing the fraction of overlap between the two mirrors to reduce the energy in the prepulse. The Kahaly mirror should be placed before the final mirror before the parabola. The further back in the chain it is placed, diffraction from the mount can cause greater danger to the optical system. The linear relationship between main pulse delay and scale length coupled with the XUV HHG signal measurements can be applied to discrete changes to the system to quantify contrast improvements.

## 4.6 Beyond GEMINI PW

This experiment will hopefully be only the start. Contrast measurements will certainly be interesting and influential if cracked.

Expand the range of targets A range of thick, flat solid targets are proposed to probe the density parameter space: diamond, a selection of plastics (polymethyl methacrylate, low and high-density polyethylene and polycarbonate) and mirrored targets, which produced interesting and slightly unexpected results in the ORION experiment. It would also be interesting to produce foam targets gaining access to the optimal low  $S$  regime [203].

It is indispensable, to test the new predictions for oblique incidence energy scalings and total electron bunch charge along with the angle of bunch ejection, the non-zero transverse vector potential of the laser will prevent the bunch from propagating directly along the transmission axis. It would also be useful to perform a parameter scan of the preplasma scale length. In this work so far, it was assumed that the optima for electron bunch production are simply those for HHG, as was shown to be true for preplasma scale length in the Supplementary Information of [115] for their electron bunches in reflection. To truly demonstrate the attosecond duration of the ZVP electron bunches would require imaging of their XUV CTR harmonics.

The return of HHG study to CLF after more than a decade hiatus is certainly indicative of a wider renewed interest in the field, perhaps spurred on by the recent Nobel Prize for attosecond physics and the rapid adoption of multi-petawatt class facilities. Vulcan 20-20 is only around the corner. Set to be the worlds most powerful laser, this ambitious laser facility will provide 200 J in 20 fs. With the capability to access triple digits of peak normalised vector potentials it is ideally suited to the study of X-ray HHG and ZVP. This experiment will build expertise providing proof of principle results with a bright future in mind.

Perhaps in the summary of work of the thesis (new chapter), note that some of the actions laid out by Savin in his future work have been achieved, ie, experiment to measure ZVP electron bunches and theoretical model for the scaling of absorption efficiency with  $S$

GPU 1D simulations of X-ray HHG

# Appendices



# A

## General plasma physics

### Contents

---

A.1	Lorentz transformations of electromagnetic fields	133
A.2	The headlight effect	134
A.3	Geometric transverse emittance	134
A.4	The Bourdier method	137

---

### A.1 Lorentz transformations of electromagnetic fields

The Lorentz transformations for electromagnetic field components parallel,  $\parallel$ , and perpendicular,  $\perp$ , to a frame of reference boost of velocity  $\mathbf{v}$  are [74]

$$\mathbf{E}'_{\parallel} = \mathbf{E}_{\parallel}, \quad (\text{A.1})$$

$$\mathbf{B}'_{\parallel} = \mathbf{B}_{\parallel}, \quad (\text{A.2})$$

$$\mathbf{E}'_{\perp} = \gamma_{\mathbf{v}}(\mathbf{E}_{\perp} + \mathbf{v} \times \mathbf{B}), \quad (\text{A.3})$$

$$\mathbf{B}'_{\perp} = \gamma_{\mathbf{v}}(\mathbf{B}_{\perp} - \mathbf{v} \times \mathbf{E}/c^2). \quad (\text{A.4})$$

## A.2 The headlight effect

The headlight effect describes the beaming of an isotropically emitting source travelling at some velocity relative to an observer. Consider the geometry of figure 2.2 with the source (the laser pulse) travelling at an angle  $2\theta$  to the observer (in this case, the ablating front). A photon with energy  $E$  emitted from the rest frame of the source (the laboratory frame in this case) has a 4-momentum

$$\mathbf{P}_\mu = \left( \frac{E}{c}, \frac{E}{c} \cos 2\theta, \frac{E}{c} \sin 2\theta \right). \quad (\text{A.5})$$

As the interaction geometry is confined to a 2D plane, the  $z$ -component can be safely neglected. Applying the lorentz boost of equation 1.30,

$$\begin{aligned} \frac{E'}{c} &= \gamma \left( \frac{E}{c} - \beta \frac{E}{c} \cos 2\theta \right) \\ \frac{E'}{c} \cos 2\theta' &= \gamma \left( \frac{E}{c} \cos 2\theta - \beta \frac{E}{c} \right). \end{aligned} \quad (\text{A.6})$$

Solving these equations for the angle in the boosted frame,

$$\cos 2\theta' = \frac{\cos 2\theta - \beta}{1 - \beta \cos 2\theta}. \quad (\text{A.7})$$

## A.3 Geometric transverse emittance

A beam<sup>1</sup> of particles is fully described by its six-dimensional particle phase space distribution

$$\rho(\mathbf{x}, \mathbf{p}) = \rho(x, p_x, y, p_y, z, p_z), \quad (\text{A.8})$$

where  $\mathbf{p} = p_x \hat{\mathbf{x}} + p_y \hat{\mathbf{y}} + p_z \hat{\mathbf{z}}$  is the canonical momentum [133]. Under the Hamilton formalism, for ideal conditions, the six-dimensional volume of the beam in this space, termed the *emittance*, arises as a conserved quantity and is therefore a useful quantity to describe the beam quality. (something to do with it affecting the ability to focus the beam?? check the papers) It is useful to rotate the coordinate system so as to align with the beam's propagation. The distribution can be written as

$$\rho(\mathbf{x}', \mathbf{p}') = \rho(x_L, p_L, x_T, p_T, x_{T'}, p_{T'}), \quad (\text{A.9})$$

---

<sup>1</sup>In this section it is electron beams and not bunches that are referred to to demonstrate the generality of these concepts.

where L is longitudinal to the beam's propagation direction, and T and T' are two orthogonal directions transverse to the beam's propagation. Where discussed in this thesis, T' will unanimously refer to the  $z$ -direction, that is, the additional direction in 3D simulations, all such simulations are designed such that the  $z$ -direction is transverse to the beam propagation direction.

Recording a six-dimensional phase space in experiment is impossible while in simulations it is almost prohibitively costly in terms of data storage. Hence, it is common practice to project the distribution onto three orthogonal sub-spaces corresponding to each spatial axis, L, T and T' and compute the area on each. Note that since the electron beam is ultra-relativistic, all electrons propagate at approximately c and therefore it is the transverse and not the longitudinal emittance that describes the beam's quality. As a particle beam does not typically exist with well-defined borders, the area used to describe the emittance is restricted to an ellipse containing only the high-density core of the distribution. For a subspace  $i$ , where  $i = T$  or  $T'$ , Floettmann *et al* [205] derive the *transverse normalised emittance* as

$$\epsilon_{n,rms}^i = \frac{1}{m_e c} \sqrt{\langle x_i^2 \rangle \langle p_i^2 \rangle - \langle x_i p_i \rangle^2}, \quad (\text{A.10})$$

where  $\langle \rangle$  is the second central moment of the particle distribution,

$$\langle ab \rangle = \frac{\int ab \rho(\mathbf{x}', \mathbf{p}') dV}{\int \rho(\mathbf{x}', \mathbf{p}') dV} - \frac{\int a \rho(\mathbf{x}', \mathbf{p}') dV \int b \rho(\mathbf{x}', \mathbf{p}') dV}{(\int \rho(\mathbf{x}', \mathbf{p}') dV)^2}, \quad (\text{A.11})$$

here  $dV = \Pi_j dx_j dp_j$  for  $j = L, T, T'$ .

When working with emittances, most frequently in the literature it is the *transverse geometric emittance*,  $\epsilon_{rms}^i$  that is discussed. This is a natural consequence of it being more readily accessible in experiments [133]. The geometric and normalised emittances are related via

$$\epsilon_{rms}^i = \frac{\epsilon_{rms}^i}{\gamma \beta_L}, \quad (\text{A.12})$$

where  $\gamma = 1/\sqrt{1-\beta^2}$  refers to the beam's mean energy and  $\beta_L \approx c$  is the ultrarelativistic beam's longitudinal speed.

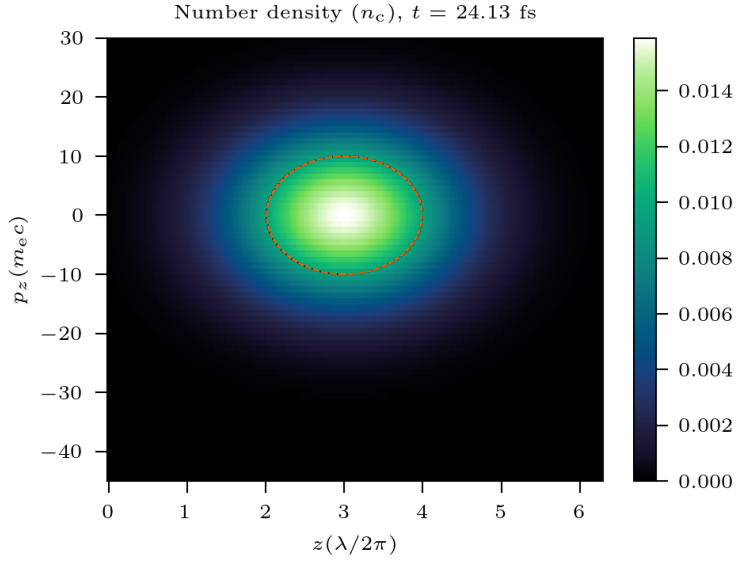


**Figure A.1:** Emittance calculation for an ideal Gaussian distribution in phase space,  $f_n(z, p_z) = 1/(2\pi s_z s_{pz}) \exp[-((z - m_z)^2/(2s_z^2) + (p_z - m_{pz})^2/(2s_{pz}^2))]$ , centred at  $(m_z, m_{pz}) = (3, 0)$  with standard deviations  $(s_z, s_{pz}) = (1, 10)$ .

The Courant-Snyder invariant which describes the ellipse that corresponds to the emittance is<sup>2</sup>

$$\epsilon_{\text{rms}}^i = \gamma x_i^2 + 2\alpha x x' \beta x_i'^2, \quad (\text{A.13})$$

here the coordinates are  $x_i$  and  $x'_i = p_i/p_L$  [206]. The Twiss parameters are

$$\alpha = -\frac{\langle x_i x'_i \rangle}{\epsilon_{\text{rms}}^i}, \quad (\text{A.14})$$

$$\beta = \frac{\langle x_i \rangle}{\epsilon_{\text{rms}}^i} \quad (\text{A.15})$$

and

$$\gamma = \frac{\langle x_i'^2 \rangle}{\epsilon_{\text{rms}}^i}. \quad (\text{A.16})$$

Thus the shape of the ellipse and the divergence of the beam can be determined. The elliptical contour defining the emittance of an ideal Gaussian phase-space distribution is given in Figure A.1. The contour is numerically calculated to contain 39.4(1) % of the particles, compared to 39.3 % from theory. Here the discrepancy arises from the finite grid on which the distribution is defined.

---

<sup>2</sup>Regrettably  $\beta$  and  $\gamma$  are the standard notations for the Twiss parameters, at all other locations in this Thesis, these parameters will refer to the standard relativistic beta and gamma factors of objects respectively.

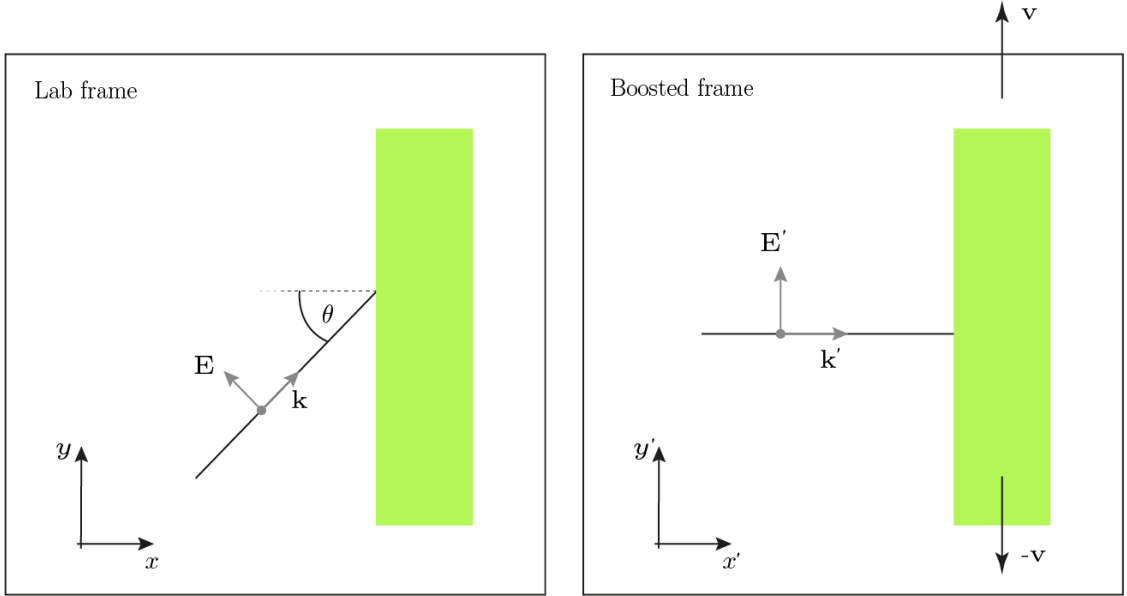


Figure A.2

## A.4 The Bourdier method

The Bourdier method enables the modelling of an obliquely incident laser pulse in 1D geometry [167]. While some of this section may seem trivial, it is frequently misquoted in the literature. It therefore seems of great importance to provide a full derivation.

Consider a photon incident on a plasma block at angle  $\theta$  as in Figure A.2. A boost is applied with velocity  $\mathbf{v}$  to the laboratory frame such that the photon is normally incident on the now streaming plasma at velocity  $-\mathbf{v}$ . The velocity transformation for the photon's velocity,  $\mathbf{u}$ , parallel to the boost is

$$\mathbf{u}'_{\parallel} = \frac{\mathbf{u}_{\parallel} - \mathbf{v}}{1 - \mathbf{u} \cdot \mathbf{v}/c^2}. \quad (\text{A.17})$$

Setting  $\mathbf{u}'_{\parallel} = 0$ , it is clear that

$$\mathbf{v} = \mathbf{u}_{\parallel} = c \sin \theta \hat{\mathbf{y}} \quad (\text{A.18})$$

in this geometry and

$$\gamma_v = \frac{1}{\sqrt{1 - \mathbf{v}^2/c^2}} = \sec \theta. \quad (\text{A.19})$$

Since Snell's law is frame invariant, the photon remains normal as it propagates into the skin depth of the plasma, a frame in which the interaction reduces to a 1D problem has been successfully found for all  $\theta < \pi/2$ . Those familiar with the topic may wonder how this is possible considering the 'ripples' that can be observed on the plasma surface for oblique incidence. The explanation for this is of course the relativity of simultaneity.

It remains to determine how do all the relevant quantities transform as such a boost is applied. Starting with a simple one: the photon's wave four-vector is

$$\mathbf{K}^\mu = \left( \frac{\omega}{c}, \mathbf{k} \right) \quad (\text{A.20})$$

and thus the frequency transforms as

$$\frac{\omega}{c} = \gamma_v \left( \frac{\omega'}{c} - \frac{\mathbf{v} \cdot \mathbf{k}'}{c} \right). \quad (\text{A.21})$$

Since  $\mathbf{v} \cdot \mathbf{k}' = 0$ ,

$$\omega' = \omega \cos \theta. \quad (\text{A.22})$$

As

$$n'_c = \frac{m_e(\omega')^2}{4\pi e^2}, \quad (\text{A.23})$$

$$n'_c = n_c \cos^2 \theta, \quad (\text{A.24})$$

while the plasma block will be Lorentz contracted along  $\hat{\mathbf{y}}$ . Hence, the number density of electrons will increase as

$$n'_e = \frac{n'_e}{\cos \theta} \quad (\text{A.25})$$

leading to the perhaps unexpected

$$\bar{n}'_e = \frac{\bar{n}_e}{\cos^3 \theta}. \quad (\text{A.26})$$

Time is dilated

$$t' = \frac{t}{\cos \theta}. \quad (\text{A.27})$$

Consider now the more general case where the photon's electric field is rotated out of the  $x$ - $y$  plane, *i.e.*

$$\mathbf{E} = E_0(-\cos \phi \sin \theta, \cos \phi \cos \theta, \sin \phi) \quad (\text{A.28})$$

and correspondingly

$$\mathbf{B} = \frac{\hat{\mathbf{k}} \times \mathbf{E}}{c} = \frac{E_0}{c}(\sin \phi \sin \theta, -\sin \phi \cos \theta, \cos \phi). \quad (\text{A.29})$$

The Lorentz transformations for electro-magnetic fields are

$$\mathbf{E}'_{\parallel} = \mathbf{E}_{\parallel}, \quad (\text{A.30})$$

$$\mathbf{B}'_{\parallel} = \mathbf{B}_{\parallel}, \quad (\text{A.31})$$

$$\mathbf{E}'_{\perp} = \gamma_{\mathbf{v}}(\mathbf{E}_{\perp} + \mathbf{v} \times \mathbf{B}), \quad (\text{A.32})$$

$$\mathbf{B}'_{\perp} = \gamma_{\mathbf{v}}(\mathbf{B}_{\perp} - \mathbf{v} \times \mathbf{E}/c^2). \quad (\text{A.33})$$

Using the above expressions for  $\mathbf{E}_{\perp}$  and  $\mathbf{E}_{\parallel}$  and transforming to the boosted frame,

$$\mathbf{E}' = E_0 \cos \theta(0, \cos \phi, \sin \phi). \quad (\text{A.34})$$

As anticipated for normal incidence there is no component of the E-field normal to the surface. Conveniently, the polarisation of the incident photon is unchanged despite having components both parallel and perpendicular to the transformation and

$$|\mathbf{E}'| = |\mathbf{E}| \cos \theta. \quad (\text{A.35})$$

The picture can now be completed. Since

$$a'_0 = \frac{e|\mathbf{E}'|}{m_e e \omega'} \quad (\text{A.36})$$

it follows that [204]

$$a'_0 = a_0, \quad (\text{A.37})$$

$$S' = \frac{S}{\cos^3 \theta}. \quad (\text{A.38})$$

Normalised Smilei units now come into their own in this new framework. In Smilei units, distances, times and vector potentials are unchanged by the interaction and can simply be extracted from the simulation in the required frame by multiplying by the frame of interest's reference quantity. Care must still be taken with densities.



# B

## PIC simulations

---

### Contents

---

B.1 Convergence of 3D PIC simulations . . . . .	141
---	-----

---

### B.1 Convergence of 3D PIC simulations

To reduce the computation cost of the large 3D simulations, a lower resolution version of the original 3D simulation was performed. Results are presented in figure B.1, demonstrating reasonable convergence.

### B.1. Convergence of 3D PIC simulations

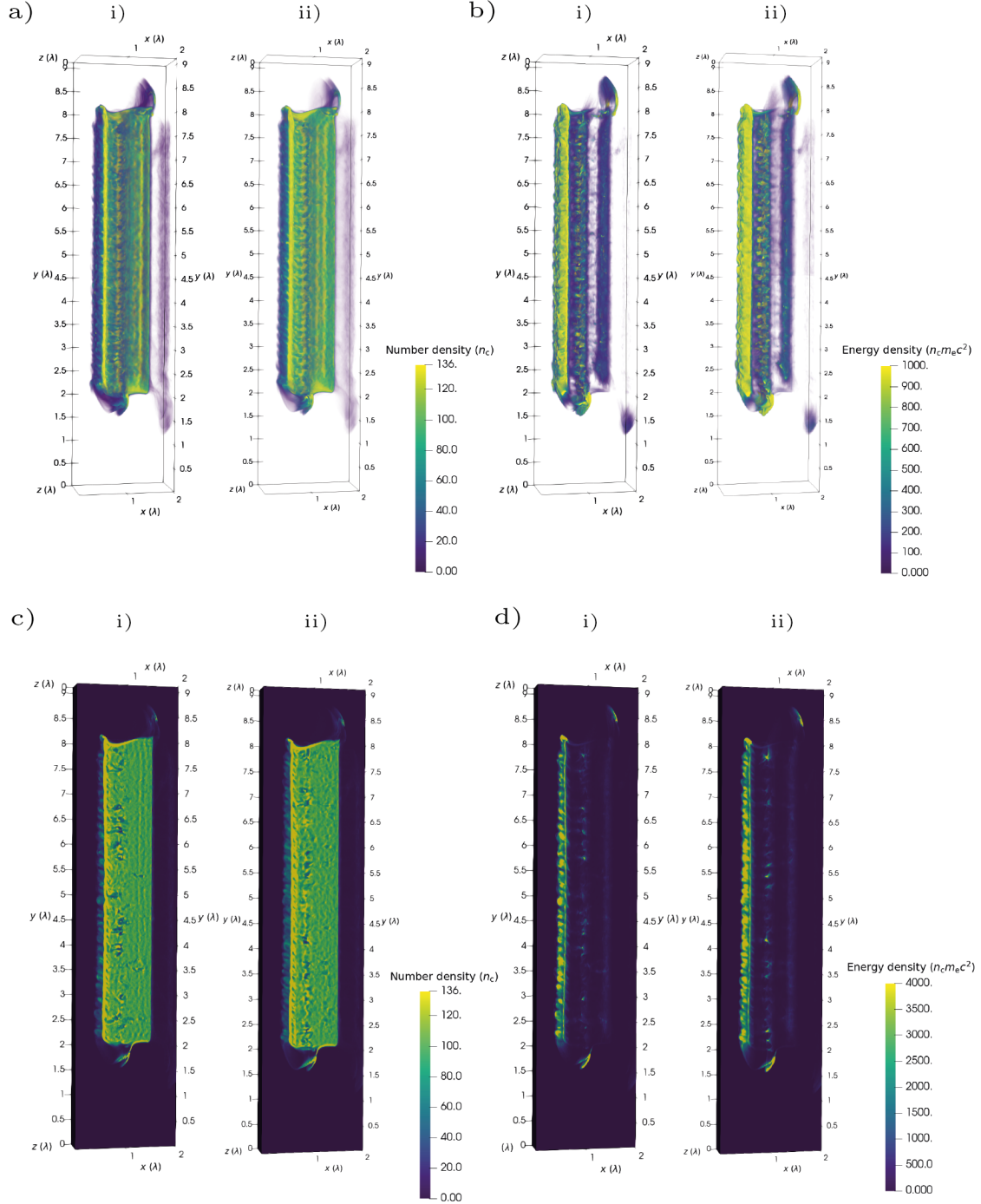


**Figure B.1:** Comparison between the initial 3D simulation and a lower resolution version. a) Electron number density. b) Kinetic energy density. c) and d) are slices of a) and b) respectively. *i*) Initial simulation. *ii*) Lower resolution simulation. Good convergence is demonstrated.

## References

- [1] Douglas Kothe, Stephen Lee, and Irene Qualters. “Exascale Computing in the United States”. In: *Computing in Science & Engineering* 21.1 (Jan. 1, 2019), pp. 17–29.
- [2] Donna Strickland and Gerard Mourou. “Compression of Amplified Chirped Optical Pulses”. In: *Optics Communications* 55.6 (Oct. 1985), pp. 447–449.
- [3] I.N. Ross, P. Matousek, and J.L. Collier. “Optical Parametric Chirped Pulse Amplification”. In: *Conference on Lasers and Electro-Optics (CLEO 2000). Technical Digest. Postconference Edition. TOPS Vol.39 (IEEE Cat. No.00CH37088)*. Conference on Lasers and Electro-Optics (CLEO 2000). Technical Digest. Postconference Edition. TOPS Vol.39. San Francisco, CA, USA: IEEE, 2000, p. 249.
- [4] S. Fourmaux et al. “Pedestal Cleaning for High Laser Pulse Contrast Ratio with a 100 TW Class Laser System”. In: *Optics Express* 19.9 (Apr. 25, 2011), p. 8486.
- [5] Yong Wang et al. “085 PW Laser Operation at 33 Hz and High-Contrast Ultrahigh-Intensity = 400 Nm Second-Harmonic Beamline”. In: *Optics Letters* 42.19 (Oct. 1, 2017), p. 3828.
- [6] G. Tiscareno et al. “The Ohio State University Scarlet Laser Facility - Open To External Users Via LaserNetUS”. In: 2020 (Jan. 1, 2020), CP15.001. URL: <https://ui.adsabs.harvard.edu/abs/2020APS..DPPC15001T> (visited on 09/19/2023).
- [7] Jae Hee Sung et al. “42 PW, 20 Fs Ti:Sapphire Laser at 01 Hz”. In: *Optics Letters* 42.11 (June 1, 2017), p. 2058.
- [8] Ian N. Ross et al. “Generation of Terawatt Pulses by Use of Optical Parametric Chirped Pulse Amplification”. In: *Applied Optics* 39.15 (May 20, 2000), p. 2422.
- [9] Xiaodong Yang et al. “Multiterawatt Laser System Based on Optical Parametric Chirped Pulse Amplification”. In: *Optics Letters* 27.13 (July 1, 2002), p. 1135.
- [10] Stefan Witte et al. “A Source of 2 Terawatt, 2.7 Cycle Laser Pulses Based on Noncollinear Optical Parametric Chirped Pulse Amplification”. In: *Optics Express* 14.18 (2006), pp. 8168–8177.
- [11] C. Stoeckl et al. “High-Energy Petawatt Project at the University of Rochester’s Laboratory for Laser Energetics”. In: *Fusion Science and Technology* 49.3 (Apr. 2006), pp. 367–373.
- [12] V V Lozhkarev et al. “Compact 0.56 Petawatt Laser System Based on Optical Parametric Chirped Pulse Amplification in KD\*P Crystals”. In: *Laser Physics Letters* 4.6 (June 1, 2007), pp. 421–427.

- [13] Daniel Herrmann et al. “Generation of Sub-Three-Cycle, 16 TW Light Pulses by Using Noncollinear Optical Parametric Chirped-Pulse Amplification”. In: *Optics Letters* 34.16 (Aug. 15, 2009), p. 2459.
- [14] Giedrius Andriukaitis et al. “90 GW Peak Power Few-Cycle Mid-Infrared Pulses from an Optical Parametric Amplifier”. In: *Optics Letters* 36.15 (Aug. 1, 2011), p. 2755.
- [15] Kun Zhao et al. “Generation of 120 GW Mid-Infrared Pulses from a Widely Tunable Noncollinear Optical Parametric Amplifier”. In: *Optics Letters* 38.13 (July 1, 2013), p. 2159.
- [16] Nicholas Hopps et al. “Overview of Laser Systems for the Orion Facility at the AWE”. In: *Applied Optics* 52.15 (May 20, 2013), p. 3597.
- [17] Nicolas Thiré et al. “10 mJ 5-Cycle Pulses at  $1.8 \mu\text{m}$  through Optical Parametric Amplification”. In: *Applied Physics Letters* 106.9 (Mar. 2, 2015), p. 091110.
- [18] Yanchun Yin et al. “High-Efficiency Optical Parametric Chirped-Pulse Amplifier in BiB<sub>3</sub>O<sub>6</sub> for Generation of 3 mJ, Two-Cycle, Carrier-Envelope-Phase-Stable Pulses at 17 m”. In: *Optics Letters* 41.6 (Mar. 15, 2016), p. 1142.
- [19] S Gales et al. “The Extreme Light Infrastructure—Nuclear Physics (ELI-NP) Facility: New Horizons in Physics with 10 PW Ultra-Intense Lasers and 20 MeV Brilliant Gamma Beams”. In: *Reports on Progress in Physics* 81.9 (Sept. 1, 2018), p. 094301.
- [20] *OMEGA Facility*. Laboratory for Laser Energetics, University of Rochester. URL: [Lle.rochester.edu/omega%20facility](http://Lle.rochester.edu/omega%20facility).
- [21] J. Ren et al. “A Compact Double-Pass Raman Backscattering Amplifier/Compressor”. In: *Physics of Plasmas* 15.5 (May 1, 2008), p. 056702.
- [22] L. Lancia et al. “Experimental Evidence of Short Light Pulse Amplification Using Strong-Coupling Stimulated Brillouin Scattering in the Pump Depletion Regime”. In: *Physical Review Letters* 104.2 (Jan. 11, 2010), p. 025001.
- [23] L. Lancia et al. “Signatures of the Self-Similar Regime of Strongly Coupled Stimulated Brillouin Scattering for Efficient Short Laser Pulse Amplification”. In: *Physical Review Letters* 116.7 (Feb. 16, 2016), p. 075001.
- [24] J.-R. Marquès et al. “Joule-Level High-Efficiency Energy Transfer to Subpicosecond Laser Pulses by a Plasma-Based Amplifier”. In: *Physical Review X* 9.2 (Apr. 12, 2019), p. 021008.
- [25] Francis Théberge et al. “Tunable Ultrashort Laser Pulses Generated through Filamentation in Gases”. In: *Physical Review Letters* 97.2 (July 14, 2006), p. 023904.
- [26] Sergei A. Trushin et al. “Sub-10-Fs Supercontinuum Radiation Generated by Filamentation of Few-Cycle 800 nm Pulses in Argon”. In: *Optics Letters* 32.16 (Aug. 15, 2007), p. 2432.
- [27] T I Oh et al. “Intense Terahertz Generation in Two-Color Laser Filamentation: Energy Scaling with Terawatt Laser Systems”. In: *New Journal of Physics* 15.7 (July 3, 2013), p. 075002.

- [28] Takuya Horio, Roman Spesyvtsev, and Toshinori Suzuki. "Generation of Sub-17 Fs Vacuum Ultraviolet Pulses at 133 Nm Using Cascaded Four-Wave Mixing through Filamentation in Ne". In: *Optics Letters* 39.20 (Oct. 15, 2014), p. 6021.
- [29] Eiji Takahashi, Yasuo Nabekawa, and Katsumi Midorikawa. "Generation of 10- $\mu$ J Coherent Extreme-Ultraviolet Light by Use of High-Order Harmonics". In: *Optics Letters* 27.21 (Nov. 1, 2002), p. 1920.
- [30] E. Goulielmakis et al. "Single-Cycle Nonlinear Optics". In: *Science* 320.5883 (June 20, 2008), pp. 1614–1617.
- [31] E. Skantzakis et al. "Coherent Continuum Extreme Ultraviolet Radiation in the Sub-100-nJ Range Generated by a High-Power Many-Cycle Laser Field". In: *Optics Letters* 34.11 (June 1, 2009), p. 1732.
- [32] F. Ferrari et al. "High-Energy Isolated Attosecond Pulses Generated by above-Saturation Few-Cycle Fields". In: *Nature Photonics* 4.12 (Dec. 2010), pp. 875–879.
- [33] Eiji J. Takahashi et al. "Attosecond Nonlinear Optics Using Gigawatt-Scale Isolated Attosecond Pulses". In: *Nature Communications* 4.1 (Oct. 25, 2013), p. 2691.
- [34] Dimitar Popmintchev et al. "Ultraviolet Surprise: Efficient Soft x-Ray High-Harmonic Generation in Multiply Ionized Plasmas". In: *Science* 350.6265 (Dec. 4, 2015), pp. 1225–1231.
- [35] Y. Nomura et al. "Attosecond Phase Locking of Harmonics Emitted from Laser-Produced Plasmas". In: *Nature Physics* 5.2 (Feb. 2009), pp. 124–128.
- [36] J Bierbach et al. "Generation of 10  $\mu$  W Relativistic Surface High-Harmonic Radiation at a Repetition Rate of 10 Hz". In: *New Journal of Physics* 14.6 (June 7, 2012), p. 065005.
- [37] P. Heissler et al. "Multi- $\mu$ J Harmonic Emission Energy from Laser-Driven Plasma". In: *Applied Physics B* 118.2 (Feb. 2015), pp. 195–201.
- [38] M. Yeung et al. "Experimental Observation of Attosecond Control over Relativistic Electron Bunches with Two-Colour Fields". In: *Nature Photonics* 11.1 (Jan. 2017), pp. 32–35.
- [39] Olga Jahn et al. "Towards Intense Isolated Attosecond Pulses from Relativistic Surface High Harmonics". In: *Optica* 6.3 (Mar. 20, 2019), p. 280.
- [40] B. Rus et al. "Efficient, High-Brightness Soft-x-Ray Laser at 21.2 Nm". In: *Physical Review A* 55.5 (May 1, 1997), pp. 3858–3873.
- [41] S. Sebban et al. "Full Characterization of a High-Gain Saturated x-Ray Laser at 13.9 Nm". In: *Physical Review A* 61.4 (Mar. 17, 2000), p. 043810.
- [42] B. Rus. "Multi-Millijoule, Highly Coherent X-ray Laser at 21 Nm as a Routine Tool for Applications". In: *AIP Conference Proceedings*. X-RAY LASERS 2002: 8th International Conference on X-Ray Lasers. Vol. 641. Aspen, Colorado (USA): AIP, 2002, pp. 182–190.
- [43] Ph. Zeitoun et al. "A High-Intensity Highly Coherent Soft X-ray Femtosecond Laser Seeded by a High Harmonic Beam". In: *Nature* 431.7007 (Sept. 2004), pp. 426–429.

- [44] Y. Wang et al. “High-Brightness Injection-Seeded Soft-X-Ray-Laser Amplifier Using a Solid Target”. In: *Physical Review Letters* 97.12 (Sept. 18, 2006), p. 123901.
- [45] Nina Rohringer et al. “Atomic Inner-Shell X-ray Laser at 1.46 Nanometres Pumped by an X-ray Free-Electron Laser”. In: *Nature* 481.7382 (Jan. 2012), pp. 488–491.
- [46] V. Ayvazyan et al. “First Operation of a Free-Electron Laser Generating GW Power Radiation at 32 Nm Wavelength”. In: *The European Physical Journal D* 37.2 (Feb. 2006), pp. 297–303.
- [47] W. Ackermann et al. “Operation of a Free-Electron Laser from the Extreme Ultraviolet to the Water Window”. In: *Nature Photonics* 1.6 (June 2007), pp. 336–342.
- [48] P. Emma et al. “First Lasing and Operation of an Ångstrom-Wavelength Free-Electron Laser”. In: *Nature Photonics* 4.9 (Sept. 2010), pp. 641–647.
- [49] *Flash Free-Electron Laser*. DESY. URL: [flash.desy.de](http://flash.desy.de).
- [50] *FELIX Laboratory: Overview and Specifications*. Radboud University. URL: [ru.nl/felix/facility/overview-specification/](http://ru.nl/felix/facility/overview-specification/).
- [51] S. Kneip et al. “Observation of Synchrotron Radiation from Electrons Accelerated in a Petawatt-Laser-Generated Plasma Cavity”. In: *Physical Review Letters* 100.10 (Mar. 14, 2008), p. 105006.
- [52] S. Kneip et al. “Bright Spatially Coherent Synchrotron X-rays from a Table-Top Source”. In: *Nature Physics* 6.12 (Dec. 2010), pp. 980–983.
- [53] J. Ju et al. “Enhancement of X-Rays Generated by a Guided Laser Wakefield Accelerator inside Capillary Tubes”. In: *Applied Physics Letters* 100.19 (May 7, 2012), p. 191106.
- [54] L. M. Chen et al. “Bright Betatron X-ray Radiation from a Laser-Driven-Clustering Gas Target”. In: *Scientific Reports* 3.1 (May 29, 2013), p. 1912.
- [55] Xiaoming Wang et al. “Quasi-Monoenergetic Laser-Plasma Acceleration of Electrons to 2 GeV”. In: *Nature Communications* 4.1 (June 11, 2013), p. 1988.
- [56] J. M. Cole et al. “Laser-Wakefield Accelerators as Hard x-Ray Sources for 3D Medical Imaging of Human Bone”. In: *Scientific Reports* 5.1 (Aug. 18, 2015), p. 13244.
- [57] J. Wenz et al. “Quantitative X-ray Phase-Contrast Microtomography from a Compact Laser-Driven Betatron Source”. In: *Nature Communications* 6.1 (July 20, 2015), p. 7568.
- [58] K. Ta Phuoc et al. “All-Optical Compton Gamma-Ray Source”. In: *Nature Photonics* 6.5 (May 2012), pp. 308–311.
- [59] S. Chen et al. “MeV-Energy X Rays from Inverse Compton Scattering with Laser-Wakefield Accelerated Electrons”. In: *Physical Review Letters* 110.15 (Apr. 10, 2013), p. 155003.

- [60] Hai-En Tsai et al. “Compact Tunable Compton X-Ray Source from Laser-Plasma Accelerator and Plasma Mirror”. In: *Physics of Plasmas* 22.2 (Feb. 1, 2015), p. 023106.
- [61] Mikhail N. Polyanskiy, Igor V. Pogorelsky, and Vitaly Yakimenko. “Picosecond Pulse Amplification in Isotopic CO<sub>2</sub> Active Medium”. In: *Optics Express* 19.8 (Apr. 11, 2011), p. 7717.
- [62] D. Haberberger, S. Tochitsky, and C. Joshi. “Fifteen Terawatt Picosecond CO<sub>2</sub> Laser System”. In: *Optics Express* 18.17 (Aug. 16, 2010), p. 17865.
- [63] J. H. Glownia, M. Kaschke, and P. P. Sorokin. “Amplification of 193-Nm Femtosecond Seed Pulses Generated by Third-Order, Nonresonant, Difference-Frequency Mixing in Xenon”. In: *Optics Letters* 17.5 (Mar. 1, 1992), p. 337.
- [64] M. Kando et al. “Enhancement of Photon Number Reflected by the Relativistic Flying Mirror”. In: *Physical Review Letters* 103.23 (Dec. 4, 2009), p. 235003.
- [65] Stephen Obenschain et al. “High-Energy Krypton Fluoride Lasers for Inertial Fusion”. In: *Applied Optics* 54.31 (Nov. 1, 2015), F103.
- [66] R. M. G. M. Trines et al. “Simulations of Efficient Raman Amplification into the Multipetawatt Regime”. In: *Nature Physics* 7.1 (Jan. 2011), pp. 87–92.
- [67] J. Kawanaka et al. “Conceptual Design of Sub-Exa-Watt System by Using Optical Parametric Chirped Pulse Amplification”. In: *Journal of Physics: Conference Series* 688 (Mar. 2016), p. 012044.
- [68] Toshiki Tajima. “Marriage of a 20keV Superconducting XFEL with a 100PW Laser”. In: *SPIE* (Apr. 16, 2018). URL: [spie.org/news/marriage-of-a-20kev-superconducting-xfel-with-a-100pw-laser?SSO=1](https://spie.org/news/marriage-of-a-20kev-superconducting-xfel-with-a-100pw-laser?SSO=1).
- [69] *Net Electricity Consumption Worldwide in Select Years from 1980 to 2022 (in Terawatt-Hours)*. Statista. URL: <https://www.statista.com/statistics/280704/world-power-consumption/> (visited on 09/26/2023).
- [70] Donald Umstadter. “Relativistic Laser Plasma Interactions”. In: *Journal of Physics D: Applied Physics* 36.8 (Apr. 21, 2003), R151–R165.
- [71] F. Dollar et al. “Enhanced Laser Absorption from Radiation Pressure in Intense Laser Plasma Interactions”. In: *New Journal of Physics* 19.6 (June 1, 2017).
- [72] P. R. Drake and Peter Norreys. “Focus on High Energy Density Physics”. In: *New Journal of Physics* 16 (2014).
- [73] Francis F. Chen. *Introduction to Plasma Physics and Controlled Fusion*. Cham: Springer International Publishing, 2016.
- [74] Andrew M. Steane. *Relativity Made Relatively Easy*. OUP Oxford, Oct. 4, 2012. 437 pp. Google Books: 75rCErZkh7EC.
- [75] J. Derouillat et al. “Smilei : A Collaborative, Open-Source, Multi-Purpose Particle-in-Cell Code for Plasma Simulation”. In: *Computer Physics Communications* 222 (Jan. 2018), pp. 351–373.

- [76] E. Esarey, C. B. Schroeder, and W. P. Leemans. “Physics of Laser-Driven Plasma-Based Electron Accelerators”. In: *Reviews of Modern Physics* 81.3 (Aug. 27, 2009), pp. 1229–1285.
- [77] Eduard Atonga et al. “Gravitational Waves from High-Power Twisted Light”. Version 1. In: (2023).
- [78] S. Gordienko and A. Pukhov. “Scalings for Ultrarelativistic Laser Plasmas and Quasimonoenergetic Electrons”. In: *Physics of Plasmas* 12.4 (Apr. 2005), p. 043109.
- [79] V. I. Eremin, A. V. Korzhimanov, and A. V. Kim. “Relativistic Self-Induced Transparency Effect During Ultraintense Laser Interaction with Overdense Plasmas: Why It Occurs and Its Use for Ultrashort Electron Bunch Generation”. In: *Physics of Plasmas* 17.4 (Apr. 1, 2010), p. 043102. arXiv: 0810.4035 [physics].
- [80] Herbert Goldstein. *Classical Mechanics*. Pearson Education, 2013.
- [81] Igor V. Sokolov et al. “Dynamics of Emitting Electrons in Strong Electromagnetic Fields”. In: *Physics of Plasmas* 16.9 (Sept. 1, 2009), p. 093115. arXiv: 0904.0405 [physics].
- [82] Luca Fedeli et al. “Probing Strong-Field QED with Doppler-boosted PetaWatt-class Lasers”. Dec. 14, 2020. arXiv: 2012.07696.
- [83] F. Niel et al. “From Quantum to Classical Modeling of Radiation Reaction: A Focus on Stochasticity Effects”. In: *Physical Review E* 97.4 (Apr. 25, 2018), p. 043209.
- [84] V. I. Ritus. “Quantum Effects of the Interaction of Elementary Particles with an Intense Electromagnetic Field”. In: *Journal of Soviet Laser Research* 6.5 (1985), pp. 497–617.
- [85] Jon T. Larsen and Stephen M. Lane. “HYADES—A Plasma Hydrodynamics Code for Dense Plasma Studies”. In: *Journal of Quantitative Spectroscopy and Radiative Transfer* 51.1-2 (Jan. 1994), pp. 179–186.
- [86] B. Fryxell et al. “FLASH: An Adaptive Mesh Hydrodynamics Code for Modeling Astrophysical Thermonuclear Flashes”. In: *The Astrophysical Journal Supplement Series* 131.1 (Nov. 2000), pp. 273–334.
- [87] R. A. Fonseca et al. “OSIRIS: A Three-Dimensional, Fully Relativistic Particle in Cell Code for Modeling Plasma Based Accelerators”. In: *Computational Science — ICCS 2002*. Ed. by Peter M. A. Sloot et al. Red. by Gerhard Goos, Juris Hartmanis, and Jan Van Leeuwen. Vol. 2331. Berlin, Heidelberg: Springer Berlin Heidelberg, 2002, pp. 342–351.
- [88] Keith Bennett et al. “Users Manual for the EPOCH PIC Codes”. In: *University of Warwick* (2017).
- [89] *ARCHER2*. URL: <https://www.archer2.ac.uk/> (visited on 08/15/2023).
- [90] *SCARF Overview*. Scarf User Documentation. URL: <https://www.scarf.rl.ac.uk>.
- [91] N.J. Sircombe and T.D. Arber. “VALIS: A Split-Conservative Scheme for the Relativistic 2D Vlasov–Maxwell System”. In: *Journal of Computational Physics* 228.13 (July 2009), pp. 4773–4788.

- [92] A. Bruce Langdon and Charles K. Birdsall. “Theory of Plasma Simulation Using Finite-Size Particles”. In: *The Physics of Fluids* 13.8 (Aug. 1, 1970), pp. 2115–2122.
- [93] Jay Boris. “Relativistic Plasma Simulation-Optimization of a Hybrid Code”. In: 1970, pp. 3–67. URL: [https://books.googleusercontent.com/books/content?req=AKW5Qaeo8UUUCTkUiZGKQfqho3zFTavASZJjYJCvrsSoN\\_u25RLetQyQp8U5iPMIb1VW8Q\\_DgEqvUbZ-MG7\\_9qCd-k3kYfJ01qDFbCqPmbKg1afBwHgq3IlT40yyzs1PFfSHTUTTLYyR5k0LFn2BxKZng8CGWvPzy80fVr832hShsxhHdwPn1\\_DhVDGM3oz7bF1eKbVySrHyf5muZD3oh23aJsg1T\\_8c\\_W5vQp-gsEdPsLqacS8VtJMcoGUbRVFJQg3A](https://books.googleusercontent.com/books/content?req=AKW5Qaeo8UUUCTkUiZGKQfqho3zFTavASZJjYJCvrsSoN_u25RLetQyQp8U5iPMIb1VW8Q_DgEqvUbZ-MG7_9qCd-k3kYfJ01qDFbCqPmbKg1afBwHgq3IlT40yyzs1PFfSHTUTTLYyR5k0LFn2BxKZng8CGWvPzy80fVr832hShsxhHdwPn1_DhVDGM3oz7bF1eKbVySrHyf5muZD3oh23aJsg1T_8c_W5vQp-gsEdPsLqacS8VtJMcoGUbRVFJQg3A) (visited on 08/31/2023).
- [94] T.Zh. Esirkepov. “Exact Charge Conservation Scheme for Particle-in-Cell Simulation with an Arbitrary Form-Factor”. In: *Computer Physics Communications* 135.2 (Apr. 2001), pp. 144–153.
- [95] Allen Taflove. “Computational Electromagnetics: The Finite-Difference Time-Domain Method”. In: *The Electrical Engineering Handbook*. Boston: Elsevier Academic Press, 2005, pp. 629–669.
- [96] H. Barucq and B. Hanouzet. “Asymptotic Behavior of Solutions to Maxwell’s System in Bounded Domains with Absorbing Silver–Müller’s Condition on the Exterior Boundary”. In: *Asymptotic Analysis* 15.1 (1997), pp. 25–40.
- [97] *Collisions*. OSIRIS Reference guide. URL: <https://osiris-code.github.io/osiris/reference/collisions>.
- [98] F. Pérez et al. “Improved Modeling of Relativistic Collisions and Collisional Ionization in Particle-in-Cell Codes”. In: *Physics of Plasmas* 19.8 (Aug. 1, 2012), p. 083104.
- [99] M. Vranic et al. “Particle Merging Algorithm for PIC Codes”. In: *Computer Physics Communications* 191 (June 2015), pp. 65–73.
- [100] Hideo Okuda and Charles K. Birdsall. “Collisions in a Plasma of Finite-Size Particles”. In: *The Physics of Fluids* 13.8 (Aug. 1, 1970), pp. 2123–2134.
- [101] Carlos A. De Moura and Carlos S. Kubrusly, eds. *The Courant–Friedrichs–Lewy (CFL) Condition: 80 Years After Its Discovery*. Boston: Birkhäuser Boston, 2013.
- [102] Charles K Birdsall and A Bruce Langdon. *Plasma Physics via Computer Simulation*. CRC press, 2004.
- [103] J.U. Brackbill. “On Energy and Momentum Conservation in Particle-in-Cell Plasma Simulation”. In: *Journal of Computational Physics* 317 (July 2016), pp. 405–427.
- [104] T D Arber et al. “Contemporary Particle-in-Cell Approach to Laser-Plasma Modelling”. In: *Plasma Physics and Controlled Fusion* 57.11 (Nov. 1, 2015), p. 113001.
- [105] Victor V. Kulagin et al. “Characteristics of Relativistic Electron Mirrors Generated by an Ultrashort Nonadiabatic Laser Pulse from a Nanofilm”. In: *Physical Review E* 80.1 (July 13, 2009), p. 016404.
- [106] Li-Xiang Hu et al. “Enhanced Dense Attosecond Electron Bunch Generation by Irradiating an Intense Laser on a Cone Target”. In: *Physics of Plasmas* 22 (Apr. 6, 2015), p. 033104.

- [107] Giada Cantono et al. “Extensive Study of Electron Acceleration by Relativistic Surface Plasmons”. In: *Physics of Plasmas* 25.3 (Mar. 1, 2018), p. 031907. arXiv: 1802.05483 [physics].
- [108] D. A. Serebryakov, E. N. Nerush, and I. Yu Kostyukov. “Near-Surface Electron Acceleration during Intense Laser-Solid Interaction in the Grazing Incidence Regime”. In: *Physics of Plasmas* 24.12 (Dec. 1, 2017), p. 123115. arXiv: 1708.09833 [physics].
- [109] Y. X. Zhang et al. “Giant Isolated Attosecond Pulses from Two-Color Laser-Plasma Interactions”. In: *Physical Review Letters* 124.11 (Mar. 18, 2020), p. 114802.
- [110] Vojtěch Horný and László Veisz. “Generation of Single Attosecond Relativistic Electron Bunch from Intense Laser Interaction with a Nanosphere”. In: *Plasma Physics and Controlled Fusion* 63.12 (Dec. 1, 2021), p. 125025.
- [111] J. F. Ong, P. Ghenuche, and K. A. Tanaka. “Electron Transport in a Nanowire Irradiated by an Intense Laser Pulse”. In: *Physical Review Research* 3.3 (Sept. 17, 2021), p. 033262.
- [112] Victor V. Kulagin et al. “Subrelativistic Infrared and Terahertz Pulses from Petawatt Class Laser Interaction with Complex Nanodimensional Targets”. In: *Relativistic Plasma Waves and Particle Beams as Coherent and Incoherent Radiation Sources IV*. Relativistic Plasma Waves and Particle Beams as Coherent and Incoherent Radiation Sources IV. Ed. by Dino A. Jaroszynski and MinSup Hur. Online Only, Czech Republic: SPIE, Apr. 18, 2021, p. 11.
- [113] Jinpu Lin et al. “Towards Isolated Attosecond Electron Bunches Using Ultrashort-Pulse Laser-Solid Interactions”. In: *Scientific Reports* 10.1 (1 Oct. 27, 2020), p. 18354.
- [114] D. E. Cardenas et al. “Sub-Cycle Dynamics in Relativistic Nanoplasma Acceleration”. In: *Scientific Reports* 9.1 (Dec. 1, 2019). pmid: 31086214.
- [115] M. Thévenet et al. “Vacuum Laser Acceleration of Relativistic Electrons Using Plasma Mirror Injectors”. In: *Nature Physics* 12.4 (Apr. 1, 2016), pp. 355–360. arXiv: 1511.05936.
- [116] S. Cousens et al. “Electron Trajectories Associated with Laser-Driven Coherent Synchrotron Emission at the Front Surface of Overdense Plasmas”. In: *Physical Review E* 101.5 (May 28, 2020), p. 053210.
- [117] A. F. Savin et al. “Attosecond-Scale Absorption at Extreme Intensities”. In: *Physics of Plasmas* 24.11 (Nov. 1, 2017).
- [118] T. Baeva et al. “The Zero Vector Potential Mechanism of Attosecond Absorption”. In: *Physics of Plasmas* 18.5 (May 2011).
- [119] Alex Savin. “Modelling Laser-Plasma Interactions for the Next Generation of High-Power Laser Experiments”. In: (2019).
- [120] A. A. Gonoskov et al. “Ultrarelativistic Nanoplasmonics as a Route towards Extreme-Intensity Attosecond Pulses”. In: *Physical Review E* 84.4 (Oct. 10, 2011), p. 046403.

- [121] D. an Brügge and A. Pukhov. “Enhanced Relativistic Harmonics by Electron Nanobunching”. In: *Physics of Plasmas* 17.3 (Mar. 2010), p. 033110. arXiv: 1002.3576 [physics].
- [122] H. Vincenti et al. “Optical Properties of Relativistic Plasma Mirrors”. In: *Nature Communications* 5 (Mar. 11, 2014), p. 3403. pmid: 24614748.
- [123] Andrea Macchi. “Theory of Light Sail Acceleration by Intense Lasers: An Overview”. In: *High Power Laser Science and Engineering* 2 (July 1, 2014), e10.
- [124] S C Wilks et al. *Absorption of Ultra-Intense Laser Pulses*. 1992.
- [125] T. Baeva, S. Gordienko, and A. Pukhov. “Theory of High-Order Harmonic Generation in Relativistic Laser Interaction with Overdense Plasma”. In: *Physical Review E - Statistical, Nonlinear, and Soft Matter Physics* 74.4 (2006). arXiv: physics/0604228.
- [126] Matthew R. Edwards and Julia M. Mikhailova. “The X-Ray Emission Effectiveness of Plasma Mirrors: Reexamining Power-Law Scaling for Relativistic High-Order Harmonic Generation”. In: *Scientific Reports* 10.1 (Dec. 1, 2020), p. 5154. pmid: 32198482.
- [127] Alex F. Savin et al. “Energy Absorption in the Laser-QED Regime”. In: *Scientific Reports* 9.1 (Dec. 1, 2019), p. 8956. pmid: 31222083.
- [128] Arkady Gonoskov. “Theory of Relativistic Radiation Reflection from Plasmas”. In: *Physics of Plasmas* 25.1 (Jan. 1, 2018). arXiv: 1708.05364.
- [129] A. Pukhov et al. “Relativistic High Harmonics and (Sub-)Attosecond Pulses: Relativistic Spikes and Relativistic Mirror”. In: *The European Physical Journal D* 55.2 (Nov. 2009), pp. 407–414.
- [130] Matthew R. Edwards, Nicholas M. Fasano, and Julia M. Mikhailova. “Electron-Nanobunch-Width-Dominated Spectral Power Law for Relativistic Harmonic Generation from Ultrathin Foils”. In: *Physical Review Letters* 124.18 (May 8, 2020). pmid: 32441983.
- [131] K. A. Tanaka et al. “Current Status and Highlights of the ELI-NP Research Program”. In: *Matter and Radiation at Extremes* 5.2 (Mar. 1, 2020), p. 024402.
- [132] A. Bret, L. Gremillet, and M. E. Dieckmann. “Multidimensional Electron Beam-Plasma Instabilities in the Relativistic Regime”. In: *Physics of Plasmas* 17.12 (Dec. 1, 2010), p. 120501.
- [133] K. T. McDonald and D. P. Russell. “Methods of Emittance Measurement”. In: *Frontiers of Particle Beams; Observation, Diagnosis and Correction*. Ed. by M. Month and S. Turner. Vol. 343. Berlin/Heidelberg: Springer-Verlag, 1989, pp. 122–132.
- [134] Ferenc Krausz and Misha Ivanov. “Attosecond Physics”. In: *Reviews of Modern Physics* 81.1 (Feb. 2, 2009), pp. 163–234.
- [135] F Calegari et al. “Ultrafast Electron Dynamics in Phenylalanine Initiated by Attosecond Pulses”. In: () .
- [136] Eiji J Takahashi et al. “Nonlinear Attosecond Metrology by Intense Isolated Attosecond Pulses”. In: *IEEE JOURNAL OF SELECTED TOPICS IN QUANTUM ELECTRONICS* 21.5 (2015).

- [137] Yuya Morimoto and Peter Baum. “Diffraction and Microscopy with Attosecond Electron Pulse Trains”. In: *Nature Physics* 14.3 (Mar. 2018), pp. 252–256.
- [138] W Schumaker. “Ultrafast Electron Radiography of Magnetic Fields in High-Intensity Laser-Solid Interactions”. In: *Physical Review Letters* 110.015003 (2013).
- [139] Joseph Duris et al. “Tunable Isolated Attosecond X-ray Pulses with Gigawatt Peak Power from a Free-Electron Laser”. In: *Nature Photonics* 14.1 (1 Jan. 2020), pp. 30–36.
- [140] Y. Glinec et al. “Radiotherapy with Laser-plasma Accelerators: Monte Carlo Simulation of Dose Deposited by an Experimental Quasimonoenergetic Electron Beam”. In: *Medical Physics* 33.1 (Jan. 2006), pp. 155–162.
- [141] S. Corde et al. “Femtosecond x Rays from Laser-Plasma Accelerators”. In: *Reviews of Modern Physics* 85.1 (Jan. 9, 2013), pp. 1–48.
- [142] K. Khrennikov et al. “Tunable All-Optical Quasimonochromatic Thomson X-Ray Source in the Nonlinear Regime”. In: *Physical Review Letters* 114.19 (May 14, 2015), p. 195003.
- [143] V V Kulagin, V N Kornienko, and V A Cherepenin. “Nonlinear Reflection of High-Amplitude Laser Pulses from Relativistic Electron Mirrors”. In: *Quantum Electronics* 46.4 (Apr. 30, 2016), pp. 315–320.
- [144] Ian Martin. “Diamond Light Source Upgrade”. Low Emittance Ring Workshop (Frascati, Italy (Remote)). 2020.
- [145] He Ping. “The Progress of HEPS Project”. 8th Low Emittance Rings Workshop (Frascati, Italy (Remote)). 2020.
- [146] C Christou. “The Pre-Injector Linac for the Diamond Light Source”. In: *Proceedings of LINAC*. Lübeck, Germany, 2004, pp. 84–86.
- [147] H. Vincenti and F. Quéré. “Attosecond Lighthouses: How To Use Spatiotemporally Coupled Light Fields To Generate Isolated Attosecond Pulses”. In: *Physical Review Letters* 108.11 (Mar. 16, 2012), p. 113904.
- [148] P. Heissler et al. “Few-Cycle Driven Relativistically Oscillating Plasma Mirrors: A Source of Intense Isolated Attosecond Pulses”. In: *Physical Review Letters* 108.23 (June 6, 2012), p. 235003.
- [149] J P Kennedy, B Dromey, and M Yeung. “Isolated Ultra-Bright Attosecond Pulses via Non-Collinear Gating”. In: *New Journal of Physics* 24.11 (Nov. 1, 2022), p. 113004.
- [150] M. Yeung et al. “Dependence of Laser-Driven Coherent Synchrotron Emission Efficiency on Pulse Ellipticity and Implications for Polarization Gating”. In: *Physical Review Letters* 112.12 (Mar. 26, 2014), p. 123902.
- [151] K. Miyauchi et al. “Laser Electron Acceleration by a Plasma Separator”. In: *Physics of Plasmas* 11.10 (Oct. 1, 2004), pp. 4878–4881.
- [152] Alexander Andreev, Konstantin Platonov, and Saltanat Sadykova. “Double Relativistic Electron Accelerating Mirror”. In: *Applied Sciences* 3.1 (Feb. 4, 2013), pp. 94–106.

- [153] M. Sherlock et al. “In-Depth Plasma-Wave Heating of Dense Plasma Irradiated by Short Laser Pulses”. In: *Physical Review Letters* 113.25 (Dec. 15, 2014).
- [154] B. Chrisman, Y. Sentoku, and A. J. Kemp. “Intensity Scaling of Hot Electron Energy Coupling in Cone-Guided Fast Ignition”. In: *Physics of Plasmas* 15.5 (May 1, 2008), p. 056309.
- [155] L. L. Ji et al. “Radiation-Reaction Trapping of Electrons in Extreme Laser Fields”. In: *Physical Review Letters* 112.14 (Apr. 8, 2014), p. 145003.
- [156] Y He et al. “A Single-Laser Scheme for Observation of Linear Breit–Wheeler Electron–Positron Pair Creation”. In: *New Journal of Physics* 23.11 (Nov. 1, 2021), p. 115005.
- [157] U. Teubner and P. Gibbon. “High-Order Harmonics from Laser-Irradiated Plasma Surfaces”. In: *Reviews of Modern Physics* 81.2 (Apr. 3, 2009), pp. 445–479.
- [158] R. L. Carman, D. W. Forslund, and J. M. Kindel. “Visible Harmonic Emission as a Way of Measuring Profile Steepening”. In: *Physical Review Letters* 46.1 (Jan. 5, 1981), pp. 29–32.
- [159] B. Bezzerides, R. D. Jones, and D. W. Forslund. “Plasma Mechanism for Ultraviolet Harmonic Radiation Due to Intense C O 2 Light”. In: *Physical Review Letters* 49.3 (July 19, 1982), pp. 202–205.
- [160] S. V. Bulanov, N. M. Naumova, and F. Pegoraro. “Interaction of an Ultrashort, Relativistically Strong Laser Pulse with an Overdense Plasma”. In: *Physics of Plasmas* 1.3 (Mar. 1, 1994), pp. 745–757.
- [161] B. Dromey et al. “Bright Multi-keV Harmonic Generation from Relativistically Oscillating Plasma Surfaces”. In: *Physical Review Letters* 99.8 (Aug. 25, 2007). pmid: 17930952.
- [162] R W Paddock et al. “Energy Gain of Wetted-Foam Implosions with Auxiliary Heating for Inertial Fusion Studies”. In: *Plasma Physics and Controlled Fusion* 66.2 (Feb. 1, 2024), p. 025005.
- [163] Henri Vincenti. “Achieving Extreme Light Intensities Using Optically Curved Relativistic Plasma Mirrors”. In: *Physical Review Letters* 123.10 (Sept. 3, 2019). pmid: 31573299.
- [164] Fabien Quéré and Henri Vincenti. “Reflecting Petawatt Lasers off Relativistic Plasma Mirrors: A Realistic Path to the Schwinger Limit”. In: *High Power Laser Science and Engineering* (2021).
- [165] R. Aboushelbaya et al. “Orbital Angular Momentum Coupling in Elastic Photon-Photon Scattering”. In: *Physical Review Letters* 123.11 (Sept. 13, 2019), p. 113604.
- [166] T Baeva. “High Harmonic Generation from Relativistic Plasma”. Mathematisch-Naturwissenschaftlichen Fakulta t der Heinrich-Heine-Universita t Du sseldorf, 2008.
- [167] A. Bourdier. “Oblique Incidence of a Strong Electromagnetic Wave on a Cold Inhomogeneous Electron Plasma. Relativistic Effects”. In: *The Physics of Fluids* 26.7 (July 1, 1983), pp. 1804–1807.

- [168] R. Lichters, J. Meyer-ter-Vehn, and A. Pukhov. “Short-Pulse Laser Harmonics from Oscillating Plasma Surfaces Driven at Relativistic Intensity”. In: *Physics of Plasmas* 3.9 (Sept. 1, 1996), pp. 3425–3437.
- [169] Raoul Trines et al. *Laser Harmonic Generation with Independent Control of Frequency and Orbital Angular Momentum*. Oct. 30, 2023. preprint.
- [170] A. P.L. Robinson et al. “Relativistically Correct Hole-Boring and Ion Acceleration by Circularly Polarized Laser Pulses”. In: *Plasma Physics and Controlled Fusion* 51.2 (2009).
- [171] A. P.L. Robinson, D. H. Kwon, and K. Lancaster. “Hole-Boring Radiation Pressure Acceleration with Two Ion Species”. In: *Plasma Physics and Controlled Fusion* 51.9 (2009).
- [172] Daniel An Der Brügge and Alexander Pukhov. “Propagation of Relativistic Surface Harmonics Radiation in Free Space”. In: *Physics of Plasmas* 14.9 (Sept. 1, 2007), p. 093104.
- [173] F. Dollar et al. “Scaling High-Order Harmonic Generation from Laser-Solid Interactions to Ultrahigh Intensity”. In: *Physical Review Letters* 110.17 (Apr. 24, 2013).
- [174] D Hillier, E Harvey, and P Treadwell. *A Model of the ORION Contrast*. E-mail. 21.11.22.
- [175] B. Dromey et al. “Diffraction-Limited Performance and Focusing of High Harmonics from Relativistic Plasmas”. In: *Nature Physics* 5.2 (2009), pp. 146–152.
- [176] G. Doumy et al. “Complete Characterization of a Plasma Mirror for the Production of High-Contrast Ultraintense Laser Pulses”. In: *Physical Review E* 69.2 (Feb. 9, 2004), p. 026402.
- [177] *45° AOI Beamsplitter Compensation Plates, UV Fused Silica for UV to NIR*. Thor Labs. URL: [https://www.thorlabs.com/newgroupage9.cfm?objectgroup\\_id=10662](https://www.thorlabs.com/newgroupage9.cfm?objectgroup_id=10662).
- [178] Mikhail N. Polyanskiy. “Refractiveindex.Info Database of Optical Constants”. In: *Scientific Data* 11.1 (Jan. 18, 2024), p. 94.
- [179] A. L. Meadowcroft, C. D. Bentley, and E. N. Stott. “Evaluation of the Sensitivity and Fading Characteristics of an Image Plate System for X-Ray Diagnostics”. In: *Review of Scientific Instruments* 79.11 (Nov. 11, 2008), p. 113102.
- [180] D. O. Golovin et al. “Calibration of Imaging Plates Sensitivity to High Energy Photons and Ions for Laser-Plasma Interaction Sources”. In: *Journal of Instrumentation* 16.02 (Feb. 2021), T02005.
- [181] N. Izumi et al. “Application of Imaging Plates to X-Ray Imaging and Spectroscopy in Laser Plasma Experiments (Invited)”. In: *Review of Scientific Instruments* 77.10 (Oct. 23, 2006), 10E325.
- [182] Krzysztof W Fornalski. “Simple Empirical Correction Functions to Cross Sections of the Photoelectric Effect, Compton Scattering, Pair and Triplet Production for Carbon Radiation Shields for Intermediate and High Photon Energies”. In: *Journal of Physics Communications* 2.3 (Mar. 22, 2018), p. 035038.

- [183] P. Beiersdorfer et al. “Lineshape Spectroscopy with a Very High Resolution, Very High Signal-to-Noise Crystal Spectrometer”. In: *Review of Scientific Instruments* 87.6 (June 1, 2016).
- [184] M. J. MacDonald et al. “Absolute Throughput Calibration of Multiple Spherical Crystals for the Orion High-REsolution X-ray Spectrometer (OHREX)”. In: *Review of Scientific Instruments* 92.2 (Feb. 1, 2021). pmid: 33648146.
- [185] N. Hell et al. “Calibration of the OHREX High-Resolution Imaging Crystal Spectrometer at the Livermore Electron Beam Ion Traps”. In: *Review of Scientific Instruments* 87.11 (Nov. 1, 2016), p. 11D604.
- [186] B.L. Henke, E.M. Gullikson, and J.C. Davis. “X-Ray Interactions: Photoabsorption, Scattering, Transmission, and Reflection at  $E = 50\text{-}30,000 \text{ eV}$ ,  $Z = 1\text{-}92$ ”. In: *Atomic Data and Nuclear Data Tables* 54.2 (July 1993), pp. 181–342.
- [187] S. E. Perevalov et al. “Laser Peeler Regime of High-Harmonic Generation for Diagnostics of High-Power Focused Laser Pulses”. In: *Matter and Radiation at Extremes* 8.3 (May 1, 2023), p. 034402.
- [188] I. Ouatu et al. “Ionization States for the Multipetawatt Laser-QED Regime”. In: *Physical Review E* 106.1 (July 27, 2022), p. 015205.
- [189] C. Zulick et al. “High Resolution Bremsstrahlung and Fast Electron Characterization in Ultrafast Intense Laser–Solid Interactions”. In: *New Journal of Physics* 15.12 (Dec. 2013), p. 123038.
- [190] *Eagle XV – In Vacuum X-Ray*. Raptor Photonics. URL: <https://www.raptorphotonics.com/products/eagle-xv/>.
- [191] Sam Astbury. *Target Fabrication Group, Central Laser Facility, STFC Rutherford Appleton Laboratory, Didcot OX11 0QX, UK*. E-mail. 2024.
- [192] B. Dromey et al. “Third Harmonic Order Imaging as a Focal Spot Diagnostic for High Intensity Laser-Solid Interactions”. In: *Laser and Particle Beams* 27.2 (June 2009), pp. 243–248.
- [193] *Ansys Zemax OpticStudio*. Ansys. URL: <https://www.ansys.com/products/optics/ansys-zemax-opticstudio> (visited on 04/05/2024).
- [194] Aghapi G. Mordovanakis et al. “Quasimonoenergetic Electron Beams with Relativistic Energies and Ultrashort Duration from Laser-Solid Interactions at 0.5 kHz”. In: *Physical Review Letters* 103.23 (Dec. 1, 2009).
- [195] Matthew J. Suggit et al. “Nanosecond White-Light Laue Diffraction Measurements of Dislocation Microstructure in Shock-Compressed Single-Crystal Copper”. In: *Nature Communications* 3.1 (Nov. 27, 2012), p. 1224.
- [196] W. H. Bragg and W. L. Bragg. “Diffraction of Waves”. In: *X Rays and Crystal Structure*. Bell, 1915, pp. 8–19.
- [197] M. Behmke et al. “Controlling the Spacing of Attosecond Pulse Trains from Relativistic Surface Plasmas”. In: *Physical Review Letters* 106.18 (May 6, 2011), p. 185002.
- [198] C. Rödel et al. “Harmonic Generation from Relativistic Plasma Surfaces in Ultrasteep Plasma Density Gradients”. In: *Physical Review Letters* 109.12 (Sept. 19, 2012), p. 125002.

- [199] S. Kahaly et al. “Direct Observation of Density-Gradient Effects in Harmonic Generation from Plasma Mirrors”. In: *Physical Review Letters* 110.17 (Apr. 22, 2013), p. 175001.
- [200] B. Y. Li et al. “Experimental Demonstration of Efficient Harmonic Generation via Surface Plasma Compression with Lasers”. In: *Physical Review Letters* 128.24 (June 14, 2022), p. 244801.
- [201] Yi Cai et al. “Time-Resolved Measurements on Reflectivity of an Ultrafast Laser-Induced Plasma Mirror”. In: *Physics of Plasmas* 16.10 (Oct. 1, 2009), p. 103104.
- [202] B. Dromey et al. “Coherent Synchrotron Emission in Transmission from Ultrathin Relativistic Laser Plasmas”. In: *New Journal of Physics* 15 (Jan. 2013).
- [203] D. Batani et al. “Physics Issues for Shock Ignition”. In: *Nuclear Fusion* 54.5 (May 1, 2014), p. 054009.
- [204] A. Bourdier and S. Gond. “Dynamics of a Charged Particle in a Linearly Polarized Traveling Electromagnetic Wave”. In: *Physical Review E* 63.3 (Feb. 23, 2001), p. 036609.
- [205] Klaus Floettmann. “Some Basic Features of the Beam Emittance”. In: *Physical Review Special Topics - Accelerators and Beams* 6.3 (2003), pp. 80–86.
- [206] Wiedemann. *Particle Accelerator Physics*. New York, NY: Springer Berlin Heidelberg, 2015.